Max-Planck-Institut für Metallforschung
Stuttgart

Transmission Electron Microscopy Investigations of Thin Mo and Pd Films Grown on $SrTiO_3$ Substrates

Elena Tchernychova

Dissertation
an der
Universität Stuttgart

Bericht Nr. 153
Juni 2004

Transmission Electron Microscopy Investigations of Thin Mo and Pd Films Grown on $SrTiO_3$ Substrates

Von der Fakultät Chemie der Universität Stuttgart
zur Erlangung der Würde eines
Doktors der Naturwissenschaften (Dr. rer. nat.)
genehmigte Abhandlung

vorgelegt von

Elena Tchernychova

aus Sankt Petersburg

Hauptberichter:	Prof. Dr. M. Rühle
Mitberichter:	Prof. Dr. F. Aldinger
Tag der Einreichung:	31 März 2004
Tag der mündlichen Prüfung:	22 Juni 2004

Max–Planck–Institut für Metallforschung

Stuttgart 2004

Parts of this thesis were published in following articles:

- E. Tchernychova, C. Scheu, T. Wagner, Q. Fu and M.Rühle
  Electron microscopy studies of thin Mo films grown by MBE on (100) $SrTiO_3$ substrates
  Surface Science **542** (2003) 33-44

- Q. Fu, E. Tchernychova and T. Wagner
  Texture of molybdenum thin films on $SrTiO_3$: a RHEED study
  Surface Science Letters **538** (2003) L511-L517

- M. Gao, C. Scheu, E. Tchernychova and M. Rühle
  Electron-energy-loss spectroscopy studies of Mo/$SrTiO_3$ interfaces grown by molecular beam epitaxy
  Journal of Microscopy **210** (2003) 94-101

Contents

List of Abbreviations

AES	Auger Electron Spectroscopy
AFM	Atomic Force Microscopy
CSL	Coincidence Site Lattice
CTEM	Conventional Transmission Electron Microscopy
CTF	Contrast Transfer Function
EELS	Electron Energy Loss Spectroscopy
ELNES	Energy-loss Near Edge Structure
FFT	Fast Fourier Transform
GIXS	Grazing Incidence x-ray scattering
GB	Grain Boundary
HAADF	High-Angle Annular Dark Field
HeD	Helium-atom Diffraction
HRTEM	High-resolution Transmission Electron Microscopy
IAS	Infrared Absorption Spectroscopy
LEEDS	Low Energy Electron Diffraction Spectroscopy
LEIS	Low Energy Ion Scattering
MBE	Molecular Beam Epitaxy
MEIS	Medium-energy Ion Scattering
ML	Monolayer
MSD	Magnetron Sputter Deposition
NCSL	Near Coincidence Site Lattice
OR	Orientation Relationship
QHRTEM	Quantitative High-resolution Transmission Electron Microscopy

RHEED	Reflection High-energy Electron Diffraction
RT	Room Temperature
SAD	Selected Area Diffraction
SEM	Scanning Electron Microscopy
STEM	Scanning Transmission Electron Microscopy
STM	Scanning Tunneling Microscopy
STS	Scanning Tunneling Spectroscopy
STO	$SrTiO_3$
TEM	Transmission Electron Microscopy
UHV	Ultra High Vacuum
UPS	Ultraviolet Photoelectron Spectroscopy
XCF	Cross Correlation Factor
XPS	X-Ray Photoelectron Spectroscopy
XRD	X-Ray Diffraction
λ	wave length
C_s	spherical abberation
Df	defocus
FF	Fourier transform
f	lattice misfit
Δf	defocus (positive values stand for underfocus)
Δf_{sch}	Scherzer defocus
(hkl)	crystallographic plane
$\langle hkl \rangle$	crystallographic direction

Summary

Thin metal films deposited on ceramic substrates are employed in a wide variety of technological applications, such as catalysts, gas sensors, supercondctors, cell-capacitors in RAM devices, etc. [Uchino1994, Meixner1995]. Constantly decreasing dimensions of such devices bring up the importance of thorough investigations of systems containing metal/ceramic interfaces, since their mechanical and electronic properties control the performance of the devices. These interfacial properties, in their turn, are strongly influenced by the atomic structure, composition and bonding at the interface.

In the present work, $SrTiO_3$ with its cubic perovskite structure was chosen as a model substrate. Two different metals, Mo and Pd were deposited on the (100) $SrTiO_3$ surface by molecular beam epitaxy (MBE) under ultra-high vacuum (UHV) conditions with a residual gas pressure below 10^{-7} Pa. Prior to the metal deposition, the surface of the $SrTiO_3$ was treated following the technique of Kawasaki *et al.* [Kawasaki1994], which allows to obtain a TiO_2 surface termination. The Mo films were deposited at $T_{substrate} = 600°C$, while the deposition of Pd films was accomplished at $T_{substrate} = 650°C$. These conditions resulted in the formation of epitaxial orientation relationships between the metal films and the $SrTiO_3$ substrate.

The Pd/$SrTiO_3$ was chosen for this study since it represents a perfect metal/$SrTiO_3$ model system. A low oxygen affinity of Pd, i.e. low reactivity, hinders the formation of a reaction layer at the interface. Similar lattice constants between Pd and $SrTiO_3$ ($a_{Pd} = 3.89$Å, $a_{STO} = 3.905$Å) should lead to a perfect fit of Pd on top of $SrTiO_3$. The Mo, on the other hand, has a much higher oxygen affinity compared to Pd. Therefore, a reaction layer might form at the interface. The lattice mismatch between the Mo and $SrTiO_3$ is between 12% to 24%, depending on the considered directions ($a_{Mo} = 3.15$Å, $a_{STO} = 3.905$Å). Theoretical

ab initio calculations performed by Ochs *et al.* [Ochs2000] for the $Pd/SrTiO_3$ system and by Classen [Classen2001] for the $Mo/SrTiO_3$ system demonstrated similarities between the systems. For both cases, the TiO_2 termination with metal atoms positioned on top of the O atoms was determined as energetically favorable configuration.

In this study, the $Mo/SrTiO_3$ system was investigated using different transmission electron microscopy (TEM) techniques, such as conventional TEM, selected area diffraction (SAD), nano-diffraction and high-resolution TEM (HRTEM). Both cross-sectional and plan-view TEM specimens were studied in order to obtain a complete picture of the film microstructure as well as the interface structure. As deposited, the $Mo/SrTiO_3$ specimens were investigated by X-ray diffraction (XRD) to examine the obtained epitaxy. In addition, reflection high-energy electron diffraction (RHEED) experiments were performed *in situ* during the growth to determine the growth behavior of ultra-thin Mo films.

The TEM investigations of the $Mo/SrTiO_3$ system performed on the cross-sectional TEM specimens revealed that the Mo film had a polycrystalline structure. The presence of two geometrically inequivalent orientation relationships with two and four geometrically equivalent rotational variants, respectively, was found:
$(110)_{Mo}\langle 110\rangle_{Mo}\langle 100\rangle_{Mo} \| (100)_{STO}\langle 100\rangle_{STO}\langle 100\rangle_{STO}$ (OR Ia,b),
$(110)_{Mo}\langle 111\rangle_{Mo} \| (100)_{STO}\langle 110\rangle_{STO}$ (OR II).
The distribution of the variants was investigated in TEM by SAD of plan-view specimens. The majority of the grains was belonging to the OR II variant, although deviations from the perfect OR were detected. The employed near coincidence site lattice (NSCL) model was able to explain these results successfully, although the other variant, OR I, could not be explained by a simple geometrical model without considering the full energetics of the system. The grain boundaries between the variants examined by HRTEM form low-energy special tilt grain boundaries. This also explains the deviations from the perfect ORs, since the system is minimizing its total energy by finding a balance between interface, grain boundary and surface energies. The growth of fcc-like Mo, which was predicted by *ab initio* calculations [Classen2001], was observed by RHEED at the initial stage of the film growth for films with nominal thicknesses of 0.6 nm. HRTEM of cross-sectional specimens of $Mo/SrTiO_3$ revealed an abrupt interface. No significant reaction layer was detected. Misfit dislocations

accommodating the large lattice misfit between Mo and $SrTiO_3$ were observed. However, a quantitative HRTEM analysis of the Mo/$SrTiO_3$ interface could not be performed due to the insufficient quality of the HRTEM images.

In contrast, the Pd/$SrTiO_3$ interface could be studied by quantitative HRTEM and high-angle annular dark field (HAADF) techniques. The aim was to determine the projected bonding distance, i.e. the projected distance between the last layer of $SrTiO_3$ and the first layer of Pd, and the atomic configuration at the interface. The latter includes the termination of the $SrTiO_3$ and the adhesion sites of the Pd atoms. To obtain this information, HRTEM images were taken at the JEM-ARM 1250 with an accelerating voltage of 1250 kV, a point-to-point resolution of 1.2 Å and C_s = 2.6 mm. In addition, a JEM-2010F FEG, with an accelerating voltage of 200 kV, point-to-point resolution of 1.8 Å and C_s = 0.5 mm was used. This microscope has a scanning unit and a JEOL HAADF EM-24015BU detector. The HRTEM images were simulated using EMS [Stadelmann1987] and IDIM [Moebus1994] programm packages in order to retrieve the atomic structure of the Pd/$SrTiO_3$ interface. The projected bonding distance was determined using a modified method of Schweinfest *et al.* [Schweinfest1998]. In addition, the HAADF imaging technique was employed to clarify the atomic composition at the Pd/$SrTiO_3$ interface.

The HRTEM investigations showed that the Pd/$SrTiO_3$ interface is coherent. The orientation relationship was found to be cube-on-cube with
$(100)_{Pd}\langle 100\rangle_{Pd} \| (100)_{STO}\langle 100\rangle_{STO}$,
which is in agreement with the results of Richter and Van Benthem [Richter2000, Benthem2002]. However, the Pd did not form a continuous film on top of $SrTiO_3$. Instead, 3-dimensional islands were observed. HRTEM revealed an atomically abrupt Pd/$SrTiO_3$ interface. Substrate steps that have a height of one $SrTiO_3$ unit cell were found. This indicates that the surface termination stays the same across the whole specimen. The projected bonding distance at the interface is $T = 2.54$Å, which was determined with a precision of ± 0.05Å. However, the quantitative HRTEM did not allow to determine uniquely the termination of the $SrTiO_3$, and, therefore the atomic composition at the interface. Only two of the four possible structure models of the Pd/$SrTiO_3$ interface could be eliminated completely through the quantitative analysis, the TiO_2 terminated with Pd positioned on top of the O atoms and the SrO termi-

nated with Pd positioned on top of the Sr and O atoms. Both remaining structure models, TiO_2 terminated with Pd positioned on top of the Ti atoms and above the hollow sites, and the SrO terminated with Pd atoms positioned above the hollow sites, were found to be less energetically favorable compared to the excluded one with a TiO_2 termination and Pd atoms positioned on top of the O atoms [Ochs2000]. The HAADF technique also did not allow to determine uniquely the termination at the $Pd/SrTiO_3$ interface, since the image quality was not sufficient.

Zusammenfassung

Metall/Keramik Systeme besitzen zahlreiche technologische Anwendungen, wie z.B. in Sensoren, Aktuatoren, elektro-optischen und mikro-elektronischen Bauelementen [Uchino1994, Meixner1995]. Die Grenzflächen in solchen Systemen gewinnen dabei zunehmend an Bedeutung, da ihr Einfluss auf die mechanischen und elektronischen Eigenschaften durch die stetig voranschreitende Miniaturisierung zunimmt. Um ein grundlegendes Verständnis der materialphysikalischen Zusammenhänge zu entwickeln, ist daher eine Charakterisierung der Grenzflächen bezüglich der atomistischen Struktur und der Bindungen erforderlich.

Für die vorliegende Arbeit wurde eine kubische $SrTiO_3$-Keramik als Substrat ausgewählt. Auf die (100)-Oberfläche dieses Substrats wurden zwei unterschiedliche Metalle (Pd und Mo) mittels Molekularstrahlepitaxie (MBE) unter Ultrahochvakuum-Bedingungen aufgebracht. Die $SrTiO_3$-Oberfläche wurde vor dem Beschichten nach der Methode von Kawasaki *et al.*[Kawasaki1994] behandelt, um eine TiO_2-Oberflächenterminierung zu erhalten. Um ein epitaktisches Wachstum der Metallschicht auf dem Substrat zu erreichen, musste für das Aufbringen des Mo eine Temperatur von $T_{Substrat} = 600°C$ und des Pd von $T_{Substrat} = 650°C$ gewählt werden.

Aufgrund der sehr geringen Sauerstoffaffinität von Pd erwartet man keine Reaktionsschicht an der Pd/$SrTiO_3$-Grenzfläche. Da die Gitterkonstanten von Pd und $SrTiO_3$ nahezu übereinstimmen ($a_{Pd} = 3.89$Å, $a_{STO} = 3.905$Å), sollten zudem keine Gitterfehlpassungsversetzungen an der Grenzfläche entstehen. Daher kann das System Pd/$SrTiO_3$ als perfektes Modellsystem für die Untersuchungen an Metall/$SrTiO_3$ Grenzflächen betrachtet werden. Im Gegensatz zu Pd besitzt Mo eine höhere Sauerstoffaffinität, so dass die Bildung einer Reaktionsschicht möglich ist. Die Gitterparameter von Mo und $SrTiO_3$ unterscheiden sich je nach betrachteter Richtung um bis zu 24%, so dass Gitterfehlpassungsversetzungen auftre-

ten sollten. Ochs et al. [Ochs2000] und Classen [Classen2001] konnten dennoch durch ihre *ab initio*-Rechnungen Gemeinsamkeiten der beiden Metall/$SrTiO_3$ Systeme nachweisen. Die Ergebnisse der beiden theoretischen Untersuchungen zeigten, dass aus energetischen Gründen die TiO_2-Terminierung bevorzugt wird. Die Pd-Atome bzw. Mo-Atome besetzen dabei Plätze direkt oberhalb der O-Atome des $SrTiO_3$, wodurch Pd-O- bzw. Mo-O-Bindungen an der Grenzfläche begünstigt werden. Zudem treten auch Bindungen zwischen den Ti-Atomen und dem aufgebrachten Metall auf, während die Sr-Atome nicht zur Bindung beitragen.

In der vorliegende Arbeit wurde das Mo/$SrTiO_3$ mittels Transmissionelektronenmikroskopie (TEM) untersucht, um die Filmmorphologie und die Grenzflächenstruktur zu bestimmen. Dabei kamen verschiedene Verfahren, wie z.B. konventionelle TEM, Feinbereichsbeugung, Nano-Beugung und hochauflösende TEM (HRTEM), zum Einsatz. Für eine vollständige Charakterisierung der Mo-Schicht sowie der atomaren Struktur der Grenzfläche wurden sowohl Querschnitts- als auch Aufsichtsproben im TEM untersucht. Nach dem Aufbringen der Schicht wurden die Mo/$SrTiO_3$ Proben mittels Röntgenbeugung untersucht, um die Epitaxie der Mo-Schichten zu bestimmen. Außerdem wurden *in situ* RHEED Untersuchungen durchgeführt, während denen das Aufwachsverhalten von ultra-dünnen Mo-Schichten beobachtet werden konnte.

Die TEM-Untersuchungen der Mo/$SrTiO_3$-Querschnittproben zeigten, dass der Film eine $(110)_{Mo}$-Textur besitzt und aus zwei geometrisch ungleichen Domänen besteht:
$(110)_{Mo}\langle 110\rangle_{Mo}\langle 100\rangle_{Mo} \| (100)_{STO}\langle 100\rangle_{STO}\langle 100\rangle_{STO}$ (OR Ia,b) und
$(110)_{Mo}\langle 111\rangle_{Mo} \| (100)_{STO}\langle 110\rangle_{STO}$ (OR II).
Die Verteilung der Domänen mit unterschiedlicher Orientierungsbeziehung zum $SrTiO_3$ wurde an den Aufsichtsproben mittels Feinbereichsbeugung untersucht. Die Mehrheit der Körner besitzt die OR II. Es wurden zudem Körner beobachtet, deren Orientierung zum $SrTiO_3$ von der perfekten Orientierungsbeziehung um einige Grad abweicht. Diese Ergebnisse konnten zum Teil mit Hilfe des geometrischen Koinzidenzgitter (NCSL: near coincidence site lattice") Modells gedeutet werden, wobei das Auftreten der zur OR I gehörenden Körner nur unter Berücksichtigung der vollständigen Energiebilanz des Systems erklärt werden kann. HRTEM Aufnahmen der Korngrenzen zwischen den Domänen zeigten die Präsenz speziellen Korngrenzen niedriger Energie. Diese Beobachtung kann möglicherweise die Anwesen-

heit von Körner erklären, deren Orientierungsbeziehung von der perfekten Orientierungsbeziehung um einige Grad abweicht. Das System versucht seine Energie durch das Erreichen des Gleichgewichts zwischen Oberflächen-, Korngrenzen- und Grenzflächenenergie abzusenken. Bei den theoretischen *ab initio* Rechnungen wurde vorhergesagt, dass bei ultradünnen Schichten (= 3 Monolagen) Mo nicht in der kubischraumzentrierten sondern in der kubischflächenzentrierten Struktur vorliegen sollte [Classen2001]. Das Wachstum von kubischflächenzentrierten Mo konnte während der *in situ* RHEED Untersuchung von ultradünnen Mo-Filmen (nominelle Filmdicke von $\sim$ 0.6 nm) auch experimentell bestätigt werden. Die HRTEM Aufnahmen von Mo/$SrTiO_3$ zeigten eine abrupte Grenzfläche, wobei keine signifikante Grenzflächenreaktionsschicht gefunden werden konnte. Die große Gitterfehlpassung zwischen Mo und $SrTiO_3$ wurde durch das Einbringen von Gitterfehlpassungsversetzungen kompensiert. Eine quantitative Analyse der HRTEM-Aufnahmen der Mo/$SrTiO_3$-Grenzfläche konnte aufgrund unzureichender Bildqualität der HRTEM-Aufnahmen nicht durchgeführt werden.

Im Gegensatz zur Mo/$SrTiO_3$- konnte die Pd/$SrTiO_3$-Grenzfläche mit Hilfe von quantitativer HRTEM- und HAADF- ("high angle annular dark field") Techniken untersucht werden. Das Ziel der Experimente war dabei die Untersuchung der atomaren Struktur der Grenzfläche, d.h. die Terminierung des $SrTiO_3$ sowie die Positionierung der Pd Atome sollte ermittelt werden. Zudem sollte der projizierte Bindungsabstand, welcher als der Abstand zwischen der letzten Ebene des $SrTiO_3$ und der ersten Ebene des Pd definiert ist, quantitativ bestimmt werden. Die erforderlichen HRTEM- und HAADF-Bilder wurden mit einem JEM-ARM 1250 und einem JEM-2010F FEG aufgenommen. Das JEM-ARM 1250 besitzt eine Beschleunigungsspannung von 1250 kV, ein C_s von 2.6 mm und ein Auflösungsvermögen von 1.2 Å. Das JEM-2010F FEG wurde bei einer Beschleunigungsspannung von 200 kV betrieben und besitzt ein Auflösungsvermögen von 1.8Å und ein C_s von 0.5 mm. Zusätzlich ist es mit einer Rastereinheit und mit einem JEOL HAADF EM-24015BU-Detektor ausgestattet, wodurch HAADF-Untersuchungen möglich sind. Die Bestimmung der atomaren Struktur der Pd/$SrTiO_3$-Grenzfläche erfolgte mit Hilfe des Vergleichs von experimentellen und simulierten HRTEM-Aufnahmen, wobei die Softwareprogramme EMS [Stadelmann1987] und IDIM [Moebus1994] zum Einsatz kamen. Der projizierte Bindungsabstand wurde nach der Metho-

de von Schweinfest *et al.* [Schweinfest1998] ermittelt. Die HAADF-Abbildungstechnik wurde verwendet, um die chemische Zusammensetzung der Pd/$SrTiO_3$-Grenzfläche zu ermitteln.

Die TEM Untersuchungen zeigten, dass kein geschlossener Pd-Film sondern 3-dimensionale Pd-Inseln auftreten. Diese besitzen die folgende epitaktische Orientierungsbeziehung mit dem $SrTiO_3$:

$(100)_{Pd}\langle 100\rangle_{Pd} \| (100)_{STO}\langle 100\rangle_{STO}$.

Diese Ergebnisse stimmen mit den Ergebnissen früherer Untersuchungen am System Pd/$SrTiO_3$ überein, welche von Richter [Richter2000] und van Benthem [Benthem2002]durchgeführt wurden. HRTEM-Aufnahmen der Pd/$SrTiO_3$-Querschnittproben zeigten eine abrupte, kohärente Grenzfläche. Die beobachteten Substratstufen stimmen in ihrer Höhe mit einer $SrTiO_3$ Einheitszelle überein, so dass die Substratterminierung entlang der Grenzfläche unverändert bleibt. Der projizierte Bindungsabstand beträgt $T = 2.54$ Å und wurde mit einer Präzision von ± 0.05 Å bestimmt. Dennoch erlaubt die quantitative HRTEM-Analyse keine klare Aussage über die Substratterminierung, da nur zwei von vier möglichen Strukturmodellen (TiO_2-terminiertes Modell mit Pd-Atomen oberhalb der O-Atome und SrO-terminiertes Modell mit Pd-Atomen oberhalb der Sr- und O-Atome) mittels quantitativen Analyse ausgeschlossen werden konnten. Die zwei übrigen Strukturmodelle (TiO_2-terminiertes Modell mit Pd-Atomen oberhalb der Ti-Atome und der Lückenpositionen und SrO-terminiertes Modell mit Pd-Atomen oberhalb der Lückenpositionen) gelten jedoch nach den *ab initio*-Rechnungen von Ochs *et al.* [Ochs2000] gegenüber dem TiO_2-terminierten Modell mit Pd oberhalb der O-Atome als energetisch ungünstiger. Auch die HAADF-Technik erlaubte keine eindeutige Schlussfolgerung bezüglich der Terminierung des Substrats, da die Bildqualität aufgrund von Störungen der Rastereinheit nicht ausreichend war.

Chapter 1

Introduction

Metal/ceramic systems possess numerous applications in industry, e.g, in microelectronic devices, gas sensors [Uchino1994], actuators [Meixner1995], and recording media. In many of these applications the metal/ceramic system is realized by depositing a thin metal film on a ceramic substrate. In order to control the performance of the devices a basic understanding of the microstructure of the thin metal film and the interface between the metal film and the substrate is important.

Most of the studies reported in literature are dealing with the growth behavior and epitaxy of thin films deposited on different oxide substrates. Frequently used substrates are MgO, TiO_2 and Al_2O_3 [Goyhenex1996, Renaud1999, Evans1996, Dehm1998, Hansen1999, Domenichini2000, Svedberg1999, May2001, Wagner2001]. Most of the deposited metals are alkali metals or $3d$ and $4d$ transition metals. Investigations of Pt, Ni, Cu, Y, Ti, Ba and Cr metals deposited on (100) $SrTiO_3$ substrates can be found in literature [Chung1979, Kawada1999, Polli2000, Jackson1994, Kido2000, Benthem2002, Benthem2002a, Fu2001, Fu2002, Dehm2002, Hill1989, Conard1996, Andersen1990]. Frequently, surface science methods, such as reflection high-energy electron diffraction (RHEED), atomic force microscopy (AFM), auger electron spectroscopy (AES), X-ray photoelectron spectroscopy (XPS), scanning electron microscopy (SEM), scanning tunnelling microscopy (STM), scanning tunnelling spectroscopy (STS), and X-ray diffraction (XRD) techniques were applied. These methods are employed to study *in situ* the growth behavior of the films or *ex situ* their microstructure. The atomic structure of the interfaces is often characterized by transmission electron microscopy

(TEM) techniques (see e.g. [Ruehle1989, Ruehle1990, Howe1997, Sinnott2003] for overviews). Despite of the large number of investigations of different metal/ceramic systems, only a small number of the reports simultaneously address the bonding behavior and the atomic structure at the interface [Schweinfest1998, Scheu1998, Dehm1997, Benthem2002, Benthem2002a].

In this work, interfaces between the (100) $SrTiO_3$ surface and Pd and Mo films were produced and investigated. The films were grown by molecular beam epitaxy (MBE) in ultra-high vacuum. For both systems, a well-defined substrate preparation procedure was used [Kawasaki1994], resulting in a TiO_2 surface termination. The Pd/$SrTiO_3$ system serves as a model system due to the following reasons: (i) Pd possesses low oxygen affinity (reactivity), which should prevent the formation of a reaction layer at the interface, and (ii) Pd and $SrTiO_3$ have nearly identical lattice parmeter (a_{Pd} = 3.89Å, a_{STO} = 3.905Å), which most likely results in a coherent metal/$SrTiO_3$ interface. For a semicoherent Pd/$SrTiO_3$ interface, the distance between misfit dislocations would amount to 260Å. The opposite example represents the Mo/$SrTiO_3$ system, since Mo (i) has a high oxygen affinity, and, therefore, is expected to react with $SrTiO_3$. (ii) Furthermore, the lattice mismatch between Mo and $SrTiO_3$ is large, with values ranging between 12% and 24% depending on the orientation relationship (a_{Mo} = 3.15Å, a_{STO} = 3.905Å). Consequently, different epitaxial orientation relationships may form for Mo on (100) $SrTiO_3$ compared to the cube-on-cube orientation relationship, identified for the Pd/$SrTiO_3$ system [Richter2000].

First principle calculations of the Mo/$SrTiO_3$ interface suggest that (110) Mo is preferably parallel to (100) $SrTiO_3$ with a TiO_2 termination of the substrate [Classen2001]. In this configuration, Mo atoms are positioned on top of O atoms. Currently, *ab initio* calculations can only be performed for a small number of atoms, typically below $\sim$ 50. Therefore, a small supercell with an artificial perfect fit between the Mo and $SrTiO_3$ was used. For this reason, the Mo (110) plane was stretched and compressed in two perpendicular directions in order to fit on top of the $SrTiO_3$ (100) plane with a misfit of less than 0.5% [Classen2001]. The calculations performed for the Mo film thicknesses of 3 ML show that it is energetically favorable if Mo crystallizes in the fcc structure [Classen2001].

The existence of fcc-like Mo could be confirmed for a nominally 0.6 nm thick Mo film on $SrTiO_3$ by *in situ* RHEED observations [Fu2003]. With increasing film thickness, the lattice

grew in the bcc structure [Fu2003]. These films are investigated in this thesis by different TEM techniques, such as conventional TEM, SAD, nano-diffraction and HRTEM on cross-sectional and plan-view specimens in order to obtain a complete description of the bcc film microstructure. This includes the orientation relationship between Mo and $SrTiO_3$ as well as the structure of grain boundaries within the Mo film.

Previously, Richter [Richter2000] has studied the growth behavior of Pd on $SrTiO_3$. He determined a cube-on-cube orientation relationship between the Pd and $SrTiO_3$ with the Pd growing in a 3-dimensional island growth mode [Richter2000]. *Ab initio* band structure calculations for the Pd/$SrTiO_3$ system, performed by Ochs *et al.* [Ochs2000], proposed interfacial bonding between the Pd and O atoms of the TiO_2 terminated $SrTiO_3$ surface, similarly to the Mo/$SrTiO_3$ system [Classen2001]. Van Benthem [Benthem2002] analyzed the bonding across the Pd/$SrTiO_3$ interface by EELS and ELNES. The best agreement between the experimental ELNES data and the calculated projected density of states was found for the case, where the $SrTiO_3$ is TiO_2 terminated.

In the present work, a quantitative analysis of high-resolution TEM images of the Pd/$SrTiO_3$ interface was performed by image simulations [Stadelmann1987, Moebus1994] in order to retrieve the atomic structure of the Pd/$SrTiO_3$ interface. The results will be analyzed with respect to the experimentally obtained $SrTiO_3$ surface termination and compared to *ab initio* predictions and ELNES results reported in the literature.

Outline of the Thesis

The thesis consists of three main parts, which cover fundamentals (Part I), specimen preparation and experimental details (Part II), and results (Part III).

Part I contains Chapters 1 to 4. After the introduction, Chapter 2 outlines the fundamental aspects of metal/ceramic interfaces and growth modes of thin films on bulk substrates. The important properties of Pd, Mo and $SrTiO_3$ are summarized in Section 2.3 of Chapter 2. In Chapter 3 a literature survey on metal/$SrTiO_3$, Pd/oxide and Mo/oxide interfaces is presented. Publications concerning substrate preparation methods are reviewed in Section 3.1.1.

Essential experimental techniques are introduced in Chapter 4. Here, Section 4.1 treats

X-ray diffraction, while Section 4.2 is dedicated to TEM techniques. Quantitative HRTEM analysis is described in Section 4.2.3, and the HAADF (Z-Contrast) method in Section 4.2.4.

Part II covers Chapter 5, where the experimental details of the MBE film growth and TEM specimen preparation are given.

In Chapters 6 and 7 (Part III) the obtained results for $Mo/SrTiO_3$ (Chapter 6) and $Pd/SrTiO_3$ (Chapter 7) are described, quantitatively evaluated and, finally, discussed.

Part I

Fundamentals

Chapter 2

Basics

In section 2.1 the basics for describing metal/ceramic interfaces are given. Section 2.2 provides the essential models and equations for thin film growth. The properties of the materials, used in this study ($SrTiO_3$, Pd and Mo), are reviewed in section 2.3.

2.1 Interfaces

2.1.1 Orientation Relationship

A heterophase boundary is formed if two materials with different crystallographic structure and chemistry are joint. A typical example are metal/ceramic interfaces, which are of a great technological and scientific importance.

An interface is described by 6 macroscopic and 4 microscopic geometrical degrees of freedom [Sutton1994]. Within the macroscopic degrees of freedom, 3 are related to the orientation between the two crystals and 2 are responsible for the orientation of the interface. An additional degree of freedom is associated with the handedness of the either crystal. The macroscopic degrees of freedom are usually written in a simple form, showing directions that are parallel within both crystals and also planes that are parallel to the interface.

From the microscopic parameters, 3 describe the translation state, which corresponds to the relative displacement of the crystals against each other. One more parameter is needed to describe the location of the interface plane, if the basis of either crystal is not monoatomic.

In the present work, orientation relationships (OR) between the metal films and the ceramic substrate are given as

$$(hkl)[uvw] \parallel (h'k'l')[u'v'w'], \tag{2.1}$$

where (hkl) and $(h'k'l')$ denote planes parallel to the interface and $[uvw]$ and $[u'v'w']$ are directions that are parallel to each other and lie in the interface plane.

2.1.2 Lattice Mismatch

Most materials possess different lattice parameters. This difference can be described by means of the lattice mismatch parameter f:

$$f = \frac{d_{hkl\ (film)} - d_{h'k'l'\ (substrate)}}{d_{h'k'l'\ (substrate)}}, \tag{2.2}$$

where $d_{hkl\ (film)}$ and $d_{h'k'l'\ (substrate)}$ are the lattice planes of the film and the substrate, which are parallel to each other across the interface.

Usually, the thermal expansions of the film and the substrate are different, and the values of the lattice mismatch f depend on temperature. In this case, the lattice spacings in equation (2.2) should be corrected with respect to a reference state at temperature T_0:

$$\Delta d_{hkl} = d_{1\ hkl} - d_{0\ hkl} = d_{0\ hkl} \cdot \alpha \cdot (\mathrm{T}_1 - \mathrm{T}_0), \quad \text{or} \tag{2.3}$$

$$\Delta d_{hkl} = d_{0\ hkl} \cdot \alpha \cdot \Delta \mathrm{T}, \tag{2.4}$$

where $d_{0\ hkl}$ is the lattice spacing of the film at the initial temperature T_0, $d_{1\ hkl}$ is the lattice spacing at final temperature T_1, and α is thermal expansion coefficient. The same applies to the corresponding lattice spacing of the substrate.

2.1.3 Interface Coherence

Interfaces are classified into three categories according to the atomic structure [Hull1984]: coherent, semi-coherent and incoherent (Fig. 2.1). For coherent interfaces, the lattice mismatch of the adjacent crystals is small enough, that adjacent lattice planes continue periodically across the interface. Coherent interfaces are often formed at the early stages of the epitaxial

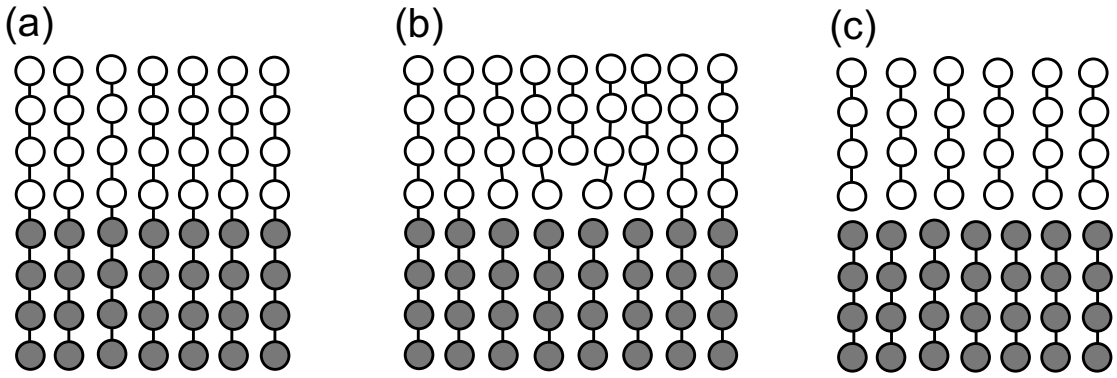

Figure 2.1: Schematic drawing of (a) a coherent, (b) a semi-coherent and (c) an incoherent interface structure.

film growth with the film material adopting the lattice spacing of the substrate crystal (Fig. 2.1a). If the strain energy at the interface exceeds a critical value, a periodic misfit dislocation network forms with the misfit dislocations separating coherent interface regions (Fig. 2.1b). In the case of an incoherent interface (Fig. 2.1c) no localized strain fields exist. Since both materials retain their equilibrium lattice spacings, no periodicity across the interface occurs. It is also possible to describe this case as a semi-coherent interface with delocalized misfit dislocations cores [Romanov1998].

2.1.4 Coincidence Site Lattice Model

The coincidence site lattice (CSL) was originally introduced for the description of grain boundaries. It represents a pure geometrical model of fitting two crystals at the interface. To produce the CSL, one crystal lattice is placed on top of the other crystal lattice so that in one point at the interface the lattices coincide. One lattice is then rotated with respect to the other one. For specific orientations between the two lattices, a higher number of coincidence sites can occur. The coincidence sites produce a new periodical structure with the unit cell size Σ, which is equal to an integer number of unit cells of the initial lattices. It is assumed that an interface between two crystals has a low energy, when the density of coincidence sites is high, and, therefore, the Σ value is low. Detailed descriptions of the CSL model are given by Bollmann [Bollmann1970], Smith and Pond [Smith1976], and by Sutton and Balluffi [Sutton1987].

The CSL model for grain boundaries can also be applied for interfaces with different lattice parameters on both sides. In that case, an exact coincidence is usually not possible. A near coincidence site lattice (NCSL) is then used, where the deviations from the exact coincidence are included. The density of the near coincidence sites depend on the misorientation angle.

In the present work, a 2-dimensional NCSL was used to calculate possible in-plane orientation relationships between the film and the substrate. The coincidence sites are mathematically defined through linear translation vectors, which connect the origin with the neighboring sites [Bollmann1970]:

$$\mathbf{T_f} = k\mathbf{a_1} + l\mathbf{a_2}, \tag{2.5}$$

$$\mathbf{T_s} = m\mathbf{b_1} + n\mathbf{b_2}, \tag{2.6}$$

where $\mathbf{a}_1$, $\mathbf{a}_2$ are unit vectors of one lattice, $\mathbf{b}_1$, $\mathbf{b}_2$ are the unit vectors of the other lattice and k, l, m, n are integers. The exact coincidence appears at

$$|\ \mathbf{T_f}| = |\ \mathbf{T_s}|. \tag{2.7}$$

In the case of NCSL, a degree of coincidence misfit δ has to be introduced:

$$\delta = \frac{2(\mathbf{T}_{Mo} - \mathbf{T}_{STO})}{\mathbf{T}_{Mo} + \mathbf{T}_{STO}}. \tag{2.8}$$

The quantity δ denotes how well the atoms of one lattice are placed on top of the atoms of the second lattice at the coincidence sites. Further details are given in the Appendix A and Section 6.2.1.

2.2 Growth of Thin Films

The growth of epitaxial thin films on different substrates is a process that depends on a variety of parameters, such as substrate temperature, adsorption and desorption rates, surface energies of the film and the substrate and interface energy of the system. Bauer developed a simple model to describe various growth processes [Bauer1958]. He suggested three phenomenological growth modes that are based on energetic considerations only.

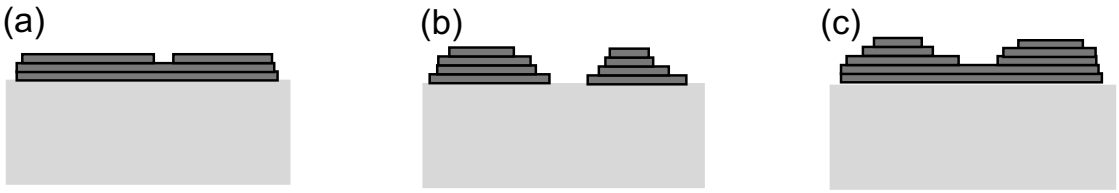

Figure 2.2: Three different mechanisms of thin films growth: (a) Frank-van-der-Merwe growth (layer-by-layer growth mode), (b) Volmer-Weber growth (3D island growth mode), and (c) Stranski-Krastanov growth (combined layer-by-layer and island growth mode).

The first mode is the "layer-by-layer", or 2-dimensional growth mode, where the growth of the next layer begins only after the previous layer is completed (Fig. 2.2a). This growth mode is referred as Frank-van-der-Merwe (FM) growth mode [Merwe1993]. It occurs if the formation of the interface is energetically more favored than the formation of the free surface. The second growth mode is called Volmer-Weber (VW) growth mode [Merwe1993]. In this mode, the film grows 3-dimensionally (3D) by forming islands on the substrate surface (Fig. 2.2b). It is energetically favorable for the film to form a free surface instead of increasing the interface. The third mode is called Stransky-Krastanov (SK) growth mode and is characterized by a combined layer-by-layer and island growth (Fig. 2.2c). At the initial stage of growth, a continuous layer with a thickness of 1-3 ML is formed. The further growth proceeds by 3D islands growth. This growth mode often occurs when a film is strained. The strain can occur due to a large lattice mismatch between the film and the substrate [Merwe1993], strong bonding between the materials or when electronic interactions between the film and the substrate materials take place [Merwe1993, Doben1988, Gossman1991].

Bauer [Bauer1958] suggested also a criterium, which allows to determine the expected growth mode. The "Bauer criterium"was derived from the Young-Dupré equation considering only thermodynamical and energetic factors.

The Young-Dupré equation (2.9), which is valid for the case of a liquid drop on a solid substrate and isotropic surface energies, is given by:

$$\gamma_{sf} = \gamma_s - \gamma_f \cdot \cos(\Theta), \tag{2.9}$$

were γ_s and γ_f are substrate and film surface energies, respectively, and γ_{sf} is the interface

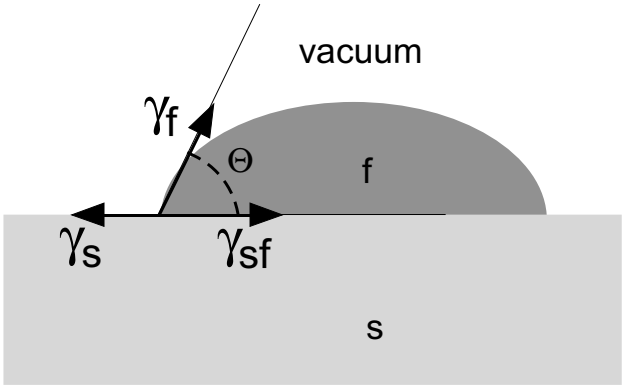

Figure 2.3: Schematic drawing of a liquid metal drop on a solid substrate. In thermodynamic equilibrium the angle Θ is defined through the surface energies γ_s and γ_f, and the interface energy γ_{sf}.

energy. The angle Θ denotes the contact angle (see Fig. 2.3). The liquid drop-substrate system is considered to be in thermodynamical equilibrium. The Bauer-criteria for the different growth modes can be represented as it is summarized in Table 2.1. Here, γ_{strain} is the strain energy stored in the film.

However, for solid/solid interfaces such as metal/ceramic interfaces, surface energies are anisotropic. Therefore, small crystals will create facets along low-indexed crystallographic planes to minimize the total surface energy [Winterbottom1967]. The shape of the crystal is given by the Wulff-construction [Wulff1901]. Due to the anisotropy of the surface energy, the Young-Dupré equation has to be modified:

$$\gamma_{sf} = \gamma_s - \gamma_{f(hkl)} \frac{r_2}{r_1}, \tag{2.10}$$

where $\gamma_{f(hkl)}$ is the surface energy of the (hkl)-facet and r_1 and r_2 are the distances between

Table 2.1: Bauer-criteria for different growth modes. γ_{strain} is the strain energy stored in the film.

$\Theta = 0$, $\gamma_{strain} \ll \gamma_f$	$\gamma_{sf} \leq \gamma_s - \gamma_f$	FM (2D) growth mode
$\Theta > 0$	$\gamma_{sf} > \gamma_s - \gamma_f$	VM (3D) growth mode
$\Theta = 0$, $\gamma_{strain} \gg \gamma_f$	$\gamma_{sf} \leq \gamma_s - \gamma_f$	SK (combimed) growth mode

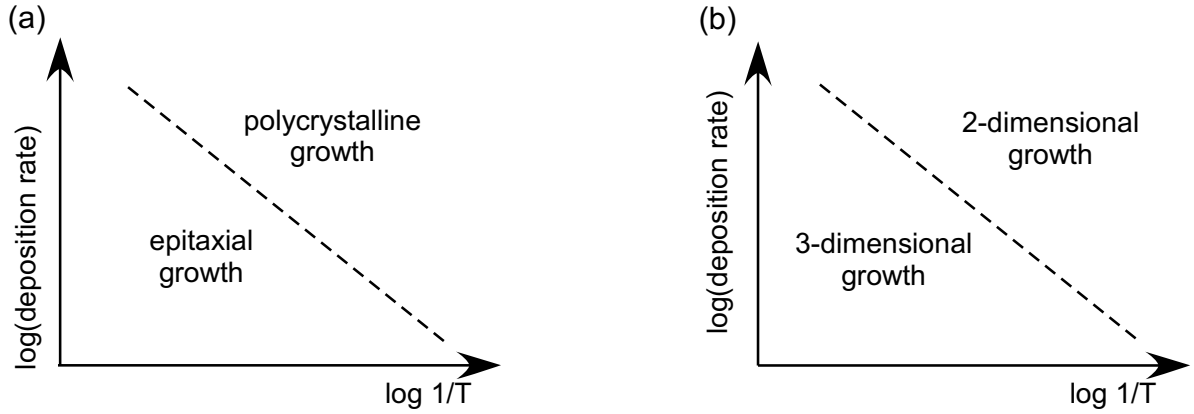

Figure 2.4: Sketches of the different thin films growth modes as a function of deposition rate and substrate temperature $T_{substrate}$ after Richter [Richter2000]. Both axes are on a logarithmic scale.

the particles surface and interfacial planes to the Wulff point, which is given by the center of the particle symmetry.

Molecular beam epitaxy (MBE) deposition disturbs thermodynamic equilibrium through the influence of the substrate temperature $T_{substrate}$ and the deposition rate. Therefore, the Bauer criterium has to be extended. Markov and Kaishew [Markov1976] derived such a modified criterium by introducing the oversaturation parameter $\xi = \frac{R_a(T_{substrate})}{R_d(T_{substrate})}$, which is the ratio of adsorbed (R_a) and desorbed (R_d) ad-atoms on the substrate surface at the temperature $T_{substrate}$ [Merwe1993]. In the region of low values of ξ (high $T_{substrate}$ and low deposition rate) the ad-atoms can easily reach energetically favored sites on the surface. The growth in this case occurs near the thermodynamic equilibrium, and the film grows with an epitaxial orientation relationship to the substrate. For high ξ values (low $T_{substrate}$ and high deposition rate), the diffusion length of the ad-atoms becomes shorter, which can lead to polycrystalline growth far from the thermodynamic equilibrium. The growth mode of the film is also influenced by ξ. The lower the deposition rate and the substrate temperature, the more favorable will be a 2-dimensional Van-der-Merwe type growth mode (see Fig. 2.4).

2.3 Properties of Film and Substrate Materials

Structures and properties of single-crystalline bulk $SrTiO_3$, Pd and Mo are outlined in this section (see also Table 2.2).

Table 2.2: Properties of $SrTiO_3$, Pd and Mo.

Parameter	**$SrTiO_3$**	**Pd**	**Mo**
Structure	cubic perovskite	fcc	bcc
Lattice parameter, [nm]	0.3905	0.389	0.3147
Space group	Pm3m	$Fm\bar{3}m$	$Im\bar{3}m$
Atomic number	38, 22, 8	46	42
Elastic modulus, E [GPa]	189.7	121	329
Thermal expansion coefficient α, [10^{-6}·K]	$\alpha_{293K} = 10.3$	$\alpha_{293K} = 11$	$\alpha_{293K} = 4.8$
Melting point, [°C]	2080	1554	2615
Oxygen affinity, pO = $-log\ p_{O_2}$		-1.1	20.1
Possible oxidation states		2, 4	6, 5, 4, 3, 2
Electronegativity [Pauling scale]		2.2	2.1
Valence electron configuration		[Kr]$4d^{10}$	[Kr]$5s^1 4d^5$

2.3.1 Bulk $SrTiO_3$

$SrTiO_3$ crystallizes at room temperature in the cubic perovskite structure [Landoldt1981, Nassau1988] with a lattice spacing of $a = 3.905$Å. It belongs to the space group $Pm3m$. The atomistic structure is described by the atomic basis with the atoms at the following positions: Sr[0,0,0], Ti[$\frac{1}{2}$,$\frac{1}{2}$,$\frac{1}{2}$], and O[$\frac{1}{2}$,$\frac{1}{2}$,0], [$\frac{1}{2}$,0,$\frac{1}{2}$], [0,$\frac{1}{2}$,$\frac{1}{2}$] [Landoldt1981]. The Ti^{4+} ions are six-fold coordinated by O^{2-} ions, while the larger Sr^{2+} ions are surrounded by four of such Ti-O-octahedra (Fig. 2.5). For the (100) surface, two surface terminations are possible, formed by SrO and TiO_2 planes, respectively (Fig. 2.5). At lower temperatures the structure undergoes phase transitions. At 105K the Ti-O-octahedra become slightly

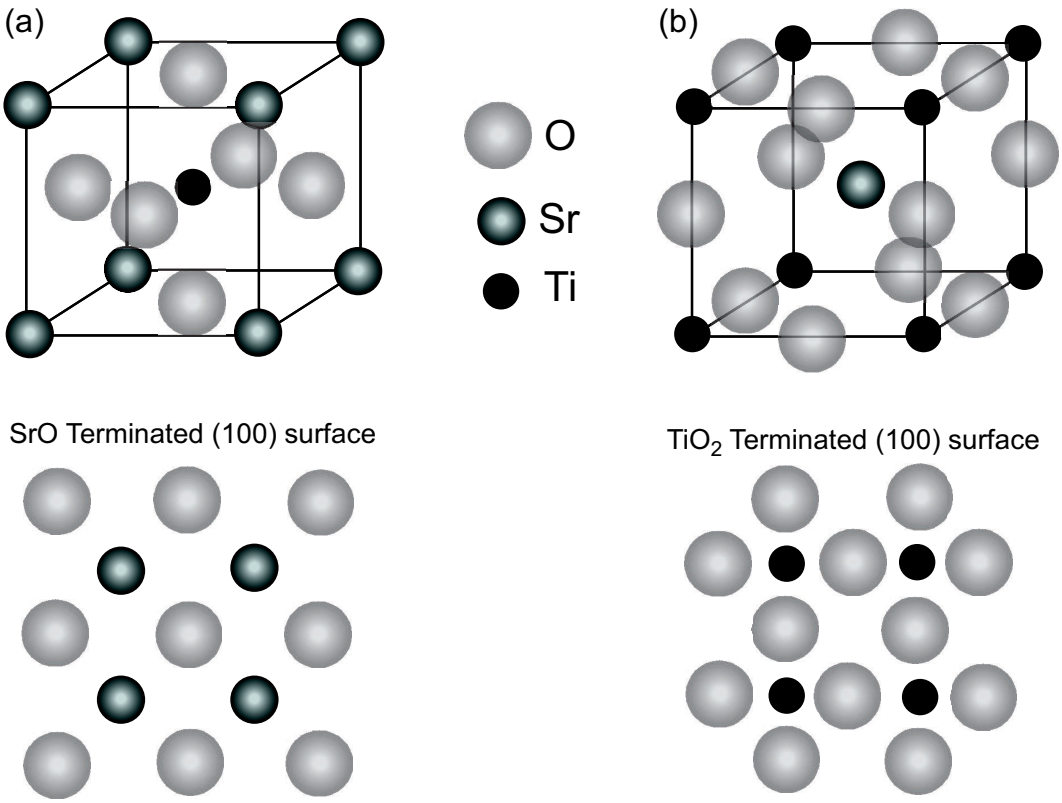

Figure 2.5: Crystal structure of $SrTiO_3$ at room temperature (a=3.905Å): (a) with the Ti atom in the center of the cube and corresponding SrO surface termination of the (100) $SrTiO_3$ surface, (b) with the Sr atom in the center and corresponding TiO_2 termination of the (100) $SrTiO_3$ surface.

distorted, which leads to the formation of the tetrahedral structure (space group $I4/mcm$ [Heidemann1973, Fujishita1979]). At 65K the structure becomes orthorhombic [Lytle1964].

Pure $SrTiO_3$ is an insulator with a band gap of 3.17eV [Cardona1965, Waser1990a, Waser1990b] and mixed ionic-covalent bonds formed by nominal Sr^{4+}, Ti^{2+} an O^{2-} ions. The presence of intrinsic defects, e.g. vacancies, or extrinsic defects, e.g. dopants, can modify the electronic structure and conductivity of the ceramic.

2.3.2 Metals

Thin films of two different metals, namely palladium (Pd) and molybdenum (Mo), were investigated in this work. Table 2.2 summarizes some of their properties.

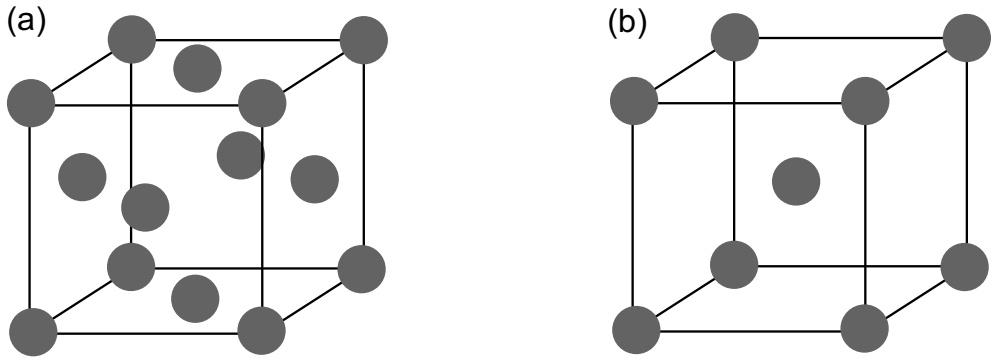

Figure 2.6: Crystal structure of (a) face-centered cubic and (b) body-centered cubic materials.

Palladium

Pd crystallizes in the face-centered cubic structure (Fig. 2.6a) with a lattice parameter of $a = 3.89$Å at room temperature (RT). With the atomic number Z=46 it belongs to the 10^{th} group of the periodic table. Its atomic valence electron configuration is [Kr]$4d^{10}$. The cube-on-cube orientation relationship to the $SrTiO_3$ with the surface plane (100) has a lattice misfit of only $f = -0.4\%$ (see Eqn. 2.2).

The heat of oxide formation has a lower value compared to Mo (Table 2.2). Therefore, the probability of a reaction at the interface is significantly low.

Molybdenum

Mo crystallizes in the body-centered cubic structure (Fig. 2.6a) with a lattice parameter of $a = 3.147$Å at RT. It is located in the 6^{th} group of the periodic table and has a valence electron structure [Kr]$5s^1 4d^5$. The lattice misfit between Mo and $SrTiO_3$ for the cube-on-cube orientation is $f = +24\%$. A reduction of the misfit is achieved when the interfacial plane of Mo is the (110) plane. In this case, and if the $\langle 110 \rangle$ Mo direction is parallel to the $\langle 100 \rangle$ $SrTiO_3$ direction, a misfit value of $f = -12\%$ is obtained.

From the values of the heat of oxide formation and oxygen affinity (Table 2.2) it can be inferred that Mo has a higher probability to react chemically with the $SrTiO_3$ than Pd.

Chapter 3

Literature Overview

In the following chapter, investigations of metal/oxide interfaces are reviewed. The focus is made on articles regarding different metals deposited on $SrTiO_3$ substrates as well as studies where Pd and Mo metals are deposited onto different oxide substrates.

3.1 Metals on Oxide Substrates

Metal/cermic interfaces are widely studied in literature. As an oxide substrate, MgO, TiO_2, Al_2O_3 and $SrTiO_3$ are often used, while most of the deposited metals belong to the 3d and 4d transition metals and alkali-metals. Preparation techniques, such as internal oxidation [Meijering1971], diffusion bonding [Fischmeister1993, Elssner1990], and molecular beam epitaxy [Tsao1993] are applied to produce the metal/ceramic joints. The publications concerning the studies of metals on $SrTiO_3$ are reviewed in Subsection 3.1.2. Subsections 3.1.3 and 3.1.4 present an overview of investigations on Pd/oxide and Mo/oxide systems, respectively. In the metal/oxide systems, the termination of the oxide substrate is essential, since it can affect the interface structure. Therefore, the literature relevant to the surface preparation of $SrTiO_3$, used as a substrate in the present work, is reviewed in Subsection 3.1.1.

3.1.1 $SrTiO_3$ surface preparation

The preparation of the $SrTiO_3$ surface prior to metal deposition is crucial, since it affects the termination of the surface and, thus, the atomic and electronic structure of the produced

metal/$SrTiO_3$ interfaces. Different preparation techniques exist for obtaining particular surface terminations: (i) Ar^+ sputtering of the surface [Henrich1978, Adachi1999], (ii) annealing of the $SrTiO_3$ crystals for one or several annealing cycles [Matsumoto1992, Tanaka1994], and (iii) chemical etching procedures [Kawasaki1994].

The Ar^+ sputtering process was found to introduce defects, such as oxygen or strontium vacancies, into the $SrTiO_3$ surface [Henrich1978, Adachi1999]. These defects do not annihilate even if an additional annealing treatment is performed [Henrich1978, Adachi1999].

A single annealing cycle was applied to $SrTiO_3$ crystals by Matsumoto *et al.* and Tanaka *et al.* [Matsumoto1992, Tanaka1994]. The crystals were heated in UHV to a temperature of T=1200°C. Both SrO and TiO_2 terminations, and regularly stepped surfaces were observed after the annealing procedure. In addition, owing to loss of oxygen in the UHV, a $(\sqrt{5} \times \sqrt{5})$ surface reconstruction caused by oxygen vacancies diffusion was found. Jiang and Zegenhagen [Jiang1996] applied a two step annealing cycle. The specimens were first annealed in an oxygen atmosphere for several hours at a temperature of T=1100°C, and then further annealed for approximately 2 hours in UHV at T=950°C. The resulting surface showed the presence of terraces with a c(6×2)-reconstruction.

Kawasaki *et al.* prepared well-defined (100) $SrTiO_3$ surfaces by etching with a HF-acid [Kawasaki1994]. The HF-acid was buffered with NH_4F, resulting in a pH-value of 4.5. Applying this technique, the authors were able to produce a regularly stepped surface with step heights of 0.39 nm (1 unit cell). The steps height depends on the angle of misorientation. After etching, the surface was found to be completely TiO_2-terminated [Kawasaki1994, Yoshimoto1994], compared to the 75-95% TiO_2 termination before the etching. To obtain a SrO-terminated surface, one monolayer of SrO had to be deposited on the $SrTiO_3$ surface after the etching procedure [Kawasaki1994].

Polli and co-workers [Polli1999] found that a combination of etching and annealing techniques allows the production of well defined (100) $SrTiO_3$ substrates that exhibit a TiO_2 surface termination with homogenous steps of about one unit cell in height.

3.1.2 Metals on $SrTiO_3$

In the following subsection, investigation performed on metal/$SrTiO_3$ systems are described. Most of these studies are focused on the growth behavior and epitaxy of the deposited films [Chung1979, Kawada1999, Polli2000, Jackson1994, Kido2000, Benthem2002, Benthem2002a, Fu2001, Fu2002, Hill1989, Conard1996, Andersen1990]. The variable parameters are substrate termination, substrate temperature, processing method and reactivity of the deposited metal. For the characterization of the interfaces, surface science methods such as reflection high-energy electron diffraction (RHEED), atomic force microscopy (AFM), auger electron spectroscopy (AES), X-ray photoelectron spectroscopy (XPS), scanning electron microscopy (SEM), scanning tunnelling microscopy (STM), scanning tunnelling spectroscopy (STS), and X-Ray diffraction (XRD) techniques were applied. Only a few publications report transmission electron microscopy (TEM) investigations of the interfaces in cross-section [Andersen1990, Conard1996, Benthem2002, Benthem2002a].

Pt/$SrTiO_3$

Chung and Weissbard [Chung1979] investigated the composition, structure and electronic properties of $SrTiO_3$ surfaces and Pt/$SrTiO_3$ interfaces. Prior to Pt deposition, a detailed analysis of the $SrTiO_3$ (100) surface was performed. The surface was cleaned by Ar^+ ion bombardment and than annealed at different temperatures. Different surface science techniques, namely AES, low energy electron diffraction (LEED), surface electron energy loss spectroscopy (EELS), ultraviolet photoelectron spectroscopy (UPS) and AES were applied. A 1×1 surface reconstruction of the $SrTiO_3$ and loss of Sr from the surface above 240°C were observed. During the deposition of Pt at room temperature, *in situ* AES measurements showed a charge transfer from Ti to Pt. LEED experiments revealed some degree of ordering of Pt on the substrate surface [Chung1979]. The measurements were performed for film thicknesses of 1, 2 and 3 ML respectively.

Kawada and co-workers [Kawada1999] investigated the high-temperature transport properties at Pt/$SrTiO_3$ interfaces. A layer of 50 nm Pt was deposited on the $SrTiO_3$ (0.5wt% Nb-doped) at $T_{substrate}$=700°C by laser ablation. Kawada and co-workers detected the for-

mation of a Schottky barrier after annealing the specimen in pure oxygen at a temperature T $\geq$ 500°C. The authors suggested that the barrier formation is strongly related to the oxygen transport in the $SrTiO_3$.

One of the first systematic growth studies of metals on differently terminated $SrTiO_3$ substrates were performed by Polli and co-workers [Polli2000]. They investigated the growth of Pt on both TiO_2 and SrO terminated (100) $SrTiO_3$ surfaces. The lattice mismatch between Pt and $SrTiO_3$ is $f = 0.4\%$. To produce SrO terminated $SrTiO_3$, 0.5ML and 2ML of Sr, respectively, were deposited onto the substrates prior to the Pt deposition [Polli2000]. The growth was monitored by *in-situ* RHEED and AES. A 3-dimensional growth and islands faceting were detected. The morphology and the structure of the metal/substrate interface were investigated by XRD, AFM and cross-sectional TEM techniques. The orientation relationship between Pt and $SrTiO_3$ was predominantly cube-on-cube for TiO_2 terminated surfaces, where the corresponding planes and directions of both cubic crystals are parallel to each other. For the SrO terminated specimens with 0.5 ML SrO coverage, it was found that the Pt (100) plane is parallel to the (100) $SrTiO_3$ plane. In contrast, specimens covered with 2 ML SrO had the Pt(111) plane parallel to the (100) SrO plane. This change in OR for the 2ML SrO terminated surface is due to the lower total energy for the Pt(111)/(2ML SrO)$SrTiO_3$ interface in comparison to the Pt(100)/(0.5ML SrO)$SrTiO_3$ interface [Polli2000].

Ni/$SrTiO_3$

Jackson and co-workers [Jackson1994] performed thermodynamical calculations of the Gibbs free energy changes for the oxidation at the metal/ceramic interface. The goal was to determine the conditions for the buffer layer oxide deposition, under which the oxidation of the metallic substrate does not occur. One of the investigated systems was $SrTiO_3$ thin films deposited on pure Ni substrates. The authors reported that under reducing conditions (with respect to nickel oxide) the Ni can be kept in the metallic state. It is stable against the oxidation from the $SrTiO_3$ side at the Ni/$SrTiO_3$ interface during the $SrTiO_3$ buffer layer deposition. However, the deposition rates as well as the surface entropies and surface enthalpies are not considered.

Kido and co-workers [Kido2000] investigated the surface structure of $SrTiO_3$ and the

structure of the interface between 1ML Ni/(001)$SrTiO_3$ by high-resolution MEIS, UPS and RHEED techniques. The $SrTiO_3$ surface was etched in a NH_4F-HF buffer solution with $pH = 3.5 - 3.8$ [Kido2000] and than annealed in an oxygen atmosphere in order to obtain a TiO_2 terminated surface. The fraction of TiO_2 termination was $(88 \pm 2)\%$ for annealing temperatures below 650°C. Medium-energy ion scattering (MEIS) measurements of the samples annealed for 1h in UHV at 650°C showed that about 14% of the O sites are vacant, which decreases the amount of the TiO_2 termination by $5 - 6\%$. At room temperature, 1ML of Ni was deposited on the predominantly TiO_2 terminated (100) surface. RHEED measurements revealed a random distribution of Ni atoms over the substrate surface [Kido2000]. The metallic nature of the Ni was confirmed by UPS measurements. After annealing for 0.5h at 400°C in UHV, the formation of Ni clusters was observed.

Van Benthem and co-workers [Benthem2002, Benthem2002a] investigated in more detail the Ni/$SrTiO_3$ system. The same substrate preparation techniques as those described by Polli et al. [Polli1999] were used. The film morphology was studied using conventional TEM methods revealing 3-dimensional island growth and a cube-on-cube epitaxial orientation relationship between the film and the substrate. The metal/ceramic interface structure was observed by high-resolution TEM (HRTEM), while the electronic structure and the bonding mechanism was investigated by means of spatially resolved EELS measurements. No excessive reaction layer was detectable at the interface. However, the detailed EELS analysis showed that a 2-dimensional NiO layer might be present at the interface.

For the Ni/$SrTiO_3$ interfaces, an reaction layer was not observed by HRTEM [Benthem2002, Benthem2002a], even though EELS studies indicated the presence of a 2D NiO layer. Kido and co-workers [Kido2000], in turn, found that 1 ML of Ni deposited on either TiO_2 or SrO terminated $SrTiO_3$ stays in the metallic state. The theoretical calculations [Jackson1994] confirmed that the interface reaction for the Ni/$SrTiO_3$ system strongly depends on the deposition conditions. Nevertheless, the atomic structure of the Ni/$SrTiO_3$ interface could not be analyzed.

Cr/$SrTiO_3$

Fu and Wagner [Fu2001, Fu2002] investigated the growth and thermal stability of Cr layers deposited on (100)$SrTiO_3$ using in situ RHEED, XPS and STM techniques. The surface of $SrTiO_3$ was prepared following the method of Kawasaki et al. [Kawasaki1994]. Cr deposition at RT resulted in the formation of clusters. After annealing below 640°C a reorientation of the randomly orientated clusters occurred, leading to a well defined rotated cube-on-cube orientation relationship. For temperatures above 600°C, oxygen diffused from the bulk $SrTiO_3$ into the surface and an epitaxial chromium oxide phase formed. After heating above 700°C an interdiffusion of the Cr clusters into the substrate was observed [Fu2001]. Film deposition at different substrate temperatures resulted in different epitaxial ORs. Nevertheless, in all cases, a Volmer-Weber growth mode was reported [Fu2001].

Van Benthem [Benthem2002] also investigated the Cr/$SrTiO_3$ system. Cr was deposited on the (100) surface of $SrTiO_3$ at a substrate temperature of 65°C. A 3-dimensional growth mode was detected by RHEED. The density of islands was found to be higher compared to the one observed for Ni. A coalescence of the Cr islands was found with increasing film thickness. In contrast to Ni, a cube-on-cube orientation relationship with a 45° in-plane rotation was observed. HRTEM observations revealed an abrupt interface without any presence of a reaction phase. Energy loss near-edge structure (ELNES) indicated the formation of Cr-O bonds at the interface and an oxidation of the interfacial Cr atoms.

The reported studies of the Cr/$SrTiO_3$ system showed that the reaction at the interface is strongly dependent on the substrate temperature during the deposition [Fu2001, Fu2002, Benthem2002]. However, Fu *et al.* [Fu2001, Fu2002] did not perform any TEM investigations in order to confirm their RHEED and STM results.

Y, Ba and Ti on $SrTiO_3$

Hill *et al.* [Hill1989] investigated interfaces between $SrTiO_3$ and different deposited metals using XPS. The $SrTiO_3$ surface preparation was done by Ar^+ ion sputtering followed by annealing at 500°C for $\sim$ 12 hours and at 900°C for 30 minutes. The resulting ordered (Ar^+-sputtered and annealed at 900°C, 1×1 reconstructed) and disordered (Ar^+-sputtered and annealed at 500°C, nearly stoichiometric but without long-range order) $SrTiO_3$ surfaces were

used for the metal films deposition.

Ti/$SrTiO_3$: Ti was deposited on the ordered substrate. XPS data showed a characteristic shift of the Ti2*p* lines, which was interpreted by Hill and co-workers [Hill1989] as complete oxidation of the 0.12 nm thin Ti film. For thicker films, the XPS results suggested that the O atoms concentrated near the buried interface with decreasing O concentration towards the film surface.

Y/$SrTiO_3$: Y3*d* XPS spectra showed similar to Ti energy shift with increasing film thickness. For 0.05 nm thickness, the binding energy value was equal to that of yttrium oxide. For thicknesses of about 3.5 nm a metallic state of the Y was detected. A linear decrease of the XPS intensities stemming from the substrate was observed with increasing film thickness, which indicates a 2-dimensional growth mode of Y on $SrTiO_3$.

Ba/$SrTiO_3$: The XPS measurements revealed a behavior of the Ba similar to that of Ti and Y, indicating the reaction at the Ba/$SrTiO_3$ interface. Also a 2-dimensional layer-by-layer growth was observed.

In their report, Hill and co-workers [Hill1989] describe only the oxidation of Ti, Y and Ba at the contact with the $SrTiO_3$. Data concerning the morphology and structure of the film are not reported.

Cu/$SrTiO_3$

Hill and co-workers [Hill1989] also investigated the Cu/$SrTiO_3$ system by XPS technique. In contrast to Ti, Y and Ba, Cu did not react with ordered or disordered $SrTiO_3$ (100) substrates. A non-exponential decrease of the core-level intensities indicates a 3-dimensional growth of Cu. The islands coalescence begins above 8 nm thickness. A gradual shift of the binding energy is observed as the continuous Cu layer is formed.

Conrad *et al.* [Conard1996] investigated the formation of the Cu/$SrTiO_3$ interface with the Cu film deposited on reduced and stoichiometric $SrTiO_3$ surfaces. The growth mode of Cu was determined by combining XPS and high-resolution EELS methods. A 2-dimensional-like Cu layer interacting with the substrate and the Cu islands, similar to the Stranski-Krastanov growth mode was found. Using the stoichiometric surface of $SrTiO_3$ resulted in a lower defect density in the film and a larger size of the the Cu islands compared to the reduced surface.

The calculations of the spectra were also performed by the authors. The results confirmed the oxidation of the first layers of the deposited Cu, which was observed during the experiment. The formation of a CuO_2-like oxide was detected. The metallic nature of the Cu developed with increasing film thickness, which was also in accordance to the experimental observations [Conard1996].

Andersen and Mller [Andersen1990] investigated ultra-thin Cu films deposited by electron beam evaporation on the 1×1 $SrTiO_3$ (100) surface at room temperature. Surface analysis techniques such as AES, surface EELS, XPS and UPS were applied. During the deposition, a 3-dimensional Volmer-Weber growth mode was observed. A well-defined orientation relationship between the film and the substrate was not detected. The energy bands were not bent at the interface, which was interpreted by the authors as a result of the weak bonding between Cu and $SrTiO_3$.

The studies mentioned above use similar surface analysis methods to describe the growth of Cu films and the bonding behavior to the substrate. Conard et al. [Conard1996] observed a Stranski-Krastanov growth mode, whereas Andersen and Møler [Andersen1990] found a Volmer-Weber growth mode. However, no imaging techniques such as TEM or SEM were used to confirm these data. Such differences in growth mode as well as the differences in bonding strength can be related to different preparation processes and different deposition temperatures. The formation of specific orientation relationships are not investigated in all three reports. The conclusions on the bonding behavior are made only qualitatively.

Pd/$SrTiO_3$

Ochs *et al.* [Ochs2000] performed detailed theoretical investigations of the projected bonding distance, bonding behavior and energetics of the Pd/$SrTiO_3$ interface using *ab initio* calculations. Four different structure models were assumed for the calculations. Two models had a TiO_2 termination of the $SrTiO_3$ with Pd atoms sitting on top of either O atoms (TiO_2/Pd-O model) or Ti atoms and hollow sites (TiO_2/Pd-Ti,gap model). For the other two models a SrO terminated $SrTiO_3$ had Pd atoms positioned on top of either Sr and O atoms (SrO/Pd-Sr,O model) or above the hollow sites (SrO/Pd-gap model). The authors found that the TiO_2 termination is energetically favorable due to the possibility of arranging

all Pd atoms of the unit cell at the energetically favorable O adsorption sites [Ochs2000]. In the most stable configuration, the Pd atoms should sit directly above the O atoms. This induces strong Pd-O bonds, however some weak Pd-Ti bonds occur in addition. For the SrO termination, strong interactions between Pd and O were observed, while the Sr interacts only weakly with O ions. This leads to a shift of the Sr atoms into the substrate interior when the Pd is placed above the hollow sites between two O and two Sr atoms [Ochs2000]. No pronounced bonds between the Pd and the substrate were detected in this case. For the TiO_2/Pd-Ti,gap and SrO/Pd-Sr,O models, the positioning of Pd on the two different adsorption sites was found to result in strong Pd buckling [Ochs2000].

Van Benthem [Benthem2002] analyzed the bonding across the Pd/$SrTiO_3$ interface by EELS and ELNES techniques. Also, the symmetry and site projected density of states at the Pd/$SrTiO_3$ interface was calculated in order to quantify the ELNES results. The same structure models proposed by Ochs et al. [Ochs2000] were used for the calculations. The best agreement between the experimental ELNES data and the calculated projected density of states was found for the case, where the $SrTiO_3$ is TiO_2 terminated. Strong Pd-O bonds and some weak Pd-Ti bonds were detected [Benthem2002].

The theoretically predicted TiO_2 terminated interface structure [Ochs2000] was found to describe the electron spectroscopic results of Van Benthem [Benthem2002]. However, so far no imaging techniques were applied to prove the proposed atomic structure at the interface. This includes a quantitative evaluation of the translation state, which should be then compared to the predicted value of Ochs *et al.* [Ochs2000].

3.1.3 Pd/Oxide Systems

A large number of investigations has been performed on Pd/Oxide interfaces owing to the high importance of such interfaces in catalytic systems. Studies related to the present work are summarized in Table 3.1. The publications that describe the growth of Pd on cubic substrates are discussed in more detail in the following section. The studies on systems with low symmetry substrates (such as rhombohedral α-Al_2O_3, hexagonal ZnO, etc.) are of a minor interest for the present work and thus are not considered further.

Table 3.1: Overview of the investigations, performed on Pd/Oxide systems. $T_{substrate}$ denotes the substrate temperature during the growth, VW and SK stand for Volmer-Weber and Stranski-Krastanov growth modes, respectively.

Substrate	Pd Film OR	Growth Mode	$T_{substrate}$	Interface Reaction	Methods of Investigation	References
(100)MgO			$< 1550°C$	yes	TEM	[Moodie1977]
(100)MgO	(100)	VW	300°-400°C		TEM,SAD	[Takayanagi1978]
(100)MgO	(100)	VW	300°-400°C		TEM	[Chapon1985]
(100)MgO	(100),(111)	VW	1025°C	no	TEM,HRTEM	[Lu1992]
(100)MgO	(100)	VW	$\sim 400°C$		TEM	[Henry1992]
$(1\bar{1}1)$MgO		VW	1000°C	yes	HRTEM	[Chen1995]
(100)MgO	(100)	pseudo-SK	250°C		AES/HeD	[Goyhenex1996]
(100)MgO	(100)	VW	20°C		TEM,GIXS, SEELFS	[Renaud1999]
(100)MgO					theory	[Matveev1999]
(100)MgO					theory	[Goniakowski1998]
(100)MgO					theory	[Goniakowski1999a]
(111)MgO					theory	[Goniakowski1999b]
(110)TiO_2	(100)/(110)	SK	27°C		LEED,XPS,IAS	[Evans1996]
(110)TiO_2		VW	$\sim 80°C$		STM,STS	[Xu1997]
(110)TiO_2					theory	[Bredow1999]
(0001)Al_2O_3	(111)	VW			STM	[Hansen1999]
(0001)Al_2O_3					theory	[Lodziana2002]
(0001)Al_2O_3					theory	[Gomes2003]

Pd/MgO

Moodie and co-workers [Moodie1977] studied the reactions at the interface between Pd and (100)MgO by TEM. The reaction phase was found to exhibit liquid-like characteristics at temperatures below the melting point of both interface components (T< 1554°C). Upon cooling, the reaction phase remained amorphous. The substrate was strain-free during the reaction process as well as after different cooling procedures. However, the authors were not able to determine the structure and composition of the intermediate phase.

The epitaxy of different metals on (100)MgO were investigated by Takayanagi *et al.* [Takayanagi1978] using *in situ* TEM and electron diffraction. They found a systematic dependence of the orientation relationship between the film and the substrate on the geometrical ratio of the lattice parameters film/substrate. The Pd/MgO system with a ratio $a_{Pd}/a_{MgO} = 0.924$ belongs to the group of metal/MgO systems with $a_{deposit}/a_{substrate} < 1$. For this group, a cube-on-cube OR was found.

The growth and morphology of Pd films deposited on (100)MgO substrates were studied by Henry *et al.* [Chapon1985, Henry1992, Goyhenex1996] using TEM and AES techniques. The deposition temperature was varied between 130° and 400°C. SAD experiments revealed a cube-on-cube orientation relationship between (100)Pd and the oxide substrate. The Pd particles were found to be randomly distributed at the initial growth stage [Chapon1985]. The combination of different experimental techniques allowed to determine unambiguously the 3-dimensional Volmer-Weber growth mode of Pd [Chapon1985]. At room temperature, Goyhenex and co-workers [Goyhenex1996] observed a pseudo-2-dimensional growth for metal coverages below 1 ML.

Lu and Cosandey [Lu1992] and Chen and co-workers [Chen1995] performed TEM investigations at Pd/MgO(100) and Pd/MgO(111) interfaces. The interfaces were found to be atomically smooth without any evidence of a reaction phase. The dislocation networks observed by HRTEM were explained by CSL/DSC geometrical models. The dislocations strain fields were found to be limited mostly to the metal side.

The structure and morphology of Pd films grown at RT on atomically flat surfaces of MgO(100) was investigated by Renaud et al. [Renaud1999] using *in situ* grazing incidence X-ray scattering (GIXS). Pd was found to grow in the 3-dimensional mode, and a cube-

on-cube epitaxy was observed. At the initial growth stages the lattice parameter of Pd was lying between bulk Pd and MgO. The islands stayed coherent to the substrate up to 4-5 ML thickness of Pd. The strain relaxation is explained by the authors through lattice relaxations at the edges and the free surfaces of the Pd islands. Above the thickness of 5 ML, the formation of misfit dislocations was observed. The film becomes continuous at approximately 35 ML thickness. The O ions were determined to be the adsorption sites for the Pd atoms, with an interfacial distance of (2.22 ± 0.03 Å) between Pd and MgO.

Goniakowski [Goniakowski1998] applied *ab initio* full-potential linear muffin-tin-orbital calculations to the Pd/MgO(100) interface in order to investigate the atomistic and electronic structure. For 1 ML of Pd on top of MgO, the Pd was found to nucleate on top of the O atoms with a bonding distance of 0.218 nm. The author states that preferential positioning is determined not by the chemical bonding, but rather by the polarization of the Pd atoms in the substrate field. The tendency of preferential adsorption of the metal atoms on top of the oxygen atoms is reported by Goniakowski for all $4d$ transition metals [Goniakowski1999a]. For the (111)MgO surface, Goniakowski and Noguera [Goniakowski1999b] found that the Pd adsorption characteristics are controlled by the strong polar character of the (111)MgO surface and, thus, differ from those determined for the (100)MgO surface [Goniakowski1998]. Strong electron transfer and/or orbital hybridization between the Pd atoms and the MgO substrate take place, including significant changes of the local density of states near the Fermi level [Goniakowski1999b].

Matveev and co-workesr [Matveev1999] also calculated the electronic and atomistic structure at the Pd(100)/MgO interface by means of gradient-corrected density functional theory. The adsorption of the Pd atoms was found to be stronger on non-charged O vacant sites compared to regular O^{2-} sites. The Pd-O bonding distance was determined to be 2.11. This theoretical value is smaller than the experimental one determined by Renaud et al. [Renaud1999] due to the "zero-coverage limit", which was set in the theoretical calculations of Matveev and co-workers [Matveev1999].

In summary, there exists a large number of publications concerning both theoretical and experimental aspects of the growth behavior of Pd on top of MgO and of the atomistic and electronic structure of the Pd/MgO interface. Most of the authors observed 3-

dimensional Volmer-Weber growth of Pd even at different growth conditions. The pseudo-Stranski-Krastanov growth mode reported by Goyhenex [Goyhenex1996] was observed only for a coverage below 1 ML, which contradicts the results of Renaud et al. [Renaud1999]. The theoretical investigations provide the basis for understanding the Pd nucleation process. The experimental and theoretical values for the bonding distance correspond to each other within the restrictions applied to the theoretical calculations [Renaud1999, Matveev1999]. However, there are no experimental investigations correlated with the theoretical studies of the Pd adsorption behavior.

Pd/TiO_2

Evans and co-workers [Evans1996] grew Pd layers on TiO_2(110) substrates by metal vapor deposition and investigated them with LEED and XPS techniques. Below 3 ML of Pd coverage the authors did not observe any significant ordering of Pd ad-atoms. Additional annealing at 200°C led to the formation of Pd clusters with a size up to 1 nm. At intermediate coverages of 10-20 ML the nucleation process was observed at RT. Heat treatment at 200°C led again to the formation of metal clusters which are highly dispersed on the substrate surface. In addition (111)Pd facets were observed. The authors state that the growth mode is of the Stranski-Krastanov type.

Xu et al. [Xu1997] investigated the growth and structure of Pd/TiO_2(110) by STM and STS. The Pd was deposited under UHV conditions at room temperature on (1×1)-reconstructed (110) surfaces of TiO_2. The growth mode was determined to be of the Volmer-Weber type. The investigation of the Pd adsorption on the TiO_2 surface revealed that the adsorption sites align themselves to the 5-fold coordinated Ti rows. The STS investigations of the electronic structure exhibited a transition from the non-metallic to the metallic nature of the Pd atoms. The clusters had sizes of about 250-350 atoms.

Bredow and Pacchioni [Bredow1999] applied a gradient-corrected density functional theory to determine the interaction of Pd atoms and dimers with the (110)TiO_2 surface. The calculations demonstrated that for a full Pd coverage, the O sites are energetically favored. For isolated Pd atoms or dimers, the Ti sites are preferred. The authors related this difference to an effect of the interactions between different adatoms. The correlation effects between Pd

atoms are responsible for the choice of the nucleation site. No charge transfer was observed at the Pd/TiO_2 interface, indicating that the bonding between the metal and the ceramic is covalent.

The studies reported in this section reveal a 2-dimensional growth of Pd on TiO_2 up to a coverage of 3 ML [Bredow1999, Evans1996]. At higher coverages (above 10 ML), 3D growth was detected [Evans1996]. Heating experiments [Evans1996, Xu1997] showed the formation of 3D Pd clusters. However, no experimental results on the bonding behavior or electronic structure at the interface were reported.

3.1.4 Mo/Oxide Systems

Since Mo is used in various technological applications, such as gate electrodes, diffusion barriers and buffer layers, a large number of investigations of different Mo/ceramic systems exists. Most of the studies concentrate on the deposition, growth behavior and morphology characterization of the films. The literature, which is of interest for the present work, is summarized in the Table 3.2.

Mo/MgO

Swedberg and co-workers [Svedberg1999] investigated the epitaxial growth of magnetron sputtered Mo films on (001)MgO substrates using *in situ* LEED, RHEED and STM techniques. They observed the presence of O on the Mo surface during initial growth stages, which lead to the reconstruction of the film surface with $(\sqrt{5} \times \sqrt{5})$R26°33′, p$(2 \times 2)$ and c(2×2) structures. The Mo films were single crystalline, exhibiting a 45°-rotated cube-on-cube orientation relationship with the MgO substrate. For film thicknesses below 20 nm, a coherent growth was observed.

Mo films grown by laser ablation on MgO (001) substrates were studied by Guilloux-Viry and co-workers [Guilloux1996] with RHEED, SEM and XRD techniques. STM was used to investigate the surface roughness of the films. Similar to Swedberg *et al.* [Svedberg1999], the authors observed a rotated cube-on-cube orientation relationship between Mo and MgO for films grown at 970°C. For intermediate deposition temperatures, a (110) Mo orientation

Table 3.2: Overview of the investigations, performed on Mo/Oxide systems. $T_{substr.}$ denotes the substrate temperature during the growth.

Substrate	Mo Film OR	Misfit	$T_{substr.}$	Interface Reaction	Methods of Investigation	References
(001)MgO	(001)single	5.6%	850°C	-	LEED,STM,RHEED,XRD	[Svedberg1999]
(001)MgO	(001),(110)	5.6%	970°C	-	XRD,RHEED	[Guilloux1996]
(001)MgO	bcc and fcc phases		20°C-600°C	-	RHEED/THEED,AES	[Kacim1994]
(001)MgO	fcc phase	-	-	-	SED/TED	[Denbigh1966]
(110)TiO_2	-	-	20°C	yes	AES,XPS,AFM,RHEED	[Petigny1999]
(110)TiO_2	-	-	20°C	yes	AES,XPS,AFM,RHEED	[Domenichini2000]
(110)TiO_2	-	-	50°C	yes	STM	[Kitchin2003]
(110)TiO_2	(110)texture	3.2-6.3%	20°C	no	XRD,HRTEM,XPS	[Blondeau2002]
$(11\bar{2}0)Al_2O_3$	(110)single	-	130°C	no	LEED,LEEM	[Swiech1999]
$(11\bar{2}0)Al_2O_3$	(110)single	-	570°C	-	RHEED,STM	[May2001]
$(0001)Al_2O_3$	(111)single	-	800°C	-	RHEED,SPM	[Ryan1999]

with the formation of two 90° rotated micro-domains was detected by RHEED and verified by STM measurements.

The formation of fcc phase in ultra-thin Mo films grown on MgO substrates was reported in early work of Denbigh and Marcus [Denbigh1966]. Using scanning electron diffraction during the film deposition, the authors observed the formation of fcc Mo as well as disordered structures during the initial stages of growth. Both structures were found to transform into the bcc phase as the film thickness increased. The bcc structure occurred at a thickness of about ~ 4 nm. The lattice parameter of the fcc Mo ranged between $0.419 - 0.427$ nm. The authors describe the Mo film growth mode as 3-dimensional, forming fcc nano-crystallites. Kacim and co-workers [Kacim1994] performed systematic growth and structure studies of Mo films deposited on (100)MgO substrates using different substrate temperatures. Thermal evaporation and direct current (d.c.) sputtering techniques were used to produce the films. The authors also reported the formation of fcc as well as bcc phases of Mo, depending on the film deposition method and sputtering rates. The lattice parameters of fcc Mo were found to

vary between 0.415 and 0.422 nm. The authors claim that the presence of non-metal elements O, N and C is responsible for the stabilization of the fcc Mo structure [Kacim1994].

All four reported investigations showed 3-dimensional growth of the Mo on the (100)MgO surface. For film thicknesses below 20 nm a coherent growth was observed [Svedberg1999]. The Mo orientation towards the substrate was found to be dependent on the deposition temperature [Guilloux1996]. The observation of the fcc Mo formation is claimed to be related to the presence of O, C and N impurities on the substrate surface during the metal deposition [Kacim1994]. However, Denbigh and Marcus [Denbigh1966], who also observed fcc Mo, found that the impurity concentration in the Mo films does not exceed $2-3$ at.%, while for the formation of a stable compound the impurity level should reach 30 at.%. They concluded, that the fcc/bcc phase transformation is most likely a general phenomena, but did not describe the mechanism of the fcc structure formation. No TEM and HRTEM studies were performed to investigate the metal/ceramic interface in detail.

Mo/Al_2O_3

May *et al.* [May2001] studied the deposition of Mo buffer layers on $(11\bar{2}0)$ Al_2O_3 substrates. *In situ* RHEED results suggested the formation of large 2-dimensional Mo terraces after the deposition of $\sim$ 16 nm of Mo. The growth direction of Mo was determined from RHEED pattern to be parallel to $\langle 110 \rangle$. Only one single epitaxial OR between the Mo film and the Al_2O_3 substrate was found. STM experiments revealed the formation of small Mo islands with an averaged diameter of 20 nm.

Święch and co-workers [Swiech1999] characterized Mo films on $(11\bar{2}0)Al_2O_3$ substrates by LEED. As-grown films contained low-angle grain boundaries, which vanished after annealing the specimens at 1500°C. The produced single-crystalline Mo film exhibited monoatomic surface steps and terraces. The authors found that the stress in the Mo film, which appears owing to the different thermal expansion of Mo and alumina, is relieved through slip along the $\langle 111 \rangle$Mo direction in the $(110)_{Mo}$ plane. The formation of interfacial screw dislocations was also observed.

Ryan et al. [Ryan1999] investigated the epitaxial growth of (111)Mo on $(0001)Al_2O_3$ substrates and its dependence on the growth temperature and deposition rate. *In situ* RHEED

and scanning probe microscopy methods were applied. At the initial growth state, the roughness of the Mo surface was found to depend strongly on the combination of both growth parameters. The RHEED patterns indicated 3D growth of fully relaxed Mo islands up to nominal thickness of $\sim$ 5 nm. The nominal thickness of $\sim$ 1 nm was described as a stable thickness: the Mo islands of this height delayed further coarsening until all other island reach the same thickness. However, the mechanism that leads to the appearance of the stable thickness was not reported by the authors [Ryan1999].

All three investigation reported in this section, describe mainly the growth behavior and the orientation of the Mo films relative to the substrates. The Mo was found to grow in a 3-dimensional mode, and the OR between the film and the substrate was dependent on the substrate surface plane orientation. Święch et al. [Swiech1999] described the stress relief, conveyed by the formation of interface dislocations. However, the authors did not performed any HRTEM analysis of the interface and dislocation structure. The bonding behavior at the interface was not investigated.

Mo/TiO_2

The film structure and composition of 40 nm thin Mo films grown on (110)TiO_2 rutile single crystalline substrates was analyzed by Blondeau-Patissier and co-workers [Blondeau2002] using XRD technique. The Mo/TiO_2 interface was investigated by HRTEM. The formation of a preferred (110)Mo film texture was observed for both air-annealed and oxygen-bombarded TiO_2 substrates. During the HRTEM and EDS investigations no amorphous MoO_X phase layer was detected at the interface between Mo and the substrate.

Pétigny *et al.* [Petigny1999] and Domenichini *et al.* [Domenichini2000] studied by *in situ* AES and XPS and *ex situ* AFM and RHEED methods the deposition of Mo on different TiO_2(110) surfaces. The surfaces had different stoichiometries: (i) normal (stoichiometric, obtained by Ar^+-bombardment, 2/1 O/Ti ratio) and (ii) non-normal (obtained by O_2^+-bombardment, small O reduction). The results indicate the Stranski-Krastanov growth mode, with the first 3 ML consisting of amorphous molybdenum oxide with Mo either in Mo^{3+} or Mo^{4+} oxidation states. Further growth proceeded as island growth of metallic Mo independently of the substrate surface treatment. The 2D growth of Mo at the initial stage

was found to be associated with electronic exchanges between Ti^{4+} and deposited Mo^0. The oxidation of Mo induces a TiO_2 surface reconstruction through the generation of Ti^{2+} and Ti^{3+} in the near-surface region of the substrate. In the case of pre-reduced substrates, the reduction of Ti was observed to migrate into the bulk TiO_2, while for the stoichiometric surface the reduction retained localized in the interface layers.

The growth and sintering behavior of Mo nanoparticles on a $TiO_2(110)$ single crystalline substrates with 1×2 reconstructed surfaces was studied by Kitchin and co-workers [Kitchin2003]. The main investigation technique was STM. The results show that the Mo film grows in a 3-dimensional mode. Different annealing times were applied to investigate the thermal behavior of the Mo particles. Flash annealing up to 500°C resulted in an increasing particles size (from 2 nm to $\sim$ 2.7 nm). In contrast, if the specimens were annealed for 20 h at the same temperature the small particles vanished and the formation of large anisotropic particles was observed. After 60 min annealing time the alignment of the particles along the $\langle 100 \rangle TiO_2$ direction was found. The anisotropic shape of the particles is reported to be due to the rearrangement of the particles in order to maximize their interaction with surface O rows. From the data on the heat of reaction for TiO_2 and Mo the authors conclude that partial oxidation of Mo and partial reduction of the oxide substrate at the metal/oxide interface are feasible.

The studies reported by Pétigny et al. [Petigny1999], Domenichini et al. [Domenichini2000] and Kitchin et al. [Kitchin2003] revealed the local oxidation of Mo at the interface. Pétigny et al. [Petigny1999] reported Stranski-Krastanov growth mode of Mo, where the first 3 ML consist of amorphous molybdenum oxide. Blondeau-Patissier et al. [Blondeau2002] did not observe any significant reaction layer at the Mo/TiO_2 interface by HRTEM. The authors explained this by the higher deposition rate and lower substrate temperature than in the previous studies, so that the oxidation process was kinetically hindered.

3.1.5 Investigations of the Electronic and Atomic Structure at Metal/Oxides Interfaces

Electronic Structure and Chemical Bonding Investigations

Only a limited number of experimental investigations exists, where the electronic structure and chemical bonding at metal/ceramic interfaces is determined. In these studies, mainly STEM and EELS techniques were used.

Brydson *et al.* [Brydson1995] and Scheu *et al.* [Scheu1995, Scheu1996a, Scheu1998] have performed extensive investigations of the electronic structure of Al/Al_2O_3 and Cu/Al_2O_3 interfaces. Spatially resolved ELNES measurement using the spatial difference technique [Bruley1993, Mullejans1995] were applied to determine the chemical bonding and the electronic structure at the different interfaces. For the Al/Al_2O_3 system it was found that the interfacial Al atoms are coordinated by three O atoms. The Al-Al bonding length was found to be shorter than the Al-O bonding length. For the Cu/Al_2O_3 system, Cu-O bonds with Cu in its normal +1 oxidation state were observed at the interface.

Detailed spatially resolved EELS/ELNES investigations of the Cu/MgO system are reported by Muller *et al.* [Muller1998] and Imhoff *et al.* [Imhoff1999]. Both authors determined that the (111) plane of MgO was terminated by O. However, Muller and co-workers [Muller1998] found that metal-induced gap states (MIGS) at the MgO side reduce the charge redistribution across the interface. In their study, the interface does not show a Cu_2O-type electronic structure. Imhoff and co-workers [Imhoff1999], on the other hand, detected a pronounced charge transfer at the Cu/MgO interface. The features of Cu-L ELNES spectra were found to correspond to those of Cu_2O with Cu in Cu^{1+} state. The O-K edge was also modified. The authors concluded that Cu-O bonds are formed at the Cu/MgO interface [Imhoff1999].

For the metal/perovskite interfaces, the EELS/ELNES analysis of the local electronic structure at the interface was performed by van Benthem [Benthem2002, Benthem2002a] for the $Pd/SrTiO_3$, $Ni/SrTiO_3$ and $Cr/SrTiO_3$ systems as described in Section 3.1.2. At the $Pd/SrTiO_3$ interface he found the formation of Pd-O bonding together with much weaker Pd-Ti intermetallic bonding. Similar results were obtained for $Ni/SrTiO_3$ and $Cr/SrTiO_3$

interfaces.

In most studies mentioned above, a charge transfer across the interface was found, which lead to strong metal-oxygen bonds [Brydson1995, Scheu1995, Scheu1996a, Scheu1996b, Bruley1993, Mullejans1995, Imhoff1999, Benthem2002]. However, Muller and co-workers [Muller1998] did not observe a charge transfer. The authors claimed that metal-induced gap states are formed at the metal/ceramic interface and that the metal atoms remain almost neutral.

Atomic Structure Investigations

In most conventional and high-resolution TEM investigations the main focus was made on the growth behavior of the films, the structure of the interface and interfacial dislocations. The quantitative evaluation of the metal/ceramic interface structure, and the determination of the translation state at the interface is only addressed in a few studies.

Gutekunst et al. [Gutekunst1997] investigated the interface between thin Nb films and different surface planes of α-Al_2O_3 by HRTEM. In order to determine the atomic structure of the interface, the experimental HRTEM micrographs were compared to simulated images. These were obtained by assuming different structure models of the interface. The translation state at the interface was determined using a rigid block displacement method. The study revealed that Nb atoms occupy the Al lattice sites at the interface. The Nb atoms of the second layer adjacent to the interface are positioned close to the Al lattice sites of a continued Al lattice of α-Al_2O_3. Misfit dislocations were observed at the interface to accommodate the lattice mismatch. However, the quantitative HRTEM analysis was not sensitive to the chemical composition at the interface, i.e. to the exchange of all Nb atoms to Al atoms [Gutekunst1997].

Dehm and co-workers [Dehm1997] used a synthesis of analytical and HRTEM techniques to determine the atomic and electronic structure at the interface between Cu and Al_2O_3. To retrieve an interface structure model, image simulations with evolutionary optimization were performed. A periodic configuration of the incoherent Cu/Al_2O_3 interface was assumed. To achieve the periodicity along the interface the Cu (022) lattice spacings were slightly increased. The EELS study indicated that Cu-O bonds establish across the interface.

Therefore, the oxygen-terminated (0001) alumina surface was incorporated into the structure model. Performing iterative structure refinement, the authors found the best agreement between simulated and experimental images for an average projected bonding distance of $\delta = 0.2 \pm 0.03$ nm between the terminating O layer and the first Cu layer [Dehm1997].

Schweinfest and *et al.* [Schweinfest1998] performed a detailed quantitative analysis of the translation state at the (001)Al/(001)$MgAl_2O_4$ interface with picometer-range precision. The authors also used the evolutionary optimization to determine the imaging conditions and initial parameters of the interface. Furthermore, the precise determination of the translation vector components at the interface was performed. Since different imaging parameters may lead to different estimates for the translation vector components, the images of undistorted Al and $MgAl_2O_4$ unit cells in the bulk were simulated for each set of imaging parameters. These images were then evaluated via cross-correlating to the large undistorted bulk area of the corresponding materials. The substrate was found to terminate with Al and O ions. From the translation between the two fitted lattices of Al and $MgAl_2O_4$ the translation state was determined to be (193 ± 5) pm for the actual set of imaging parameters.

The quantitative evaluation of the bonding distance in both Cu/Al_2O_3 and Al/$MgAl_2O_4$ systems showed an increase of the bonding length at the metal/ceramic interface in comparison to the bulk parameters [Dehm1997, Schweinfest1998]. Similar results were found by semi-quantitativ methods for the Nb/α-Al_2O_3 interfaces [Gutekunst1997]. However, in this case the QHRTEM was found to be insensitive to the atomic composition at the interface.

3.2 Goal of the Thesis

Within this thesis, two metals are chosen for the deposition on the $SrTiO_3$ substrates: Pd and Mo, which possess different properties (see Table 2.2). These can be regarded as non-reactive (Pd) and reactive (Mo) in contact with $SrTiO_3$. The aim of the present work is to perform a detailed characterization of the produced metal/$SrTiO_3$ interfaces regarding epitaxy, interfacial reactions and atomic structure at the interface and to compare the results for the reactive and non-reactive system.

Previously, the growth behavior of the Pd/$SrTiO_3$ system has been investigated thoroughly by means of surface analysis and CTEM techniques [Richter2000]. The atomistic and electronic structure at the interface was defined using *ab initio* local density functional theory calculations [Ochs2000, Benthem2002]. Experimentally, the electronic structure was determined by STEM-EELS/ELNES techniques [Benthem2002]. In the present work, methods of quantitative HRTEM and STEM-HAADF are employed in order to obtain experimentally the atomic structure of the interface and to define the translation state at the interface.

The Mo/$SrTiO_3$ system was chosen due to the interesting possibilities of the interface structure (large lattice misfit with $SrTiO_3$) and high reactivity of the metal after theoretical *ab initio* studies were published by Classen [Classen2001]. In the present work, the growth behavior of the Mo/$SrTiO_3$ system is analyzed by means of CTEM techniques, as well as XRD and surface science techniques. HRTEM was applied to determine the grain boundary and interface structure.

The results, obtained from both the reactive and the non-reactive system, should contribute to the understanding of other metal/$SrTiO_3$ interfaces. The correlation between the different microscopy methods and the theoretical calculations obtained in earlier studies is essential in this work.

Chapter 4

Experimental Techniques

In this chapter the experimental techniques that are used in the present work for the characterization of metal/$SrTiO_3$ interfaces are described. The different methods, i.e. XRD, conventional TEM and advanced transmission electron microscopy techniques such as HRTEM and HAADF imaging are described in Sections 4.1 and 4.2. An introduction into the image interpretation techniques is given in Subsection 4.2.3.

4.1 X-Ray Diffraction (XRD)

XRD methods ($\Theta - 2\Theta$-scans, pole figures[1]) were applied in this work to characterize the film texture and to determine the orientation relationship between the metal film and the $SrTiO_3$ substrate. A Philips X'Pert MRD instrument with a proportional counter and a parallel beam, operated at 45 kV was used for the measurements.

$\Theta - 2\Theta$-scans are used to determine which planes are parallel to the interface between the film and the substrate. Only the incident angle Θ is changed during the measurements (Fig. 4.1a). The X-rays diffracted at lattice planes that satisfy the Bragg condition interfere constructively and give rise to the maxima in the $\Theta - 2\Theta$-scan profile.

Subsequently, pole figures (two dimensional stereographic projections) for these planes are measured in order to determine the preferred orientations of crystallites within the film. In this case, a specific angle Θ corresponding to the specific plane under investigation is

[1] measurements were performed by Dipl.-Ing. G. Maier, ZWE-Röntgenbeugung

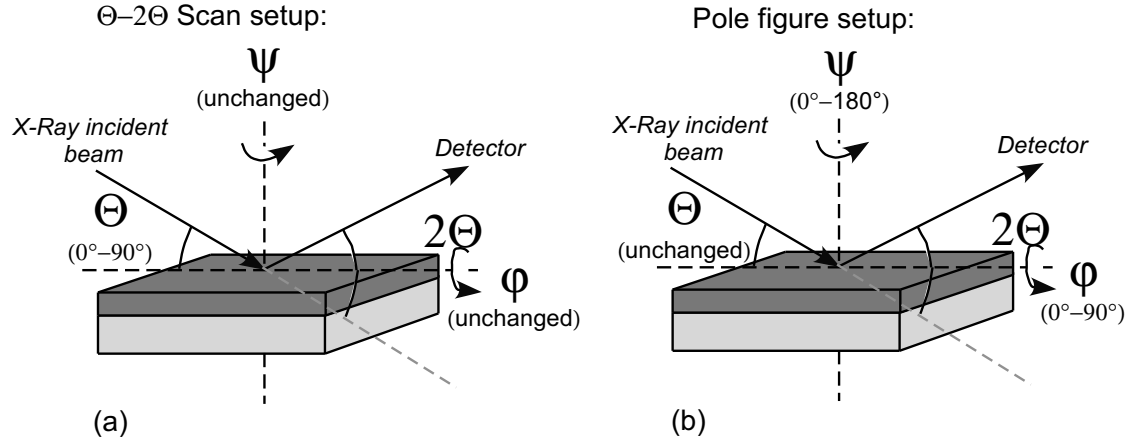

Figure 4.1: Geometry of the XRD experiments: (a) $\Theta - 2\Theta$-scan setup, and (b) pole figure setup .

chosen. The specimen is rotated around the angles φ and ψ (Fig. 4.1b). The intensities coming from the X-rays diffracted by planes in Bragg condition will than be registered by the detector.

4.2 Transmission Electron Microscopy (TEM)

TEM is applied to obtain an image of the specimen at high resolution and magnification. From the different types of TEM techniques, such as selected area diffraction (SAD), bright-field (BF) and dark-field (DF) imaging, high-resolution TEM (HRTEM) and high-angle annular dark field (HAADF, or Z-contrast) imaging, the crystallography and microstructure of the system can be investigated to the finest detail.

In the present study, TEM was the main experimental technique. For the conventional TEM studies a JEOL JEM-2000FX[2] was used. Most of the high-resolution TEM studies were performed on a JEOL ARM-1250[3] with a side-entry pole piece (C_s=2.7mm) [Phillipp1994]. A JEOL JEM-2010F[4] with a side-entry specimen holder (C_s=0.5 mm) was used additionally for the HRTEM investigations. This microscope is also equipped with a scanning unit and a

[2]200 kV accelerating voltage, point-to-point resolution of 0.28 nm, information limit of 0.14 nm
[3]1250kV accelerating voltage, point-to-point resolution of 0.12nm, information limit of 0.09nm
[4]200 kV accelerating voltage, point-to-point resolution of 0.18 nm

JEOL HAADF EM-24015BU detector, which allows to acquire Z-contrast images[5].

4.2.1 Conventional TEM (CTEM)

The ray diagram of a TEM is drawn schematically in Figure 4.2. Two operation modes can be used, i.e. imaging mode and diffraction mode (Fig. 4.2a and b, respectively). In the imaging mode, an image is observed in the image plane, i.e. on the viewing screen (Fig. 4.2a), while in the diffraction mode a diffraction pattern is projected to the viewing screen by changing the strength of the intermediate lens (Fig. 4.2b).

The contrast in conventional TEM is mainly due to diffraction/scattering contrast and mass-thickness contrast. These are based on the scattering cross-section of the atomic species in the specimen and the number of scattering atoms along the propagation of the electron beam. Strongly scattering regions of the specimen (heavy elements, large thickness) show darker contrast in the bright-field image than weakly scattering regions (light elements, small thickness).

A diffraction pattern is formed in the back focal plane of the objective lens (see Fig. 4.2). The diffraction pattern of an amorphous specimen consists of diffuse rings, whereas a crystalline specimen generates diffraction spots. These spots are formed due to the constructive interference between the diffracted beams that fulfill the Bragg condition:

$$\mathrm{n}\lambda = 2d_{hkl} \sin \Theta \ , \tag{4.1}$$

where λ is the wave length, Θ is the Bragg angle, d_{hkl} is the distance between the planes and n is an integer.

Depending on which diffraction spot contributes to the image formation, bright-field (BF) or dark-field (DF) images can be obtained. A BF image is formed, when only the direct beam is selected by the objective aperture, which is inserted in the back focal plane of the objective lens. For obtaining a DF image, the objective aperture is shifted in such a way that only one of the diffracted beams is contributing to the image formation. Since this beam runs off-axis, its electrons suffer from the spherical aberration and astigmatism of the lenses more than the

[5]These experiments were done at the Jošef Štefan Institute (Ljubljana, Slovenia) in cooperation with M. Čeh and S. Šturm.

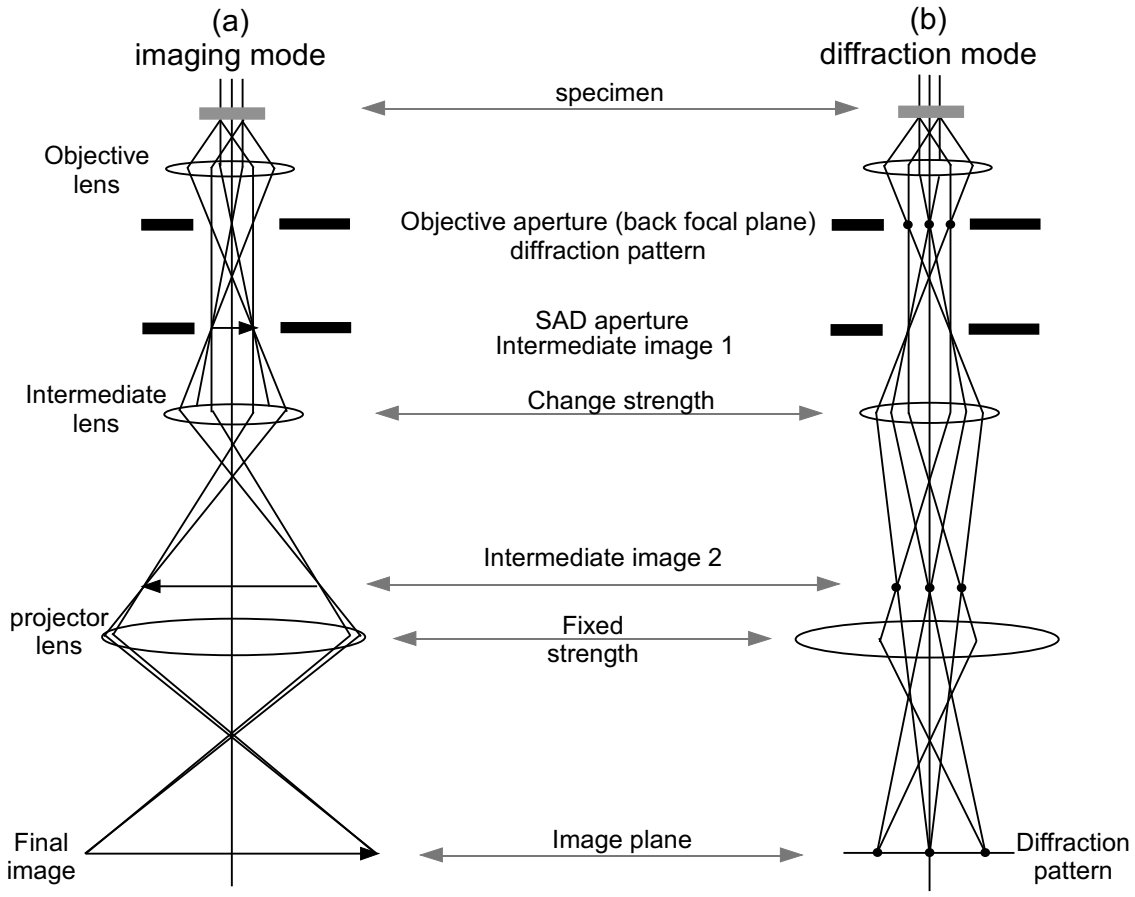

Figure 4.2: Schematic ray diagram of the conventional TEM: (a) projection of the image onto the viewing screen, and (b) projection of the diffraction pattern onto the viewing screen, after Williams and Carter [Williams1996].

paraxially travelling electrons. Thus, the incident beam should be tilted so that the scattered electrons, used for imaging, will travel parallel to the optic axis (angle corresponding to 2Θ with the optic axis). This method is called on-axis DF imaging.

BF and DF images are not images in Abbe's definition [Born1999], since only one beam is used for imaging. The contrast in these images is in the case of a perfect crystal mostly due to the variation of thickness (thickness contours) or the variations in specimen orientation (bending contours). Lattice defects cause bending in their surrounding. This changes also the intensity of the beams that are selected for the image and a defect can be seen in the image. In polycrystalline materials, intensity differences of the individual grains can arise due to diffraction contrast and mass-thickness contrast.

The selected area diffraction (SAD) technique is used to obtain the diffraction pattern

from a selected area of the specimen. To confine the diffraction pattern to the selected region of the specimen, a selected area aperture is used. The aperture is placed in the imaging plane of the objective lens, e.g. the plane where the first intermediate image is formed (Fig. 4.2b). In this case, only beams (transmitted and diffracted) selected by the SAD aperture contribute to the final diffraction pattern, which is projected onto the viewing screen.

The nano-diffraction technique allows obtaining a diffraction pattern from a very small area of the specimen (of about ~ 20 nm in the present work). This is done by focusing the incident beam on the specimen (i.e. focusing the condenser lens) while using the smallest condenser aperture. In this way, the regular diffraction from parallel illumination becomes a convergent beam diffraction, and disks instead of spots are observed on the viewing screen.

4.2.2 High-resolution TEM (HRTEM)

HRTEM allows the investigation of the atomic structure of materials (i.e. defects, grain boundaries, heterophase interfaces). In this work it has been employed for the study of metal/$SrTiO_3$ interfaces. In contrast to CTEM, the HRTEM investigations reveal a magnified image of the specimen in projection up to finest details, i.e. atomic columns. However, the image formation in the HRTEM is a rather complicated process where direct "intuitive"image interpretation often fails.

HRTEM image formation is in accordance with Abbe's theory [Born1999], which states that at least one diffracted beam and the direct beam have to be used to form an image. In order to resolve the fine details of the specimen, i.e. atomic columns, also large values of the $\mathbf{k}$ vector have to contribute to the image. The HRTEM image can be understood as a complex interference pattern of the various diffracted beams and the direct beam. This interference pattern depends on the imaging conditions and the thickness of the specimen.

The direct naive interpretation of the obtained experimental HRTEM micrographs is usually not possible. The main reasons for that are: (i) Strong interactions between the electrons of the incoming electron wave with the Coulomb potentials of the atoms, which leads to dynamic effects, such as multiple scattering, even for small specimen thicknesses. Therefore, the exit wave function can not be easily related to the structure of the specimen. (ii) Due to spherical aberration of the objective lens, the electron rays from outer regions of

the lens are bent more strongly, compared to the electron rays passing the lens in the inner near-axis region. This leads to the formation of disks rather than spots in the image plane. Due to the overlap of the disks, the direct correlation between an image point and an object point gets lost.

These reasons require HRTEM image simulations to retrieve the atomic structure of the specimen. For that, a model of the specimen structure has to be assumed. During the simulations, the microscope parameters are used as an input and image intensity patterns are calculated. A digital comparison between simulated and experimental images is performed, and the initial simulation parameters are varied until the best agreement is achieved. A short description of the image formation in HRTEM and image analysis is given farther below. A more detailed description can be found in [Williams1996, Reimer1984, Spence1981].

Image Formation in HRTEM

The image formation process is sketched in Figure 4.3. In principle it is possible to define two main interactions that contribute to the image formation: (i) an interaction of the incident plane wave with the electrostatic crystal potential and (ii) an interaction between the exit wave function and the microscope lens system (formation of the magnified image of the exit wave function).

The interaction of the incident wave function $\Psi_0(\mathbf{r})$ with the specimen becomes more complicated to calculate as soon as the specimen thickness increases, since dynamical effects (multiple electron scattering) have to be considered. For very thin specimens (1-2 nm) a weak phase object approximation can be applied, where the crystal potential modifies only the phase of the propagating electron wave but not the amplitude. Thus, for the weak phase object the exit electron wave function $\Psi_e(\mathbf{r})$ is "modulated" by the projected two-dimensional crystal potential.

The exit wave function $\Psi_e(\mathbf{r})$ undergoes a Fourier transformation while travelling through the objective lens, i.e. a diffraction pattern is formed in the back focal plane (Fig. 4.3):

$$\Psi_e(\mathbf{k}) = F\Big(\Psi_e(\mathbf{r})\Big). \tag{4.2}$$

Electrons, emitted from the cathode have a certain energy spread (for a LaB_6 cathode in the

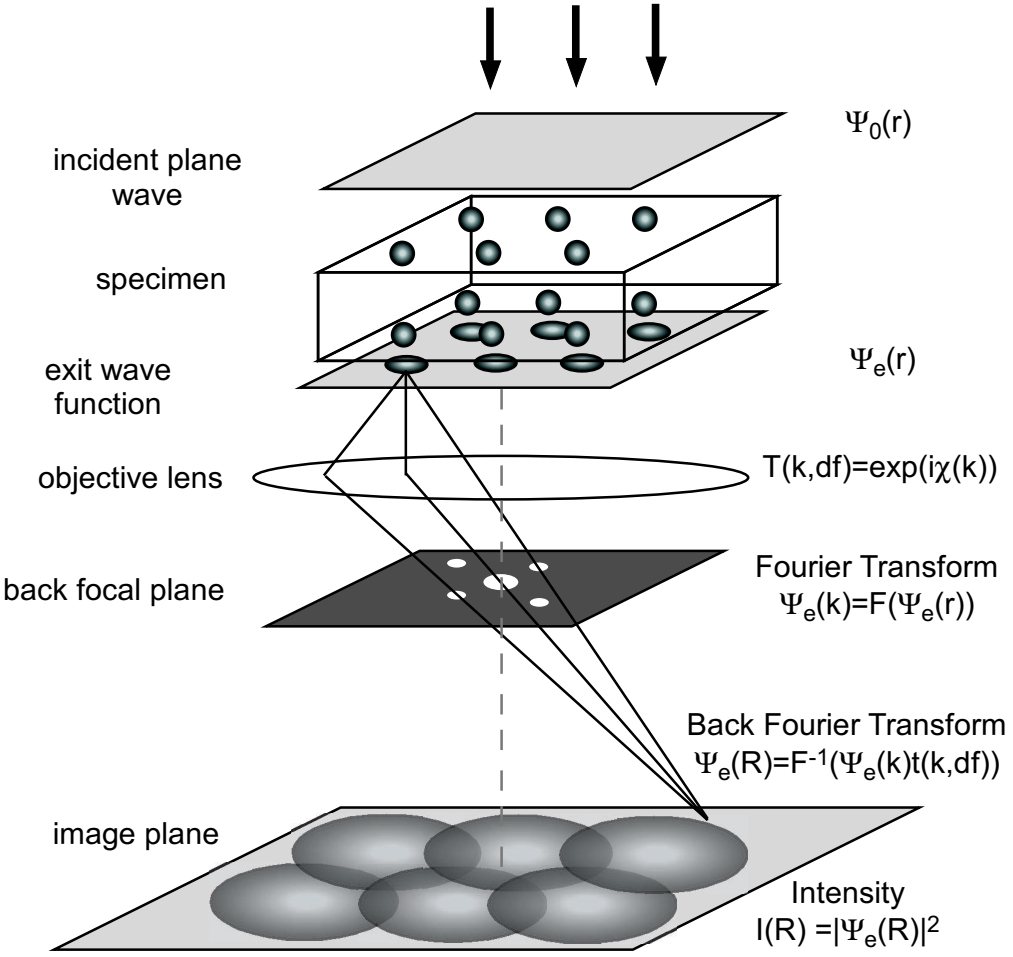

Figure 4.3: Image formation in HRTEM (after Kienzle [Kienzle1999]).

range of ΔE = 1 eV). Instabilities of the high voltage also result in an energy spread. The energy spread, together with the lens current instabilities and aberrations leads to differences in focal length and, thus, to the formation of a disk rather than a point in the image plane (Fig. 4.4). The image plane in this case is defined as a plane, where the paraxial beams are focused. The disk of least confusion is formed in the plane where the diameter of beams intersection is minimal.

The abberations of the objective lens and the defocus are characterized by the aberration function

$$\chi(\mathbf{k}) = -2 \cdot \pi \cdot \left(\frac{1}{4} \cdot C_s \cdot \lambda^3 \cdot |\mathbf{k}^4| - \frac{1}{2} \cdot \lambda \cdot |\mathbf{k}^2| \cdot \Delta f \right), \tag{4.3}$$

where C_s is the spherical abberation of the objective lens, Δf is the defocus, $\mathbf{k}$ is the spatial frequency, and λ is the wavelength. This aberration function is taken into account in the

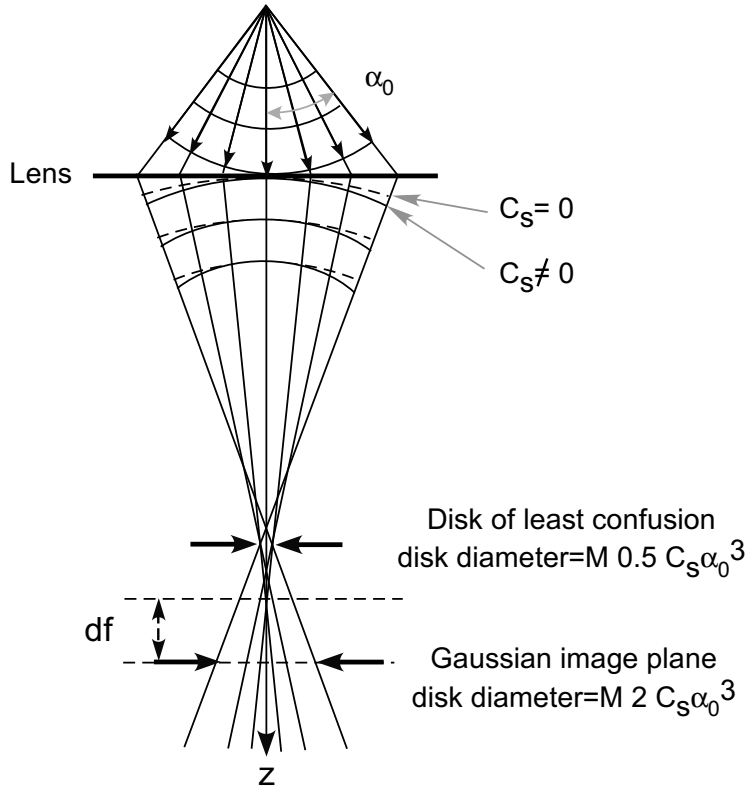

Figure 4.4: Schematic ray diagram showing the effect of the spherical abberation: minimum contrast is obtained at the Gaussian image plane, best imaging condition is achieved by defocusing the objective lens. The parameters M, C_s and α are the magnification, the spherical aberration and the semiangle of collection of the lens.

contrast transfer function (CTF):

$$\mathtt{T}(\mathbf{k}, \Delta f) = exp\Big(i \cdot \chi(\mathbf{k})\Big) \tag{4.4}$$

The CTF $\mathtt{T}(\mathbf{k}, \Delta f)$ describes which spatial frequencies $\mathbf{k}$ are transmitted and thus which atomic spacings can be resolved in the image. Figure 4.5 shows the CTF for the JEM-ARM1250 at Scherzer defocus ($\Delta f_{sch}=(\lambda C_s)^{1/2}$). The value of the Scherzer defocus is defined as the focus value where the pass-band in the CTF is the largest, i.e. where the first intersection of the CTF with the $\mathbf{k}$-axis occurs (CTF=0) at highest frequencies. On the graph (Fig. 4.5 the (113) $SrTiO_3$ spacings with $d_{STO} = 1.18$ Å lie just before the CTF intersection with the $\mathbf{k}$-axis (point-to-point resolution limit).

The CTF multiplied with the Fourier transformed exit wave function $\Psi_e(\mathbf{r})$ describes

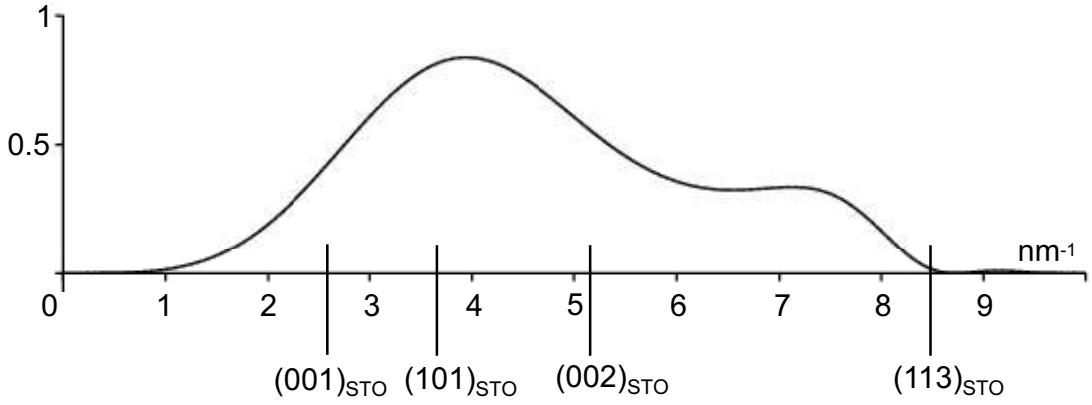

Figure 4.5: CTF of the JEOL JEM-ARM 1250 at Scherzer defocus.

the distribution of the amplitude in the back focal plane of the objective lens. Further wave propagation is described by the back Fourier transformation:

$$\Psi_E(\mathbf{R}) = F^{-1}\Big(\Psi_e(\mathbf{k})\Big) \cdot \mathtt{T}(\mathbf{k}, \Delta f). \tag{4.5}$$

$\Psi_E(\mathbf{R})$ represents the amplitude distribution in the image plane. Since an electron detector registers only the intensity $I(\mathbf{R})$ of interfered electron waves

$$I(\mathbf{R}) = \Psi_E(\mathbf{R}) \cdot {\Psi_E}^*(\mathbf{R}) \tag{4.6}$$

and not the amplitude, the phase information is lost. Therefore, it is not possible to reconstruct an object from the image straight forward and image simulations are required.

4.2.3 Quantitative HRTEM Analysis

As a consequence of the image formation mechanism in HRTEM, it is not possible to interpret the image directly in a naive way (see Section 4.2.2). Here, special techniques are required in order to recover the atomic structure of the specimen, from which the HRTEM image was taken. The structure retrieve is accomplished in this case by considering a known structure, which is expected to be found in the investigated specimen, and simulating the image for this structure. In a further step, the digital comparison of the simulated with the experimental image is performed. The parameters of the simulation can be varied in order to achieve the best match between the simulated image and the experimental images.

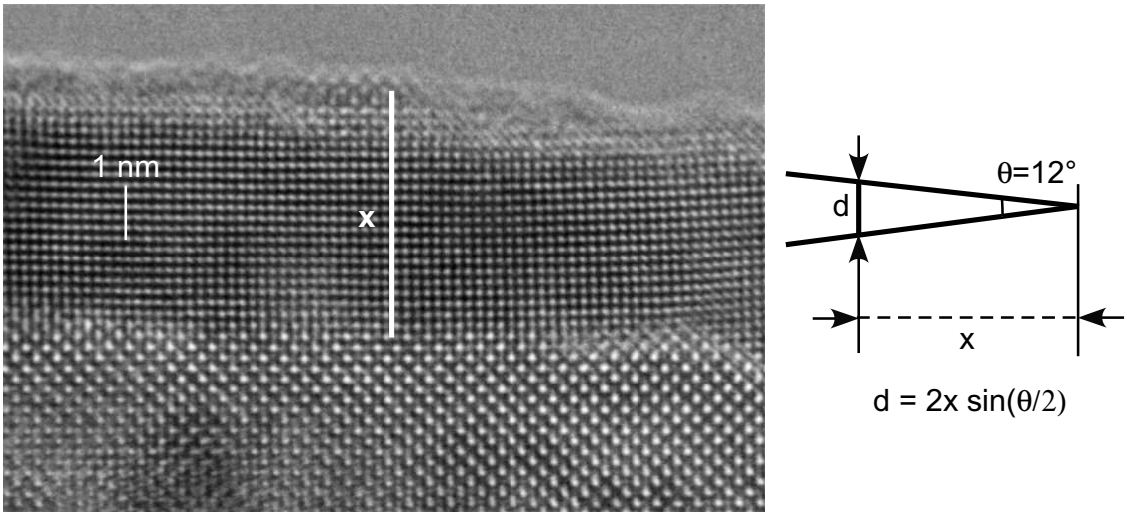

Figure 4.6: Estimation of the specimen thickness at the region of interest.

In the following section, the techniques used for HRTEM image simulations as well as for the determination of initial input parameters for the simulations (specimen thickness, defocus of the microscope, etc.) are described.

Determination of the Initial Input Parameters from the Experiment

Specimen thickness at the interface

From simple geometrical considerations it is possible to estimate the thickness at the region of interest for the case of a perfect crystalline specimen geometry. Figure 4.6 represents the procedure schematically. Here, the distance x from the hole to the interface is known from the micrograph scaling bar. Angle Θ is the angle at which the specimen is bombarded by Ar^+-ions during the ion-milling. Thus, the thickness d for the ideal case can be calculated as $\mathrm{d} = 2\mathrm{x} \cdot \sin(\Theta/2)$. However, it should be mentioned that for metal/ceramic interfaces this method gives only a rough estimation. The thinning rates of two material are different and the final geometry of the specimen edge might be less perfect, than it is drawn in Figure 4.6.

Determination of the defocus value from the experimental image

For the determination of the initial experimental defocus value, an image that includes both amorphous and crystalline regions has to be taken near the area of interest. The same

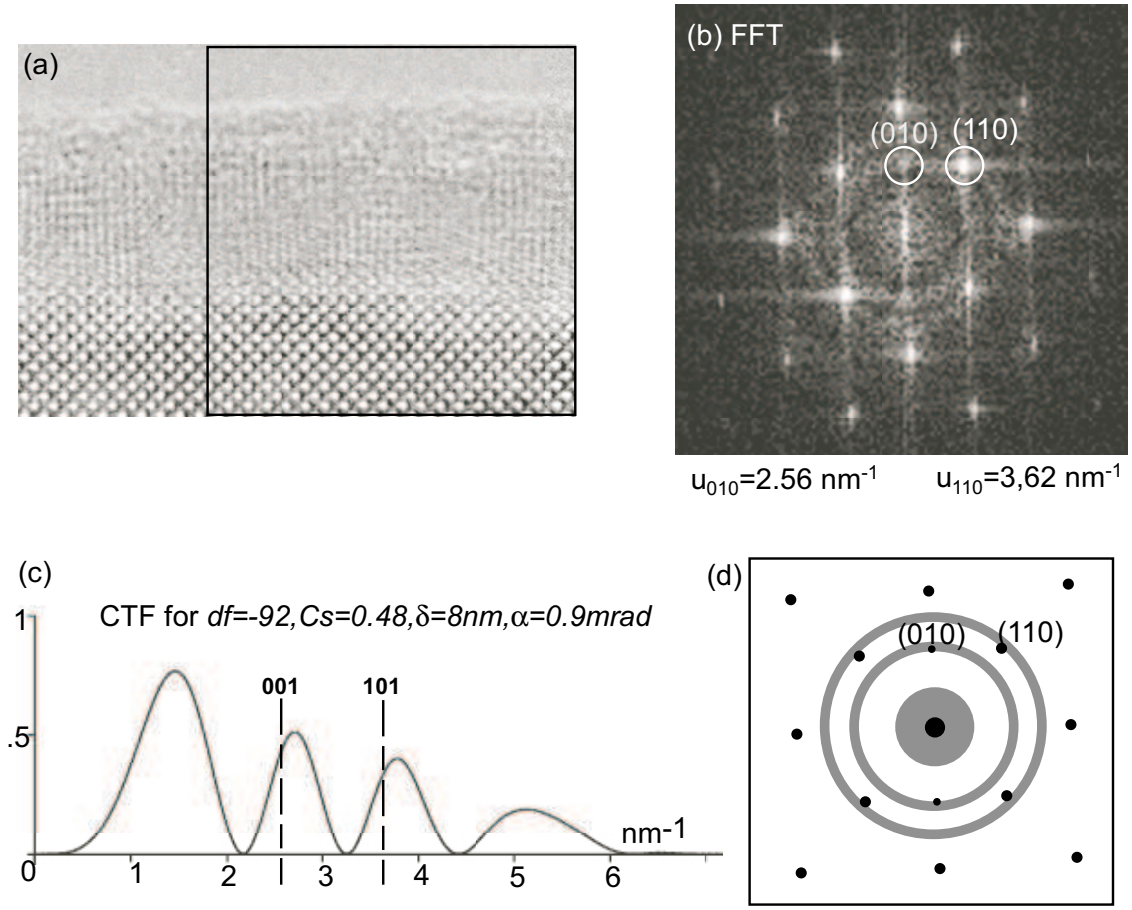

Figure 4.7: Estimation of the defocus value near the region of interest. The part of the HRTEM micrograph, which includes both amorphous and crystalline regions of the specimen is (a) Fourier-transformed, so that the amorphous rings are superimposed on the reflections from the crystalline part (b). The CTF, having minima next to the (010) and (110) $SrTiO_3$ reflections is calculated for the JEM-2010F (c). (d) represents a schematic drawing of the FFT pattern.

imaging conditions under which the HRTEM micrograph was taken have to be applied. The best approach is to obtain both at the same negative, as it was done in this work (Fig. 4.7a). The Fourier transformed image, which is equivalent to the diffraction pattern, is obtained from the HRTEM micrograph. It includes both, amorphous rings and the reflections from the crystalline part (Fig. 4.7b). In this pattern, the individual reflections can be indexed and the **k** values for the particular spots are calculated (Fig. 4.7b). The dark rings at the fast Fourier transform (FFT) pattern correspond to the minima (zero values) of the CTF, and the positioning of these minima in the reciprocal space is sensitive to the changes of the

defocus value. Thus, the CTF for specific conditions of defocus Δf, spherical abberation C_s, spread of focus δ, and beam convergence α can be calculated , as it is shown in Figure 4.7c. Here, the reflections of the (110) and (010) planes of $SrTiO_3$ are lying just at the beginning of the bright rings of the FFT diffractogramm (see schematic drawing in Figure 4.7d). The corresponding calculated CTF for such imaging conditions is represented in Figure 4.7c.

Image Simulations: Calculation of the Exit Wave Function

There are two different methods that enable the calculation of the exit wave function: (i) Bloch waves calculations and (ii) multislice method. In the Bloch wave approach, it is assumed that the Bloch waves determine the appearance of the HRTEM image. Even though a large number of diffracted waves might have been formed, only a small number of Bloch waves is usually needed to calculate an image. However, this is true only for perfect crystals [Fujimoto1978].

In the multislice methods [Cowley1957, Cowley1959], the crystal is sliced perpendicular to the wave propagation direction. The potential within each slice is projected onto a plane (Fig. 4.8) and forms this way a phase grating, described by the phase grating function $Q(x, y)$. The propagation of the electron wave Ψ_n through the n-slices results in a phase shift. The multislice approximation implies that the phase of the electron wave becomes shifted immediately on the back side of the n^{th}-slice. The further propagation of the electron wave in the vacuum between the slices can be understood in terms of Fresnel diffraction and is described by the convolution (multiplication in the Fourier space) of $\Psi_n(x, y)$ with the Fresnel propagator $P(x, y)$:

$$\Psi_{n+1}(x, y) = \Big(\Psi_n(x, y) \cdot Q_n(x, y)\Big) \otimes P(x, y), \tag{4.7}$$

where $Q_n(x, y)$ is the phase grating function. Applying this algorithm iteratively, an exit wave function $\Psi_e(x, y)$ for the whole crystal thickness can be calculated.

The image intensities are then calculated using the considerations, described in the previous subsection. An "Electron Microscopy Simulation" (EMS) programm written by Stadelmann [Stadelmann1987] was used in this work to perform multislice calculations.

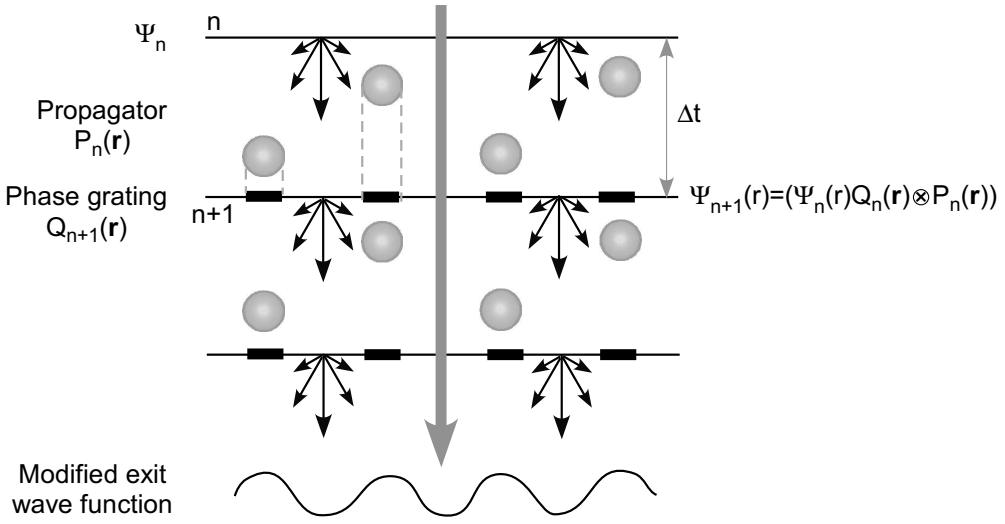

Figure 4.8: Schematic illustration of the electron wave propagation, used for the multislice calculation method.

Quantitative Image Comparison

To obtain quantitative data from the HRTEM simulations a digital comparison between the simulated and the experimental image has to be performed. In this study the IDIM (Iterative Digital Image Matching) package of Moebus *et al.* [Moebus1994, Moebus1998]) has been applied for the quantitative analysis of the HRTEM images.

Figure 4.9 summarizes the algorithm of the iterative image comparison, which is performed using the IDIM package. First, the parameters of the microscope (defocus, specimen tilt, beam tilt, 2- and 3-fold astigmatism, etc.) and of the specimen (specimen thickness, model of the atomic structure of the interface) are chosen, and an image is calculated. An experimental image is chosen and digitalized with a CCD-camera, scaled to the size of the simulated image and then compared. The comparison is performed through the calculation of a cross-correlation factor (XCF):

$$XCF(A,B) = \frac{\sum(A_{ij} - \overline{A})(B_{ij} - \overline{B})}{\sqrt{\sum(A_{ij} - \overline{A})^2 \sum(B_{ij} - \overline{B})^2}}, \tag{4.8}$$

where A_{ij} and B_{ij} are the values for the intensities of one pixel of the experimental and simulated image, respectively. This factor is sensitive to the difference in the image pattern and not to the absolute intensity difference. The values of the XCF are normalized between -1 and +1, where +1 is the best fitted case, which is not possible to achieve in reality due to

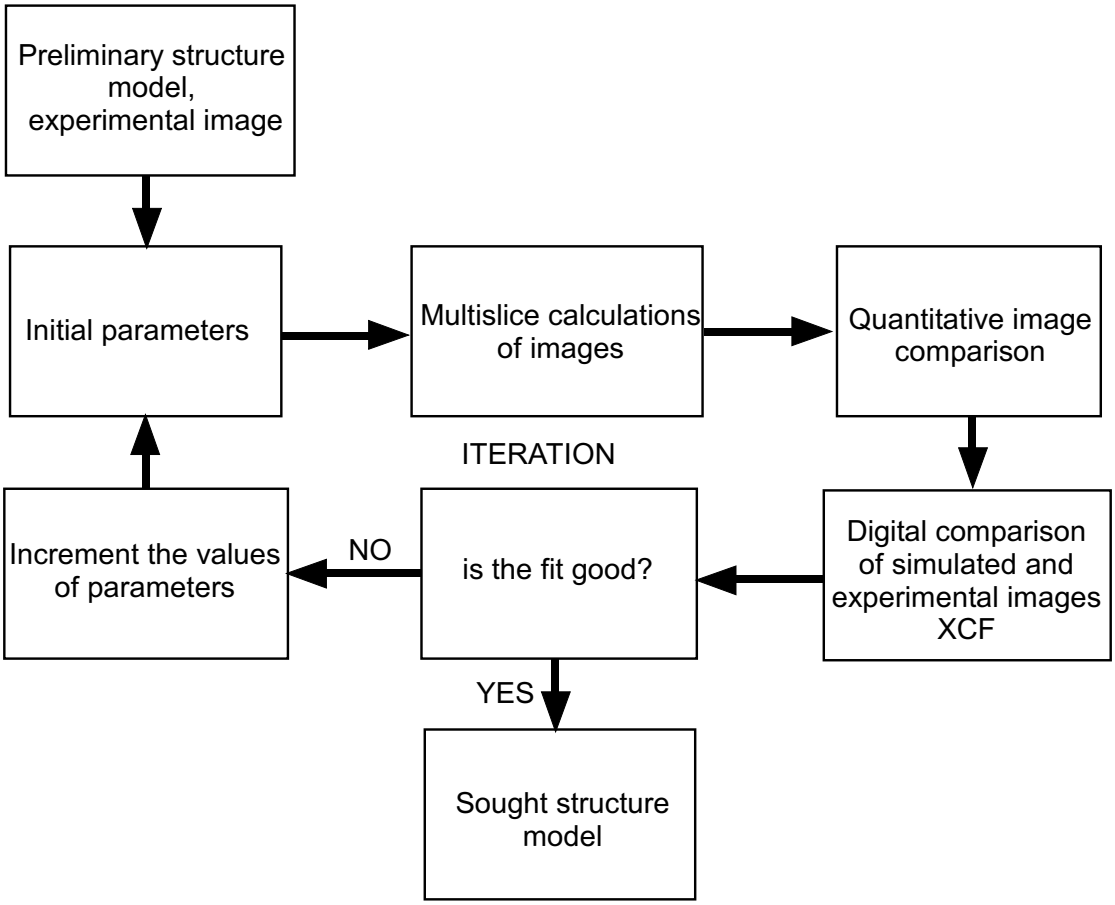

Figure 4.9: Algorithm used for the iterative digital image comparison after [Moebus1994, Moebus1998].

the presence of noise in the background of the experimental images.

If the XCF received from the comparison is not equal to an optimum value for the initial parameters, they are farther optimized and the whole process is repeated until the desired XCF is obtained.

Determination of the translation state at the interface

The determination of the translation state, e.g. the projected distance between the terminating layer of $SrTiO_3$ and the first layer of Pd at the interface, was performed using a modified method of Schweinfest *et al.* [Schweinfest1998]. Compared to the rigid blocks displacement method [Moebus1994], it allows the evaluation of larger areas of the experimental HRTEM image, which improves the accuracy of the analysis.

In order to determine the translation state at the interface a high-quality HRTEM image with minimum contrast variations in both metal and ceramic parts has to be chosen. The interfacial part has to be cut off, so that the remaining parts on the metal and ceramic sides of the image represent the rigid bulk structure of both materials (Fig. 4.10a). Furthermore, the cross-correlation map for each side of the image is calculated. For this operation, the unit cell image of one material from either experimental or simulated image can be chosen. This will be described further below in more details. The unit cell image is then moved with a step of 1 pixel in x and z directions over the entire region of the corresponding part of the HRTEM image (Fig. 4.10a). For each position of the unit cell, a value of the cross-correlation between the unit cell and the underlying image area is obtained. After finishing the procedure, a cross-correlation map is constructed (Fig. 4.10b), where bright pixels represent large values of the cross-correlation factor, i.e. a good fitting between the unit cell and the particular part of the experimental image.

In the next step, the positions of local maxima of the cross-correlation map are determined (Fig. 4.10b). Since the positions of the atoms at the image are known from the chosen unit cell, a two-dimensional lattice can be fitted within the obtained local maxima, and basis vectors of this lattice can be determined (Fig. 4.11). The origins of the basis vectors are chosen by the software in such a way, that their x positions have the same value. Further, the distance D between the origins is calculated across the interface. For the final calculation of the translation vector component $\mathbf{T}_3$, the corresponding number of basis vectors in z direction is subtracted from D at each side from the interface (Fig. 4.11, inset). The number of basis vectors, needed to reach the interface from the origins at each side of the interface is determined from the experimental image, which is shown as an inset in Figure 4.11. The distance D between the Pd and $SrTiO_3$ origins is

$$\mathrm{D} = \mathrm{O}_{Pd}(z) - \mathrm{O}_{STO}(z), \quad \text{or} \tag{4.9}$$

$$\mathrm{D} = \mathrm{n}\mathbf{a}_1 + \mathrm{m}\mathbf{b}_1 + \mathbf{T}_3, \tag{4.10}$$

where $\mathrm{O}_{Pd}(z)$ and $\mathrm{O}_{STO}(z)$ are the z coordinates of the Pd and $SrTiO_3$ origins, $\mathbf{a}_1$ and $\mathbf{b}_1$ are basis vectors of Pd and $SrTiO_3$, respectively, n and m are integers and $\mathbf{T}_3$ is the translation

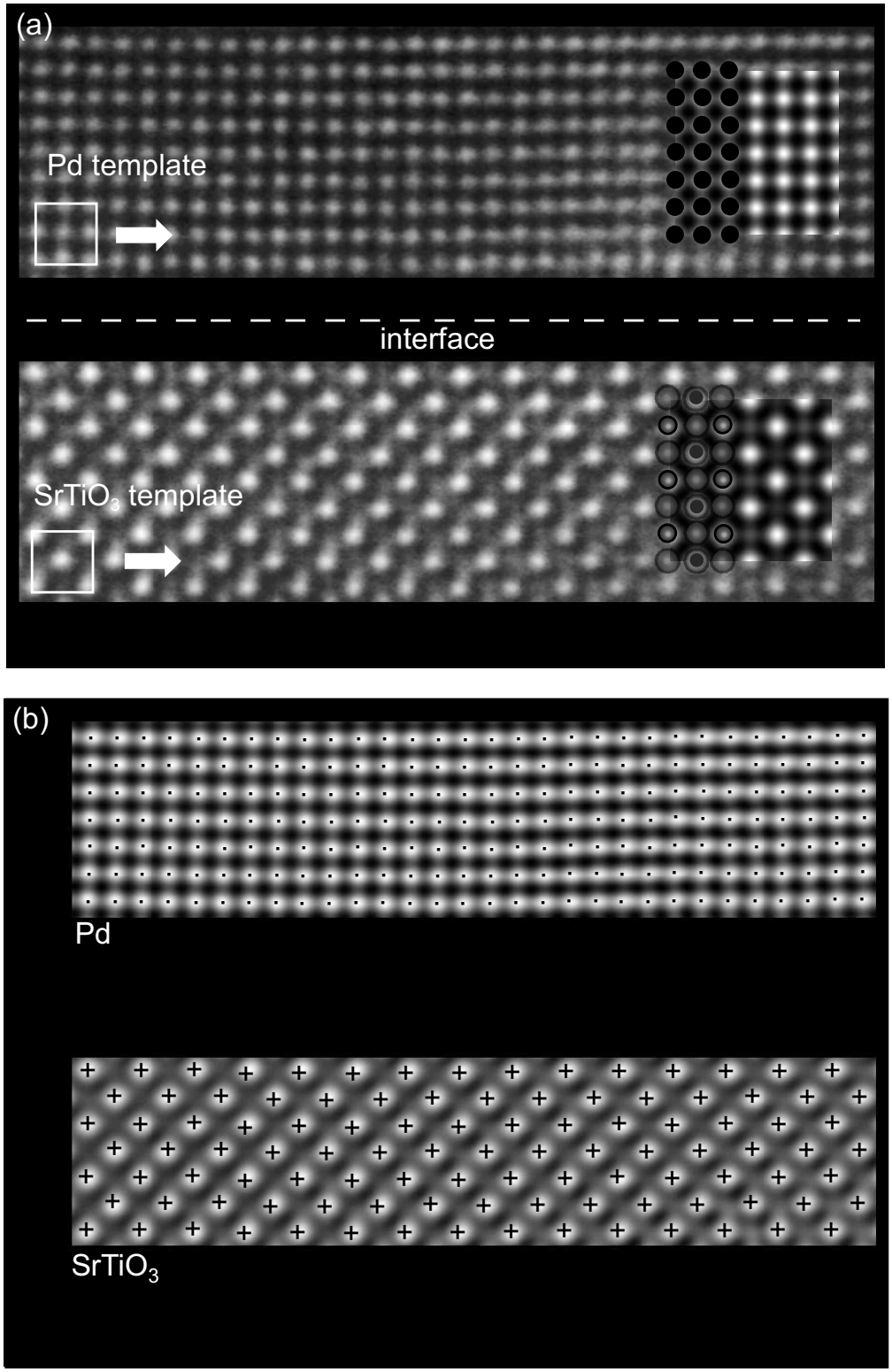

Figure 4.10: Calculation of (a) the cross-correlation map of the $Pd/SrTiO_3$ HRTEM image and (b) determination of the local maxima of the calculated map.

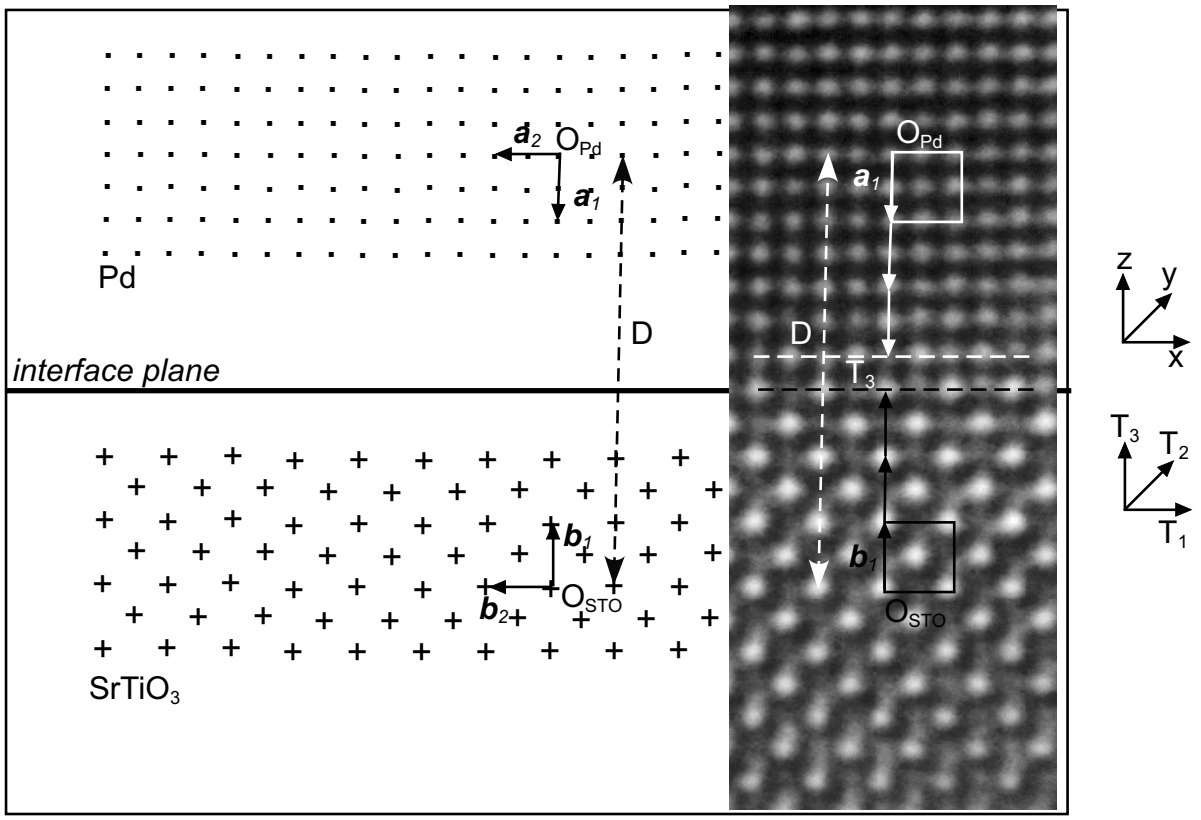

Figure 4.11: Fitted two-dimensional lattice and basis vectors for the Pd/$SrTiO_3$ image in $\langle 100 \rangle$ direction. D represents the distance between the basis vectors origins. The procedure of the determination of the $\mathbf{T}_3$ translation vector component is schematically drawn in the experimental HRTEM micrograph inset.

vector component in z direction perpendicular to the interface plane. Therefore, $\mathbf{T}_3$ can be determined as

$$\mathbf{T}_3 = \mathrm{D} - (\mathrm{n}\mathbf{a}_1 + \mathrm{m}\mathbf{b}_1). \tag{4.11}$$

In the original method of Schweinfest *et al.* [Schweinfest1998], the simulated unit cell is taken for the calculation of the cross-correlation map due to the complexity of the investigated $MgAl_2O_4$ spinel structure. In this case, the influence of different simulation parameters on the determined value of the translation vector had to be considered.

In the present work the positions of the atoms in the experimental image were determined from the simulations of bulk Pd and bulk $SrTiO_3$. It was found, that for the given imaging conditions the high intensity spots of the experimental image correspond to the positions of the atoms in both Pd and $SrTiO_3$ (Fig. 4.10a, insets). Therefore, instead of simulated images

of Pd and $SrTiO_3$ unit cells the unit cell templates cut out directly from the experimental image were used for the calculation of the cross-correlation maps (Fig. 4.10a). The influence of the simulation parameters is thus avoided. The values of the cross-correlation coefficient for each pixel movement of the unit cell template over the experimental image were written into a map. In this map, the pixel with high intensity corresponding to a value of large cross-correlation coefficient was written in the position of the middle atom in the unit cell template (see Fig. 4.10a,b). In this case, the cross-correlation map has the same intensity pattern as the experimental image. Therefore, the atoms positions coincide with the local maxima of intensity in the map. Thus, further analysis following the method of Schweinfest et al. [Schweinfest1998] can be performed.

For cutting the unit cell templates from the different parts of the experimental image, the local intensity maxima in the experimental image were determined. These maxima were further used as the origins for setting the size of the templates. Once the origin (x, z) was chosen, the size of the template was determined as $(x \pm \mathrm{k}, z \pm \mathrm{l})$, were k and l are numbers of pixels. These numbers were determined in such a way, that a region in the experimental image, corresponding to the contrast pattern of the unit cell was cut.

The cross-correlation maps were calculated for different pairs of Pd and $SrTiO_3$ unit cell templates. The length of the translation vector component $\mathbf{T}_3$ was determined for each calculation iteration following the algorithm of Schweinfest *et al.* [Schweinfest1998], described above. For the determination of the final value of $\mathbf{T}_3$, the obtained $\mathbf{T}_3$ values were averaged. This allowed to encounter inhomogeneities of the HRTEM image, which are due to noise, structure defects, etc.

4.2.4 High-angle Annular Dark Field Imaging (Z-contrast)

High angle annular dark field imaging (HAADF) is another high-resolution technique, which allows to determine the atomic structure of interfaces [Pennycook1991, Browning1993]. A TEM equipped with a scanning unit and a HAADF detector is required for this technique. On Figure 4.12 a schematic drawing of such an instrument is shown. The incident probe (typically $0.15 - 0.2$ nm for medium voltage STEMs with field emission guns) is focused on the specimen. The electrons are scattered at different angles while passing through the

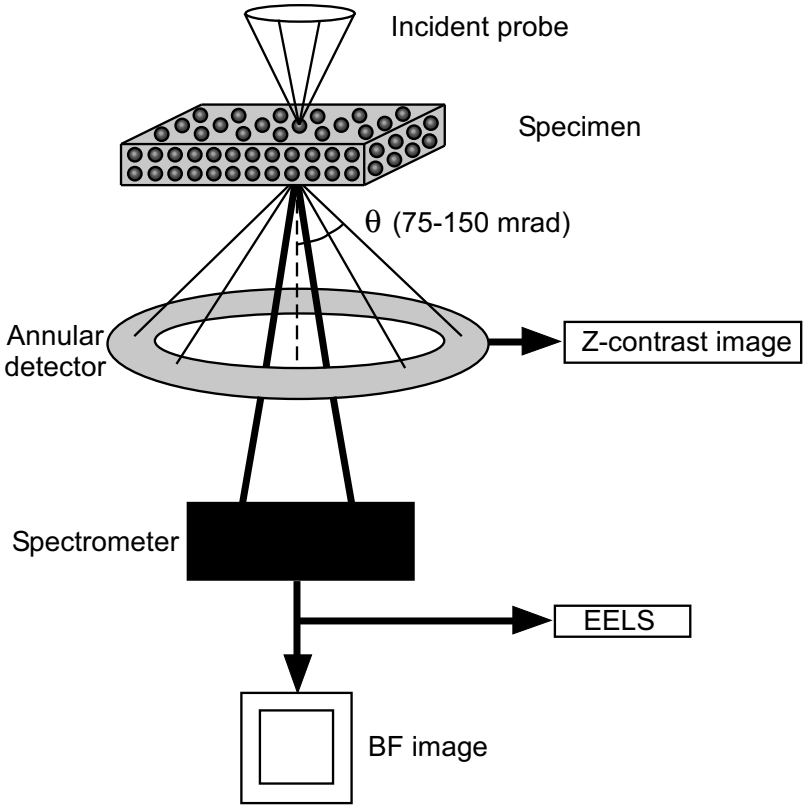

Figure 4.12: Schematic drawing of the STEM-HAADF imaging system.

specimen. The HAADF detector collects mainly the electrons that are scattered incoherently at relatively high angles ($75 - 150$ mrad). A small background is caused by thermal diffused scattering.

HAADF imaging can be described by Rutherford scattering, i.e. as a scattering from the unscreened nucleus:

$$\frac{\mathrm{d}\sigma}{\mathrm{d}\Omega} = \frac{Z^2 e^4}{16 E^2 sin^4 \Theta} \ , \tag{4.12}$$

where σ is the scattering cross-section, Z the atomic number, e the elementary charge, Θ the scattering angle and E the energy of the scattered electron. From 4.12 it is seen that $\sigma \sim Z^2$; in other words, the intensity in the image is proportional to the square of the atomic number of the scattering atom (hence the other name of the technique: Z-contrast). The image is formed by scanning the electron beam across the specimen while simultaneously the HAADF signal is registered at each point.

Part II

Specimen Preparation and Experimental Details

Chapter 5

Specimen Preparation and Experimental Details

In this chapter, the techniques and the experimental set-up used for growing thin metal films on the $SrTiO_3$ substrates are described. The molecular beam epitaxy (MBE) technique, used for the preparation of metal/ceramic interfaces in this work, and the experimental details of the film growth are described in Section 5.1. For the TEM investigations cross sectional and plan view specimens were prepared. The preparation technique and problems are described in Section 5.2.

5.1 Molecular Beam Epitaxy (MBE)

Thin metal films were grown[1] on the $SrTiO_3$ substrates by MBE technique. MBE is based on the process of thermal evaporation of metals and their further deposition onto the ceramic substrate. The evaporated metal atoms condensate on the substrate surface and are adsorbed on nucleation sites. The diffusion of the adsorbed atoms depends on the substrate temperature during growth. The evaporated atoms interact only with the substrate surface and with the chamber walls.

The typical pressure in the chamber during the MBE growth was $5{\cdot}10^{-9}$Pa. Richter

[1] Mo/$SrTiO_3$ specimens used in this work were produced (MBE-grown) by Q. Fu and T. Wagner. Pd/$SrTiO_3$ specimens were partially grown by G. Richter [Richter2000].

[Richter2000] found that the substrate surface remains free of contaminations for about 48 hours under this vacuum conditions after a cleaning procedure has been performed. The evaporation of the metals is done by using either effusion cells or electron beam evaporators. For the effusion cells, an evaporation temperature up to 1500°C and more stable deposition rates are achievable in comparison to the electron beam evaporators [Richter2000]. The *in situ* analysis of the growth behavior of Mo films was performed though RHEED, AES, XPS, STM and AFM facilities that are attached to the MBE chamber.

Experimental Details

In the present work, commercially prepared (001)-oriented single crystals of $SrTiO_3$ (Crystal GmbH, Berlin, Germany) with dimensions of 10mm×10mm×0.5mm were used as substrates. The surface miscut of the crystals was below 0.1°. The substrates were prepared as described by Kawasaki *et al.* [Kawasaki1994] and Polli *et al.* [Polli1999]. These preparation routines enable obtaining flat and predominantly TiO_2 terminated $SrTiO_3$ surfaces.

Pd films were grown on the (001)-plane of the $SrTiO_3$ surfaces with nominal thicknesses of 50 nm at a substrate temperature of 650°C. The substrate temperature and the deposition rate were chosen in such a way that the film and the substrate form a cube-on-cube epitaxial orientation relationship [Richter2000, Wagner2001].

Mo films were also grown with a nominal thickness of 50 nm. Some specimens were capped with 10nm thin Pd layer, deposited at room temperature on top of Mo to prevent the oxidation of Mo. Due to the large difference of lattice constants between Mo and $SrTiO_3$ a number of orientation relationships can occur [Wagner2001]. A substrate temperature of 600°C and a deposition rate of 0.01 nm/sec for the first 5 nm and 0.15 nm/sec for the remaining 45 nm resulted in reproducible Mo/$SrTiO_3$ specimens.

AES was routinely used to check the cleanliness of the substrate. Metal films were only deposited if less than 0.01 ML of impurities were found at the substrate surface. The growth and annealing processes were monitored by *in situ* RHEED. The RHEED patterns were recorded at a primary electron energy of 30 keV with a CCD camera.

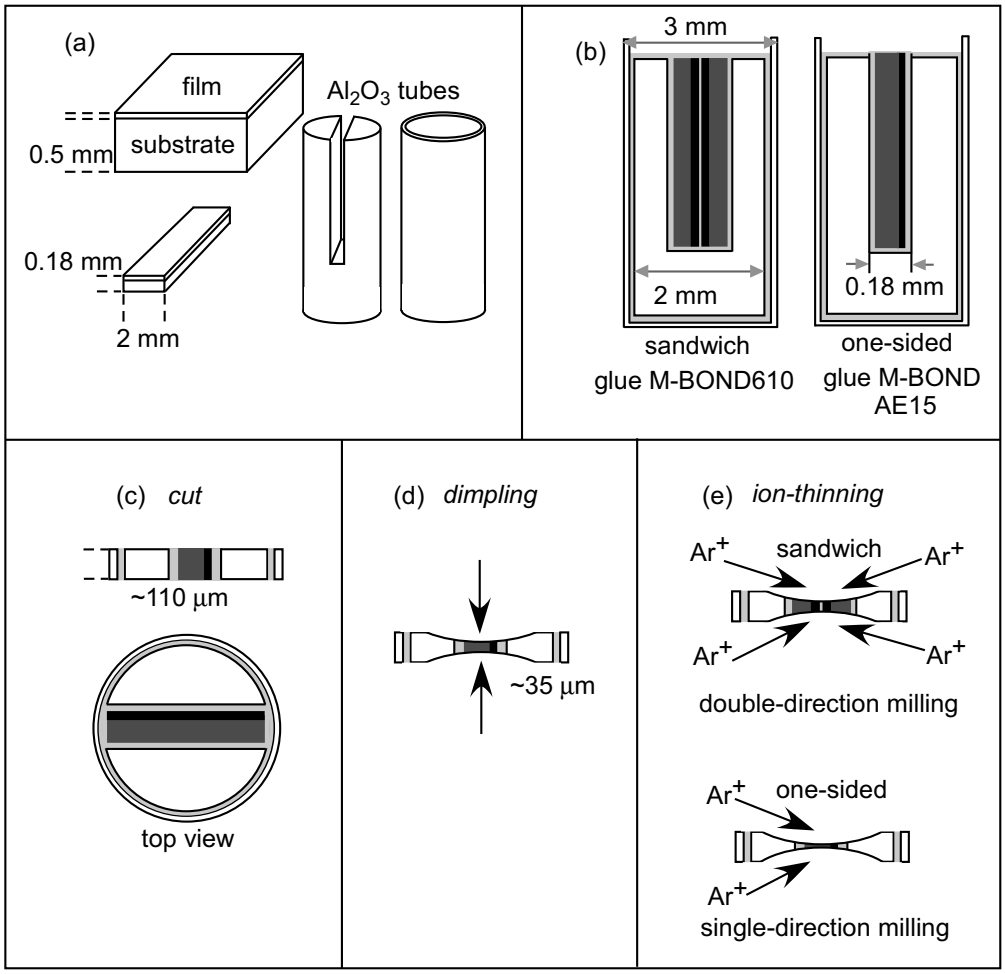

Figure 5.1: Schematic drawing of the cross-sectional TEM specimen preparation: (a) cutting and grinding the raw material, preparing to put it into the alumina holders; (b) gluing of the specimen into the alumina tubes; (c) cutting the tube into 500μm thick disks, which are then polished down to 100μm; (d) double-sided dimpling down to 35μm; (e) ion-thinning until the specimen becomes electron transparent (the whole appears in the middle).

5.2 TEM Specimen Preparation

TEM investigations require specimens which are mechanically stable and are electron transparent. Typical specimen thicknesses in the regions of interest are lying in the range of $5-50$ nm.

A TEM specimen of a high quality should fulfill specific conditions, such as small thickness and undisturbed crystalline structure. Several techniques are available in order to ob-

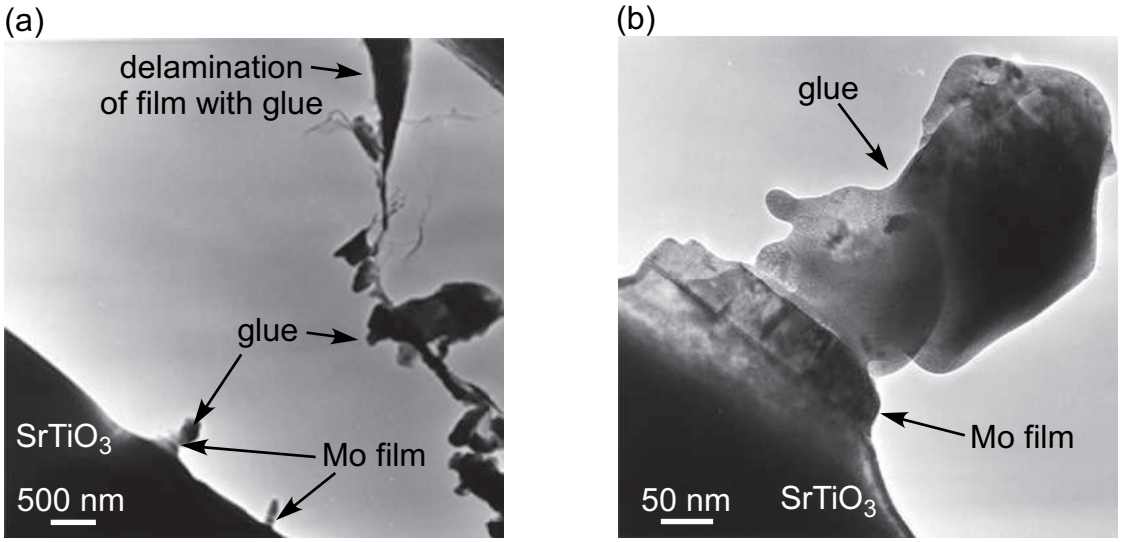

Figure 5.2: BF images of the sandwiched Mo/$SrTiO_3$ specimens, on which double-sided ion-thinning in the Gatan DUOMILL600 was performed. The specimen shows a delamination of the Mo layer (a), as well as extreme glue contamination (b).

tain such specimens (mechanical grinding, chemical etching, electrolytical thinning, ion-beam cutting techniques, ion-thinning techniques, etc.). The preparation of electron transparent metal/ceramic interfaces is a challenge for the TEM specimen preparation since these systems possess different mechanical and chemical properties. Ceramics are non-conductive and brittle while metals are conductive and easily deform plastically. Thus, such interfaces need special preparation techniques and approaches.

For the cross-section specimens, preparation techniques based on methods developed by Strecker et al. [Strecker1993] were employed. MBE prepared samples were cut into slices with a width of 2 mm along $\langle 100 \rangle$ or $\langle 110 \rangle$ directions. These slices were ground from the substrate side to 180 μm and glued into a polycrystalline alumina tube as it is drawn schematically in Figure 5.1. The inner tube has a slit with a width of 180 μm and a length (tube diameter) of 2 mm. After the specimen is inserted into the inner slit, an outer tube is placed over it. For the "sandwich"type of specimens two pieces of material were first glued together with highly dispersed epoxy-glue M-BOND610 and afterwards glued into the alumina tube with the M-BOND AE15 epoxy-glue. The latter has a higher final stiffness compared to M-BOND610. After the hardening of the glue, the tube is cut into 500 μm thick discs with a wire-saw parallel to the $\langle 100 \rangle$ substrate direction. The discs are then ground mechanically

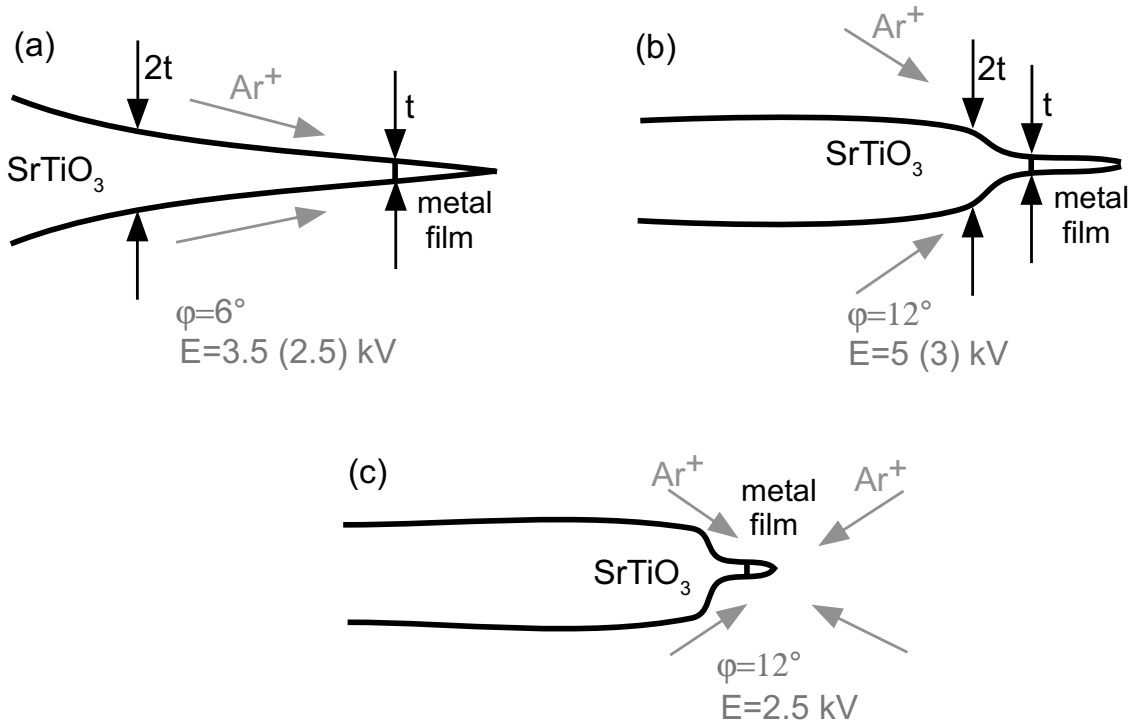

Figure 5.3: Schematic drawing of the ion-thinning process using: (a) Gatan PIPS at 6°, single direction thinning (after [Benthem2002]); (b) Gatan DUOMILL at 12°, single direction thinning (after [Benthem2002]); (c) Gatan DUOMILL at 12° with the short double-direction thinning at the end.

to approximately 100 μm (Fig. 5.1c) and dimpled from both sides so that the middle part of the disk achieves a thickness of approximately 35 μm (Fig. 5.1d). Finally, an ion-milling procedure with high energy Ar^+-ions [Strecker1993] is applied until perforation. The areas adjacent to the specimen hole were used for the TEM observations.

Van Benthem [Benthem2002] has reported difficulties that occur with the Pd/$SrTiO_3$ sandwiched specimens. He observed that the Pd film is delaminated in the sandwiched specimens, which occurred due to the high shear stresses present during the sandwich formation. The same problem occured for Mo/$SrTiO_3$ sandwiched specimens (Fig. 5.2a,b). The Mo film is delaminated, damaged or covered with contaminations, generated most likely during double-direction ion-milling due to the presence of the glue layer (Fig. 5.1e). Therefore, further specimens were prepared as one-sided and ion-milled only from one direction, from Mo to the $SrTiO_3$. Such an approach prevents severe damage or contamination of the interface and the metal film.

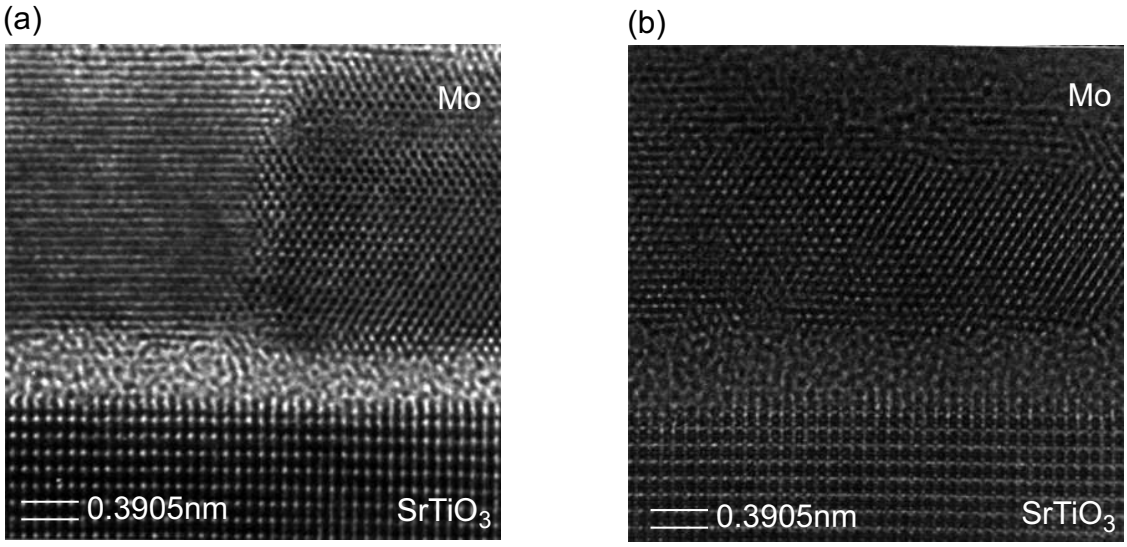

Figure 5.4: HRTEM images of the Mo/$SrTiO_3$ one-sided specimens, ion-milled in single direction (from Mo to $SrTiO_3$) in the Gatan PIPS. (a) shows a grain boundary in Mo and an interface between Mo and $SrTiO_3$, which is amorphized; (b) amorphous areas are also observed in the Mo.

The ion-thinning was performed with two different mashines: a Gatan PIPS and a Gatan DUOMILL600. The Gatan PIPS has a smaller incidence angle (down to 6°) and a beam that is more focused compared to the DUOMILL600. The specimens prepared with the PIPS reveal larger thin areas (Fig. 5.3a) but strong bending [Benthem2002] and material damage (amorphization etc.) might take place. The Mo/$SrTiO_3$ was found to be extremely sensitive to such an intensive ion-bombardment (Fig. 5.4a,b). The Gatan DUOMILL600 with its incidence angle of 12° and rather defocused beam was found to be more suitable for the preparation of the Mo/$SrTiO_3$ specimens for HRTEM investigations. It produces rather small thin areas in comparison to the PIPS (Fig. 5.3a,b), but this improves the mechanical stability of the specimen, so that bending effects are reasonably small.

Since the thinning rates of the $SrTiO_3$ and the metal differ due to the difference in mechanical and chemical properties, it is possible that a grooving at the interface during the ion-milling occurs. A short (2-5 min.) low-energy (2.5kV) double-direction ion-milling with the DUOMILL600 (Fig. 5.3c) in the last stage of the ion-thinning procedure leads to even smaller thin area. Nevertheless, the smoothing of the thickness gradient at the interface and decreasing of bending effects are advantageous in this case.

Part III

Applications: $Mo/SrTiO_3$ and $Pd/SrTiO_3$ Systems

Chapter 6

$Mo/SrTiO_3$

In this chapter, experimental results concerning the microstructure of the Mo films and atomic structure of the $Mo/SrTiO_3$ interface will be described (Section 6.1). In Section 6.2, the experimental data on the film structure are compared to the results of the geometrical model ("near coincidence site lattice", e.g. NCSL model). On this basis, the experimental results are discussed in Section 6.3.

6.1 Experimental

In the following sections the experimental results obtained by XRD, conventional TEM, SAD and HRTEM are presented. The first section gives a detailed analysis of the film structure and its orientation relationships with the $SrTiO_3$ (100) substrate, whereas the grain boundaries studies are described in the third section. HRTEM imaging experiments performed on the $Mo/SrTiO_3$ interface are presented in the second section.

6.1.1 Film Structure and Orientation Relationship with $SrTiO_3$

Film Growth

In situ RHEED measurements[1] were performed in the MBE chamber prior to and during the deposition of Mo on the $SrTiO_3$ (100) surface. Figure 6.1a shows RHEED patterns of a clean $SrTiO_3$ substrate along both the [100] and [110] azimuths [Fu2003]. The location of the

[1] *in situ* RHEED measurements were performed in collaboration with Q. Fu and T. Wagner [Fu2003].

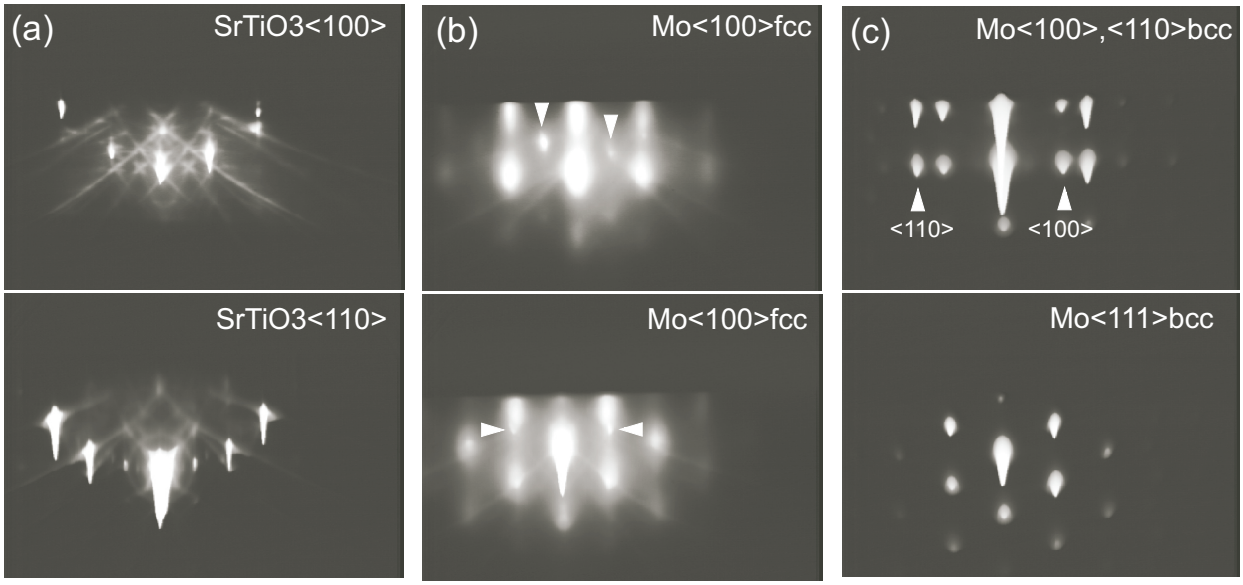

Figure 6.1: RHEED patterns of (a) clean $SrTiO_3$ surface along the [100] and [110] azimuths, (b) fcc-like 0.6 nm thick Mo film, annealed at 640°C with the electron beam oriented along the [100] and [110] azimuths of $SrTiO_3$ ($SrTiO_3$ reflections are denoted by arrow heads) and (c) bcc Mo pattern along [100] $SrTiO_3$ azimuth and $\langle 111 \rangle$Mo azimuth ($\langle 110 \rangle SrTiO_3 \pm 10^\circ$ rotated), obtained from the Mo film with a thickness of larger than 2 nm [Fu2003] .

RHEED streaks on the Laue circles indicates that the surface of the $SrTiO_3$ is smooth. Figure 6.1b shows the RHEED pattern of a 0.6 nm thick Mo film grown at room temperature and annealed at 500°C, taken along the $\langle 100 \rangle$ azimuth of $SrTiO_3$. The weak intensitites, marked by arrow heads in the Figure 6.1b, originate from the substrate. No change in the pattern was observed during the annealing of the film at temperatures ranging between 500°C and 900°C. The quantitative analysis of the pattern revealed that a lattice parameter differs from that of a regular bcc Mo structure. Instead, an fcc-like Mo structure with the lattice parameter of $a_{fcc-like\ Mo} = (4.05 \pm 0.10)$ Å was detected. XPS and AES measurements showed that the impurity concentration was below the detection limit (0.1 at%) and that the Mo stayed in the metallic phase [Fu2003]. For the fcc-like Mo metallic phase, the following OR was determined:

$(100)_{fcc-like\ Mo} \| (100)_{STO}$;

$\langle 001 \rangle_{fcc-like\ Mo} \| \langle 001 \rangle_{STO}$.

The RHEED patterns shown in Fig. 6.1c were acquired as the thickness above 2 nm was

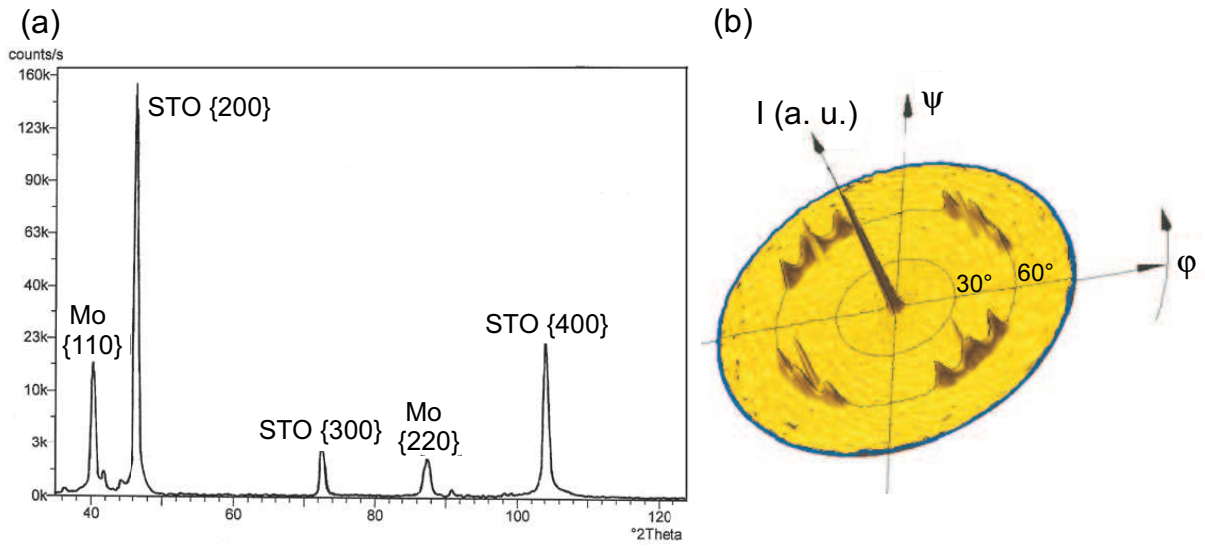

Figure 6.2: X-ray diffraction measurements: (a) $\Theta - 2\Theta$-scan and (b) $(110)_{Mo}$ pole figure.

reached. For these thicker films, the observed Mo lattice constant corresponds to bcc Mo: $a_{bcc\,Mo} = 3.15$ Å. Two sets of reflections in the upper pattern in Fig. 6.1c originate from two geometrically equivalent epitaxial variants of bcc Mo domains:

$(110)_{bcc\,Mo} \| (100)_{STO}$;

$\langle 001 \rangle_{bcc\,Mo} \| \langle 001 \rangle_{STO}$ (OR Ia);

$\langle 011 \rangle_{bcc\,Mo} \| \langle 001 \rangle_{STO}$ (OR Ib).

The lower pattern in Fig. 6.1c, showing $\langle 111 \rangle$Mo with 3-fold symmetry, was observed along the $SrTiO_3\langle 100 \rangle \pm 10°$ and also along $SrTiO_3\langle 110 \rangle \pm 20°$ azimuths. This pattern indicated that an additional epitaxial OR between Mo and $SrTiO_3$ [Fu2003] exists:

$(110)_{bcc\,Mo} \| (100)_{STO}$;

$\langle 111 \rangle_{bcc\,Mo} \| \langle 011 \rangle_{STO}$ (OR II).

Mo films with nominal thicknesses of 50 nm grown at 600°C revealed the same epitaxial behavior and the presence of OR Ia, Ib and II. These specimens were investigated further in the present work using different TEM techniques.

X-Ray Diffraction

Prior to TEM investigations, XRD[2] measurements were performed in order to determine

[2]XRD measurements were performed by Dipl.-Ing. G. Maier at the ZWE Röntgenbeugung.

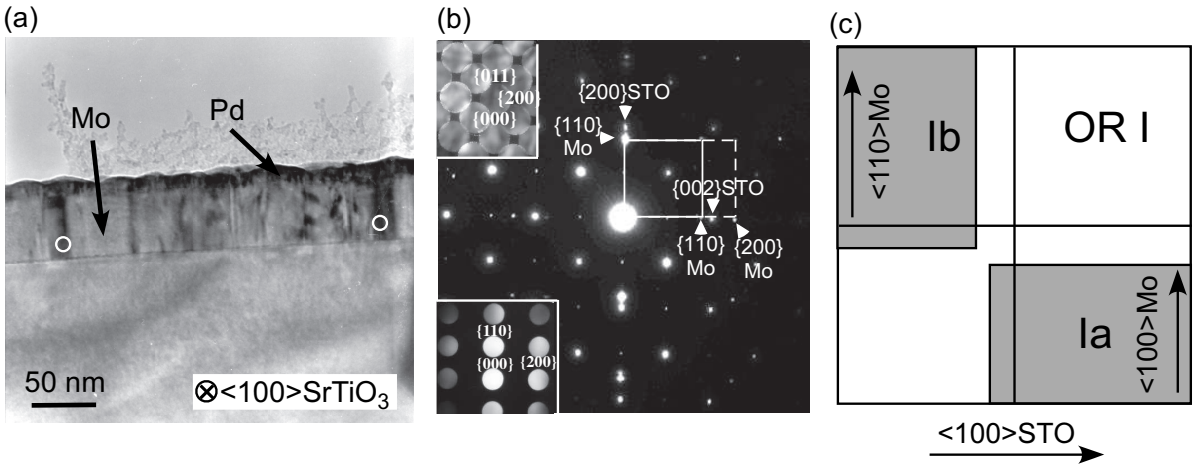

Figure 6.3: CTEM of the Mo/SrTiO$_3$ cross-sectional specimen in $\langle 100 \rangle_{STO}$ zone axis: (a) bright-field image and (b) SAD and nano-diffraction patterns. The latter are taken from the areas marked with white circles in the BF image. The diffraction pattern reveal the presence of (c) the $(100)_{Mo}$ OR I geometrically equivalent domain variants on the $(100)_{STO}$ surface. Top-view schematic drawing of these domains is shown.

the structure and epitaxy of the as-grown Mo films. $\Theta - 2\Theta$-scans revealed that the $(100)_{STO}$ plane is parallel to the $(110)_{Mo}$ plane, since only reflections from $(100)_{STO}$ and $(110)_{Mo}$ families are detected (Fig. 6.2a). In addition to the $\Theta - 2\Theta$ measurements, the Mo (110) pole figures were taken to investigate the in-plane structure of the films. The pole figure (Fig. 6.2b) showed four triple peaks, located at $\varphi = 60°$. These peaks are reflections from (110) planes in Mo, originating from at least six possible domains. The domains have common planes parallel to the substrate, $(110)_{Mo} \| (100)_{STO}$. However, their in-plane orientations differ. The four narrow peaks present in Fig. 6.2b are caused by the substrate. Comparing the width of the substrate peaks with those of the Mo peaks, it can be seen that the latter are larger and form bands instead of sharp maxima. This indicates a slight rotational distribution of domain orientations ($\pm 5°$) from the perfect orientations to the substrate, which was also observed in TEM diffraction experiments described below.

Conventional TEM

TEM imaging and diffraction experiments were performed at the 50 nm thick Mo films grown at a substrate temperature of 600°C. Figure 6.3a shows a bright field image of a cross-

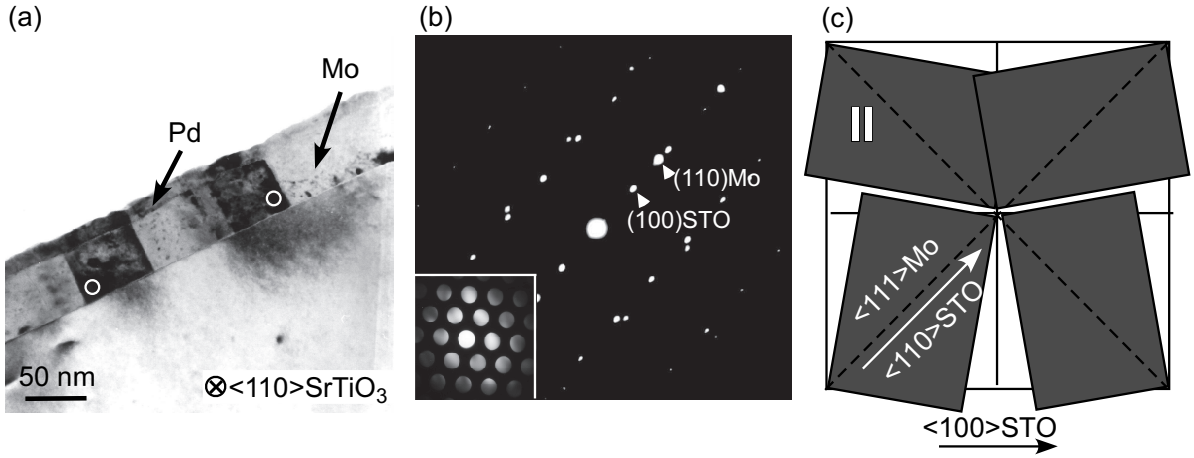

Figure 6.4: CTEM of the $Mo/SrTiO_3$ cross-sectional specimen in $\langle 110 \rangle_{STO}$ zone axis: (a) bright-field image, (b) SAD and nano-diffraction patterns, showing $(110)_{Mo}$ reflections arising from OR II type domains. The areas where the nano-diffraction patterns were taken are marked with white circles. Top-view schematic drawing of the OR II domain variants on the $(100)_{STO}$ surface is presented in (c).

sectional $Mo/SrTiO_3$ specimen, where a continuous molybdenum film, covered for protection by a 10 nm thick Pd layer, is visible. Dark and bright contrast regions in the Mo correspond to the different grains that are oriented differently with respect to the substrate. The orientation relationships were determined by selected area diffraction and nano-diffraction. The SAD pattern shown in Figure 6.3b was obtained from a circular area with a diameter of about 2μm selected by the SAD aperture. Detailed analysis of the pattern indicated the presence of one epitaxial orientation relationship with two geometrically equivalent variants (Figure 6.3c):

$\{110\}_{Mo} \| \{100\}_{STO}$;

$\langle 100 \rangle_{Mo} \| \langle 100 \rangle_{STO}$ (**OR Ia**);

$\langle 110 \rangle_{Mo} \| \langle 100 \rangle_{STO}$ (**OR Ib**).

The nano-diffraction patterns (insets in Fig. 6.3b) were taken from small circular areas with a diameter of about 15 nm. For these patterns the smallest condenser aperture was chosen and the incident beam was focused on the specimen. The areas were chosen from the edge-on oriented domains that appeared dark in the Mo film in the BF image (Fig. 6.3a). The areas are marked with white circles in the figure. The observed pattern showed also the presence of OR Ia and Ib, which is in agreement with the *in-situ* RHEED observations

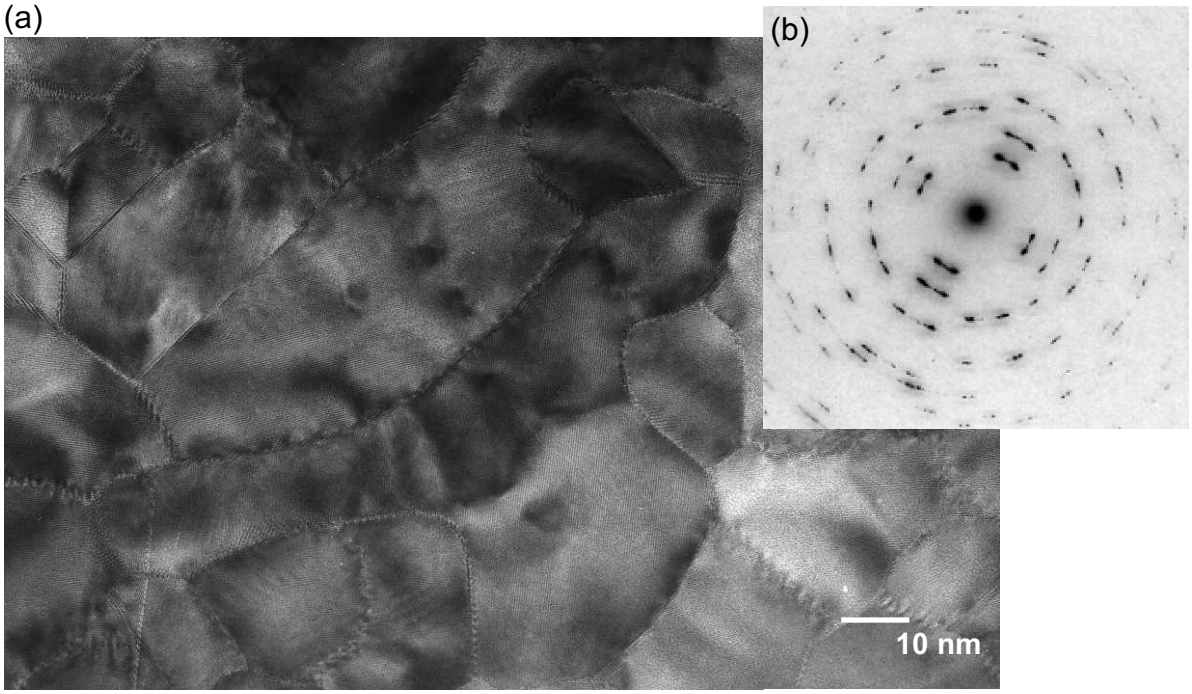

Figure 6.5: CTEM micrograph of the plan-view specimen: (a) bright-field image of the Mo film without $SrTiO_3$ and (b) the corresponding SAD pattern.

[Fu2003, Wagner2001]. A plan-view drawing of the relationship of the OR I domains relative to the substrate is shown in Fig. 6.3c.

The same methods were applied to investigate cross-sectional TEM specimen in the $\langle 110 \rangle_{STO}$ direction (Fig. 6.4a). In this case, the domains are larger and more clearly visible in the BF image than the domains of OR I. A detailed analysis of the SAD pattern revealed the presence of a second non-equivalent orientation relationship consisting of four geometrically equivalent variants (Fig. 6.4b):

$\{110\}_{Mo} \| \{100\}_{STO}$;

$\langle 111 \rangle_{Mo} \| \langle 110 \rangle_{STO}$ (**OR II**).

Nano-diffraction pattern collected from the edge-on aligned darker regions (inset in Figure 6.4b, the areas are marked with white circles) also showed the 3-fold symmetry of $\langle 111 \rangle$ Mo. Figure 6.4c shows a schematic drawing of the 4 possible nonequivalent positions of OR II Mo on top of $SrTiO_3$. This OR was also observed by in-situ RHEED during the film growth.

To obtain information about the size and shape of the grains as well as to observe the grain boundary structure, a plan-view specimen where was investigated by TEM. The $SrTiO_3$ was

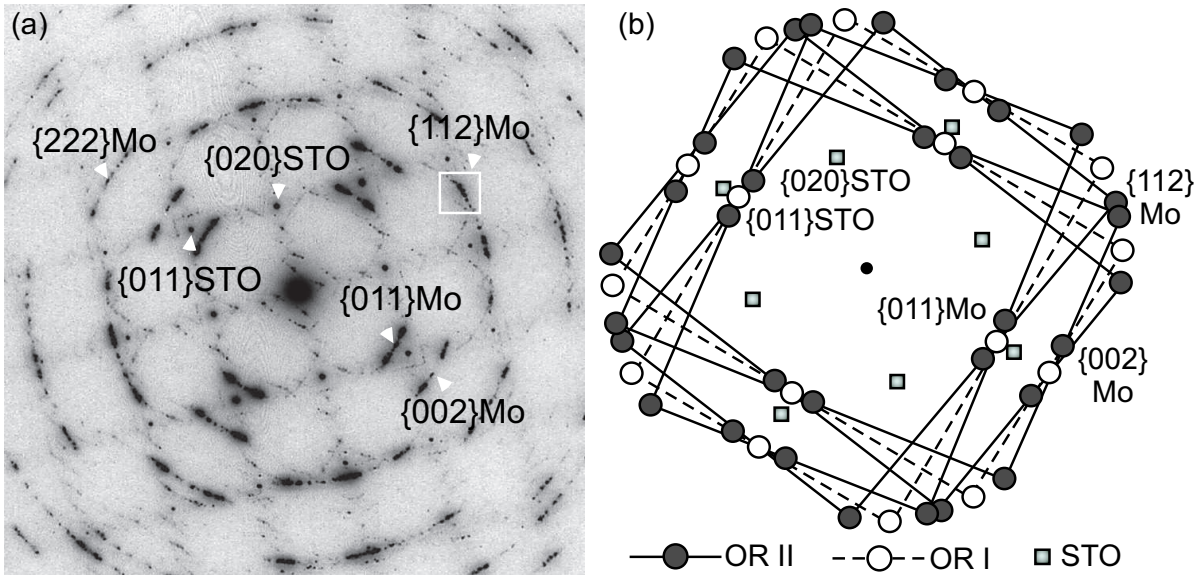

Figure 6.6: SAD studies of a plan-view Mo/$SrTiO_3$ specimen with $SrTiO_3$ present underneath the film: (a) SAD pattern, showing both Mo and $SrTiO_3$ reflections and (b) corresponding schematic drawing of SAD reflections, showing the presence of all domain variants.

completely removed by the ion-thinning procedure. Figure 6.5a shows a CTEM micrograph of such a specimen. The image shows that the domains differ in size from $\sim$ 10 to $\sim$ 50 nm. Some of the grain boundaries between the domains are faceted. The corresponding SAD pattern is shown in the Figure 6.5b.

To determine the distribution of the domains relative to the substrate, the area where both materials, Mo film and $SrTiO_3$ substrate, are present was chosen. The SAD pattern taken from this area (Fig. 6.6a) showed the presence of both OR I(a,b) and OR II. This pattern is schematically drawn in Figure 6.6b. The reflections corresponding to OR II possess high intensities, while the reflections corresponding to OR I have weak intensities (Fig. 6.6a and b). It should be also emphasized that the Mo reflections are not single-point reflections. Instead, there is a distribution of reflections, coming from the same nominal type of domains, over a range of deviation angles of $\pm 5°$. One of such "bands of reflections"is marked in the Figure 6.6a by a white square.

The domain distribution was investigated more precisely by performing nano-diffraction on single grains. In the experiment, the specimen was tilted in $\langle 110 \rangle_{Mo}$ zone axis, and the

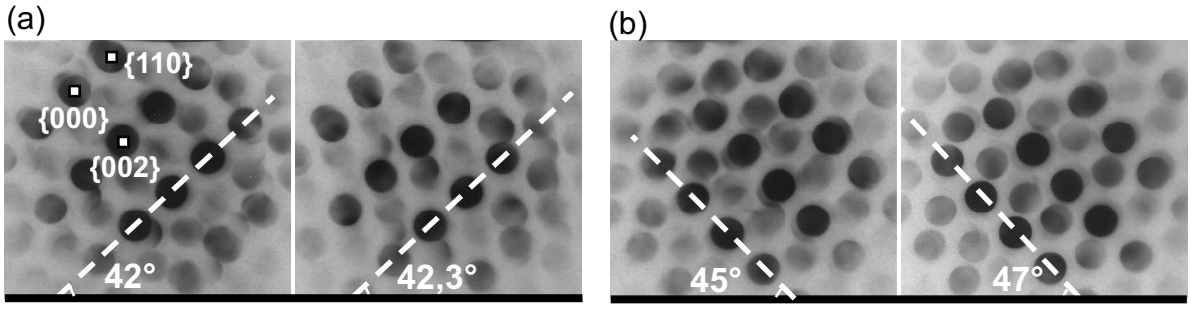

Figure 6.7: Nano-diffraction patterns, taken from the different grains in the plain-view specimen without changing the specimen position. The patterns show angular differences of (a) 0.3° and (b) 2° between the grains belonging to the same OR type.

nano-diffraction patterns were taken from the different grain ($\sim 15-20$ nm area) without further tilting of the sample. The patterns taken from the area that included various grains indicate that the grains belong to the same nominal OR type (Fig. 6.7a,b) but demonstrate an angular difference of 0.3° (Fig. 6.7a) and 2° (Fig. 6.7b) between the grains. This is in agreement with the results from the X-ray pole figure, where these deviations from the perfect OR appear as peak broadening (Figure 6.2b).

6.1.2 Atomic Structure of the Mo/SrTiO$_3$ Interfaces

The interfaces between the Mo domains and the $SrTiO_3$ substrate were investigated in detail by HRTEM. Micrographs taken from the cross-sectional specimens showed that a massive reaction layer is not formed at the interface. Figure 6.8a shows a HRTEM micrograph of the Mo/$SrTiO_3$ interface, viewed in $\langle 110\rangle$ direction of $SrTiO_3$. The upper part of the image corresponds to a Mo domain that possess the OR II. The lattice mismatch between Mo and $SrTiO_3$ in this direction is $f_{OR\,II} = +1\%$. Misfit dislocations could not be identified at the interface.

In the cross-sectional specimen, aligned in the $\langle 100\rangle_{STO}$ zone axis, both $\langle 100\rangle_{OR\,Ia}$ and $\langle 110\rangle_{OR\,Ib}$ Mo domains were observed (Fig. 6.8b,c). The lattice misfits for these types of domains are $f_{OR\,Ia} = -12.34\%$ and $f_{OR\,Ib} = +23.97\%$, respectively. A non-uniform bright contrast, appearing directly at the interface within the last $SrTiO_3$ layer and the first Mo layer is visible in the micrograph. This feature might be caused either by a local chemical

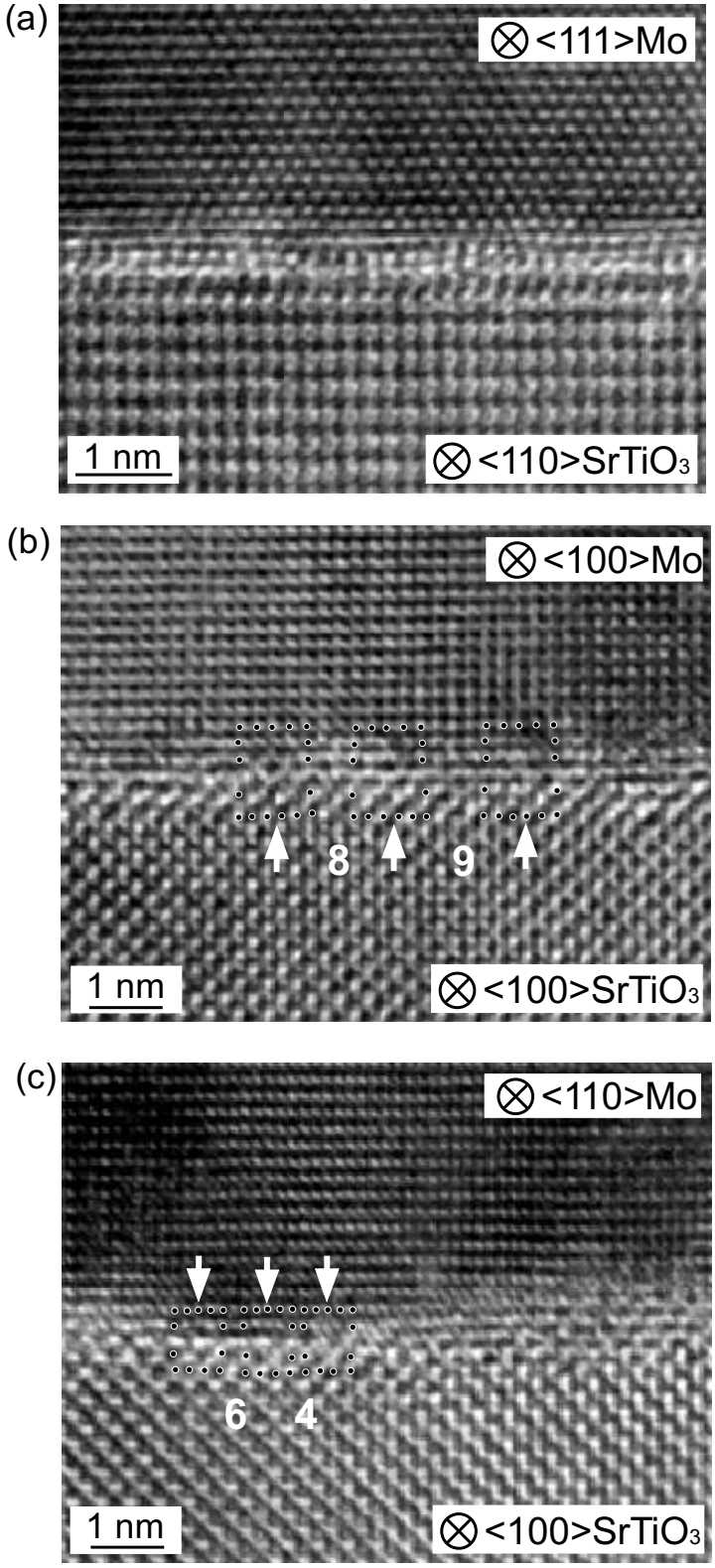

Figure 6.8: HRTEM micrographs of the interface between $SrTiO_3$ and Mo domains, possessing: (a) OR II $\langle 111\rangle_{Mo}\|\langle 110\rangle_{STO}$, (b) OR Ia $\langle 100\rangle_{Mo}\|\langle 100\rangle_{STO}$, and (c) OR Ib $\langle 110\rangle_{Mo}\|\langle 100\rangle_{STO}$. The positions of misfit dislocations are indicated by arrows.

reaction between Mo and $SrTiO_3$ or by ion-beam induced damage, which might be produced during TEM specimen preparation. The diffuse contrast at the right part of Figure 6.8c is most likely caused by an overlap of the Mo and $SrTiO_3$ lattices in the viewing direction due to the presence of a substrate step in the $\langle 110 \rangle$ direction of $SrTiO_3$.

The HRTEM micrographs shown in the Figures 6.8b and c reveal the presence of misfit dislocations. The distance between the misfit dislocations corresponds to the lattice mismatch: an extra Mo plain is inserted every 4-6 planes for the $\langle 100 \rangle$ direction and every 7-9 planes for the $\langle 110 \rangle$ direction. The interface is semi-coherent [Sutton1994] with coherent regions separated by misfit dislocations. Most of the dislocations initiate directly at the interface.

6.1.3 Grain Boundaries in Mo

HRTEM observations of plan view specimens revealed the presence of special grain boundaries in the Mo film. Figure 6.9a presents a HRTEM micrograph, where two triple junctions are formed by 5 different grain boundaries (GBs) between 4 different grains. Such boundaries were commonly observed in the investigated plan-view specimens: symmetrical tilt $\Sigma 3$ (112), $\Sigma 17$b (334), $\Sigma 83$a (119), 90° GB and asymmetrical GB. The values of Σ were determined from the misorientation angles, which deviated by a maximum of $\pm 1.5°$ from the ideal value.

Figure 6.9b shows a micrograph of a $\Sigma 3$ twin lamella, which was observed frequently in large grains of the Mo film. Such lamella had typically a length of 15-20 nm and a width of 5-10 nm. In most cases $\Sigma 3$ GBs were not observed edge-on oriented.

Low angle grain boundaries with angles $< 15°$ were also observed in the specimens. One of them, a 7.5° boundary is shown in Figure 6.9d. It is formed by a row of dislocations, which appear every 7(8) planes.

Most GBs could not be observed in edge-on orientation, since the GB planes were not exactly parallel to the $\langle 110 \rangle_{Mo}$ viewing direction of the plan-view specimen. In Figure 6.10 perfect straight GB (6.10a) and inclined and curved GB (6.10b) planes are sketched, with the arrows indicating the viewing direction for the plan-view specimen. For the case illustrated in Figure 6.10b, the GB planes are not parallel to the viewing direction. Figure 6.10c shows a HRTEM micrograph of the cross-sectional specimen, where such "imperfect"GB with a

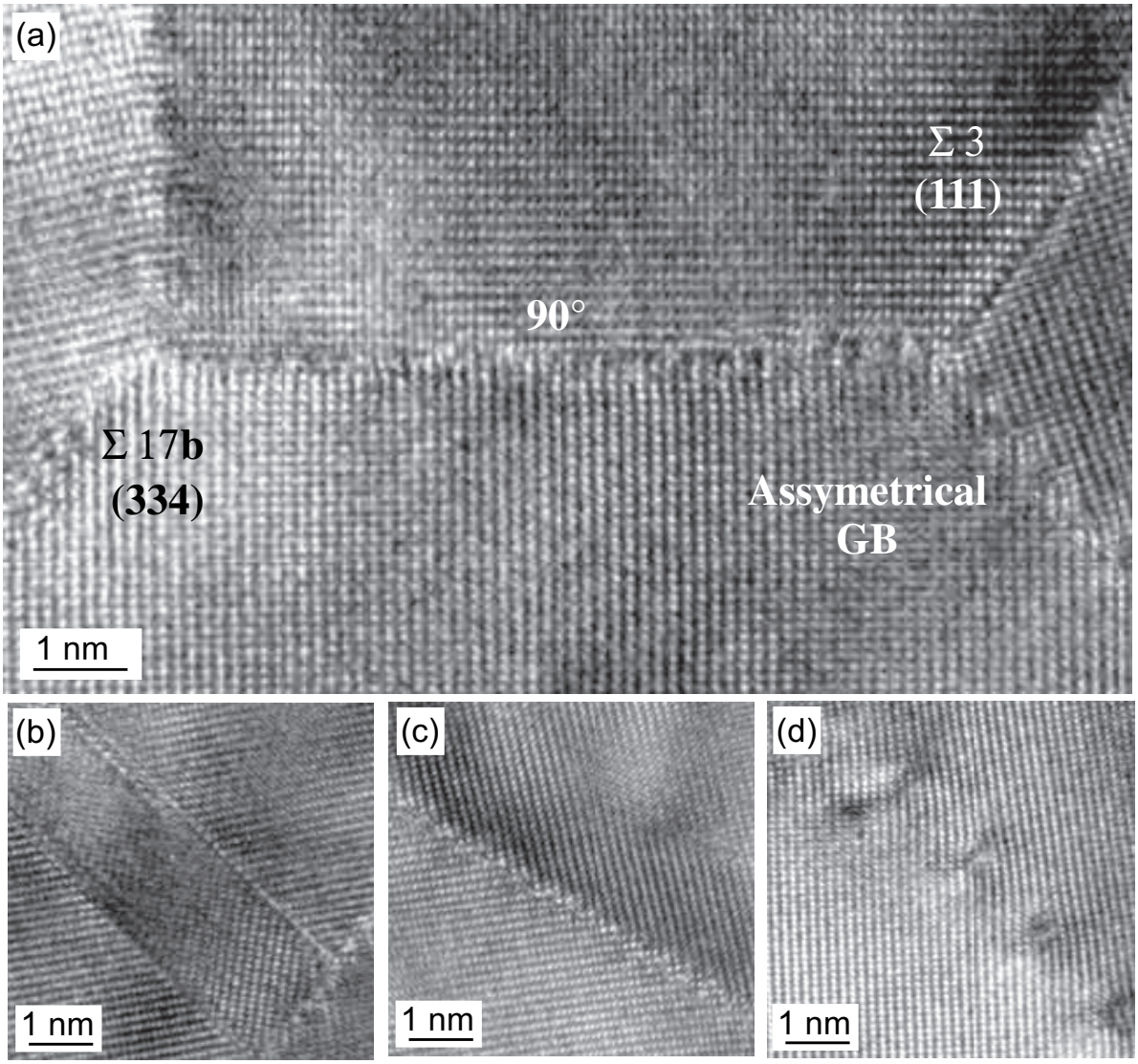

Figure 6.9: HRTEM micrographs of the plan-view $Mo/SrTiO_3$ specimen revealing (a) grain boundaries structures. Additionally, HRTEM images of (b) a Σ3 twin lamella, (c) a Σ17b grain boundary and (d) a 7.5° low-angle grain boundary are shown.

curved GB plane was observed.

Approximately 60% of all grain boundaries were found to be special symmetrical tilt (110) grain boundaries (Table 6.1). About 40% of grain boundaries were found to be Σ3 (112) and Σ17b (334), which are low energy grain boundaries in Mo [Tsurekawa1993]. About one fourth of all boundaries was represented by asymmetrical GBs. The results are summarized in Table 6.1.

Table 6.1: Distribution of experimentally observed grain boundaries.

Symmetrical Tilt GB	GB Plane	% (58 GBs=100%)
Σ3	(112)	29
Σ3	(111)	5
Σ17b	(334)	8.6
Σ17b	(223)	3.5
Σ33a	(144)	3.5
Σ83a	(119)	12
Low Angle GB		
$14° - 15°$		5
$10°$		12
$7° - 8°$		1.7
Other GB		19.7

6.2 Interpretation

6.2.1 Near Coincidence Site Lattice Model (NCSL)

The NCSL model [Balluffi1982, Hwang1990] was applied to determine possible interfacial configurations with a high density of near coincidence sites, which might indicate structures with a low interface energy. Given that the ⟨110⟩ rotation axis of Mo is always normal to the $SrTiO_3$ surface, a simplified two-dimensional (2D) version of this theory was used.

For the calculation of the NCSL the TiO_2 termination of $SrTiO_3$ was chosen. This was justified by the results of *ab-initio* calculations [Classen2001], which have shown that the TiO_2 termination is energetically preferred since its configuration exhibits a lower interface energy than the SrO terminated interface configuration. According to Classen [Classen2001], it is expected that Mo atoms sit on top of the oxygen atoms, leading to pronounced Mo-O bonds, although some additional metallic bondings between Ti and Mo were found. These results were confirmed by EELS investigations performed by Gao *et al.* [Gao2003]. For the EELS experiments the same Mo/$SrTiO_3$ specimens that were investigated in the present study were taken. According to the EELS study, Sr atoms are not involved in the bonding

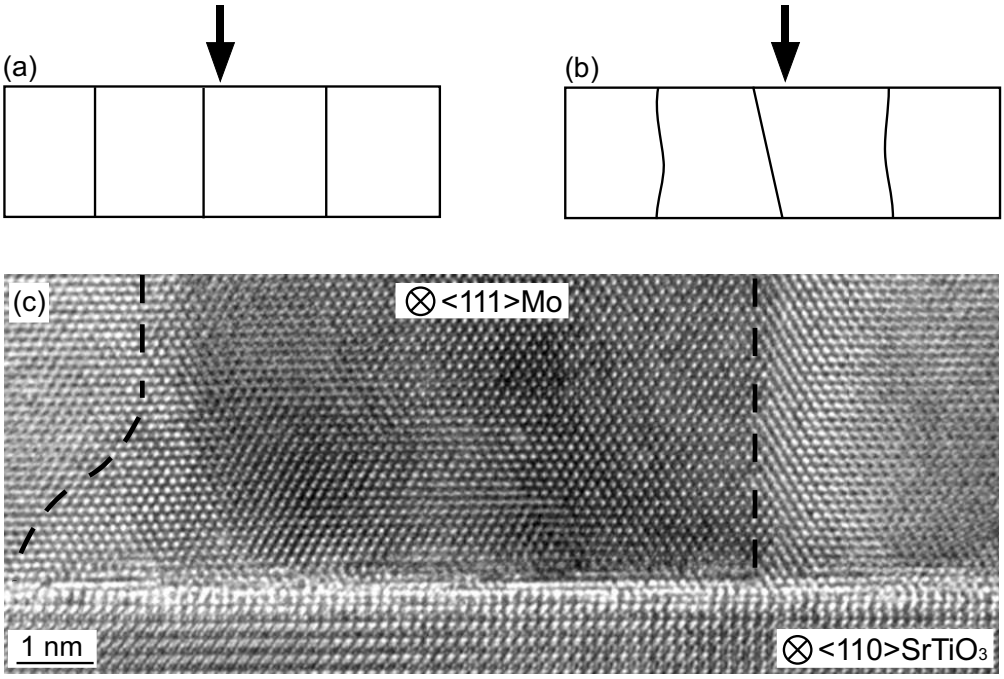

Figure 6.10: Schematic drawing of (a) GBs in cross-section with GB planes parallel to the viewing direction and (b) "imperfect" GB planes with GB planes curved and inclined. The arrows indicate the viewing direction for the plan-view specimen. HRTEM micrograph (c) taken in $\langle 110 \rangle_{STO}$ zone axis at cross-sectional specimen showing the presence of both straight and curved GB planes, which are marked by dashed lines.

and the $SrTiO_3$ terminates at the interface with a TiO_2 layer [Gao2003].

The calculated NCSL for oxygen and titanium sub-lattices were examined. Only results for the oxygen (O) sub-lattice will be presented here. The positioning of Mo on top of the Ti was also tested, but the results do not differ significantly from those for the Mo/O case due to the symmetry of the system. The programm set-up for NCSL calculations and the results for the Ti sublattice are described in details in the Appendix A.

Translation vectors $\mathbf{T}_{Mo} = \mathrm{k}\mathbf{a}_1 + \mathrm{l}\mathbf{a}_2$ and $\mathbf{T}_{STO} = \mathrm{m}\mathbf{b}_1 + \mathrm{n}\mathbf{b}_2$ were used for analysis. Here, **a** and **b** are lattice unit vectors of 2D lattices of $SrTiO_3$ and Mo, respectively; k,l,m,n represent integers (Fig. 6.11). O and Mo atoms were placed at the origin of the NCSL. At the zero rotation position, the angle Θ between the $\langle 110 \rangle_{STO}$ and $\langle 111 \rangle_{Mo}$ was set to be $\Theta = 35.25°$ and the $\langle 110 \rangle_{STO}$ direction was parallel to the $\langle 110 \rangle_{Mo}$ direction.

The degree of coincidence is denoted by σ, which represents the unit cell size of the

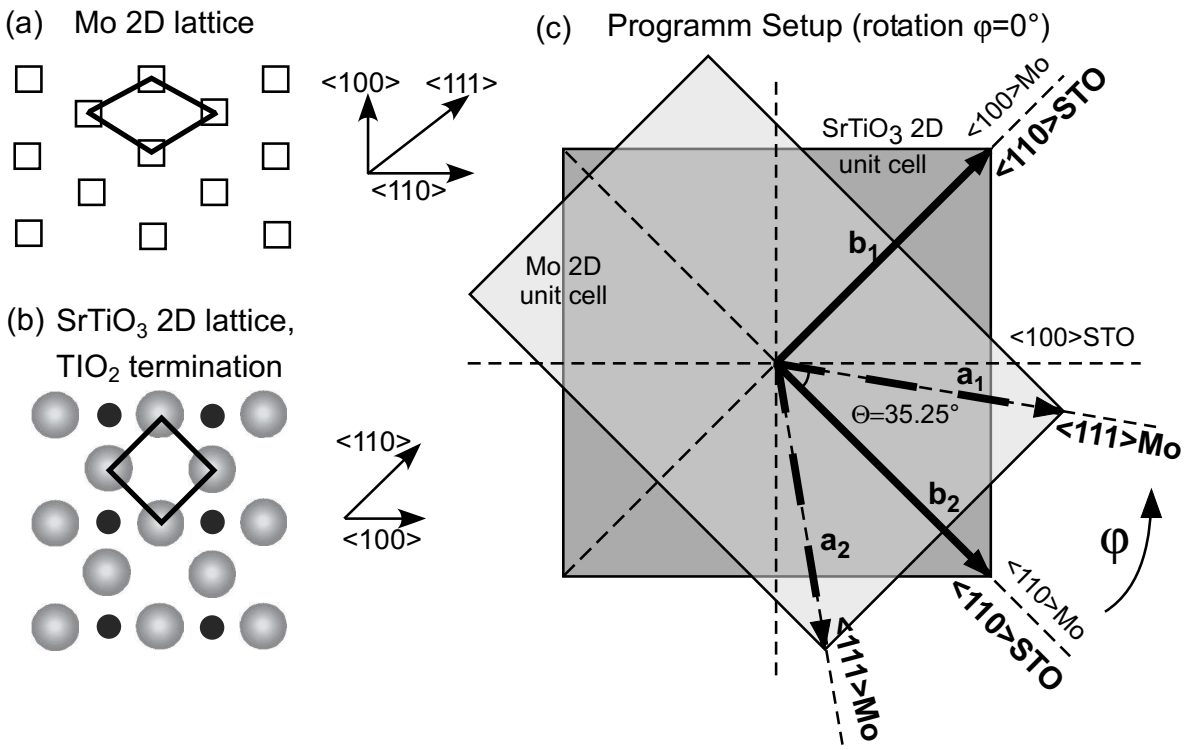

Figure 6.11: Sketch of the calculation setup, used in this work to determine the possible NCSL configurations: (a) Mo 2-dimensional lattice with marked unit cell, (b) $SrTiO_3$ 2-dimensional lattice with unit cell marked, and (c) initial positioning of the zero translation vector compoents $\mathbf{a}_{1\,Mo}$ and $\mathbf{a}_{2\,Mo}$ (dashed arrows), and $\mathbf{b}_{1\,STO}$ and $\mathbf{b}_{2\,STO}$ (solid arrows), for the angle of rotation φ=0.

two-dimensional NCSL. NCSL unit cells σ_{Mo} and σ_{SrTiO_3} are defined as $\sigma_{Mo} = \mathrm{k}^2 + \mathrm{l}^2$ and $\sigma_{STO} = \mathrm{m}^2 + \mathrm{n}^2$, respectively.

In the calculation, the $(110)_{Mo}$ surface is rotated about a surface normal by an angle φ, and the size of the NCSL unit cell σ is calculated (see Appendix A). Since it is not possible to achieve a perfect coincidence between Mo and $SrTiO_3$ lattices because of the lattice misfit, the degree of coincidence misfit δ is also calculated:

$$\delta = \frac{2(\mathbf{T}_{Mo} - \mathbf{T}_{STO})}{\mathbf{T}_{Mo} + \mathbf{T}_{STO}}. \tag{6.1}$$

The degree of coincidence misfit describes how well the atoms of one lattice fit on top of the atoms of the other lattice at the corners of the calculated NCSL unit cell. It is always possible to choose a smaller unit cell size σ with a larger degree of coincidence misfit δ. However, it will not correspond to the lowest energy configuration from a geometrical point of view, since

Table 6.2: Possible NSCLs for Mo on O sub-lattice. NCSL unit cells σ_{Mo} and σ_{SrTiO_3} are defined as $\sigma_{Mo} = k^2 + l^2$ and $\sigma_{SrTiO_3} = m^2 + n^2$, respectively.

Misorientation $\varphi(^\circ)$	σ_{Mo}	σ_{SrTiO_3}	Coincidence misfit $\delta(\%)$	Orientation Relationship
0 *0-3.7*	25 *25*	25 *25, 18*	3.01 *3.01-3.9*	$\langle 110\rangle_{Mo}\|\|\langle 110\rangle_{STO}$ OR III
9.7 *7.8-10.1*	16 *16*	13 *13*	3.36 *1.8-3.9*	$\langle 111\rangle_{Mo}\|\|\langle 100\rangle_{STO}$ OR IV
35.3 *33.2-37.4*	1 *1, 11*	1 *1, 11*	1.2 *1.2-3.8*	$\langle 111\rangle_{Mo}\|\|\langle 110\rangle_{STO}$ OR II
45 *44.8-46.8*	29 *26, 29*	25 *25, 26*	3.6 *0.6-3.2*	$\langle 110\rangle_{Mo}\|\|\langle 100\rangle_{STO}$ $\langle 100\rangle_{Mo}\|\|\langle 100\rangle_{STO}$ OR I a,b

the atoms of one lattice at the corners of the NCSL unit cell will not sit on top of the other lattice atoms. Thus, both parameters should be kept as small as possible.

Table 6.2 summarizes the results for the NCSL with an O sub-lattice. The following limitations were applied to the calculation: k, l, m, n ≤ 10, $\delta \leq 4\%$ and $\sigma \leq 25$. Only (sigma) values corresponding to possible orientation relationships with $\delta \leq 4\%$ and $\sigma \leq 25$ are listed. The data resulting with random rotations are neglected.

The optimum case is found for φ=35.3° with $\langle 111\rangle_{Mo}\|\langle 110\rangle_{STO}$ (Fig. 6.12b). Here the NCSL unit cell fits into one Mo and one $SrTiO_3$ primitive unit cells with a misfit of coincidence $\delta = 1.2\%$. This variant is also observed in the experiment (OR II) and has the smallest misfit 1.1% along the $\langle 111\rangle_{Mo}\|\langle 110\rangle_{STO}$. Another experimentally observed variant (ORI) lies at the $\varphi = 45^\circ$ rotation angle in the calculation and has a larger coincidence misfit, $\delta = 3.6\%$ (Fig. 6.12a). The NCSL unit cell is much larger in this case (29 Mo : 25 $SrTiO_3$). Although two other calculated ORs, found at $\varphi = 9.7^\circ$ (OR III) and $\varphi = 0^\circ$ (OR IV), have smaller sized NSCL unit cells in comparison to that of OR I (Fig. 6.12c,d), these variants were not detected in the experiment.

The angular deviations from the perfect orientation were also predicted by the model

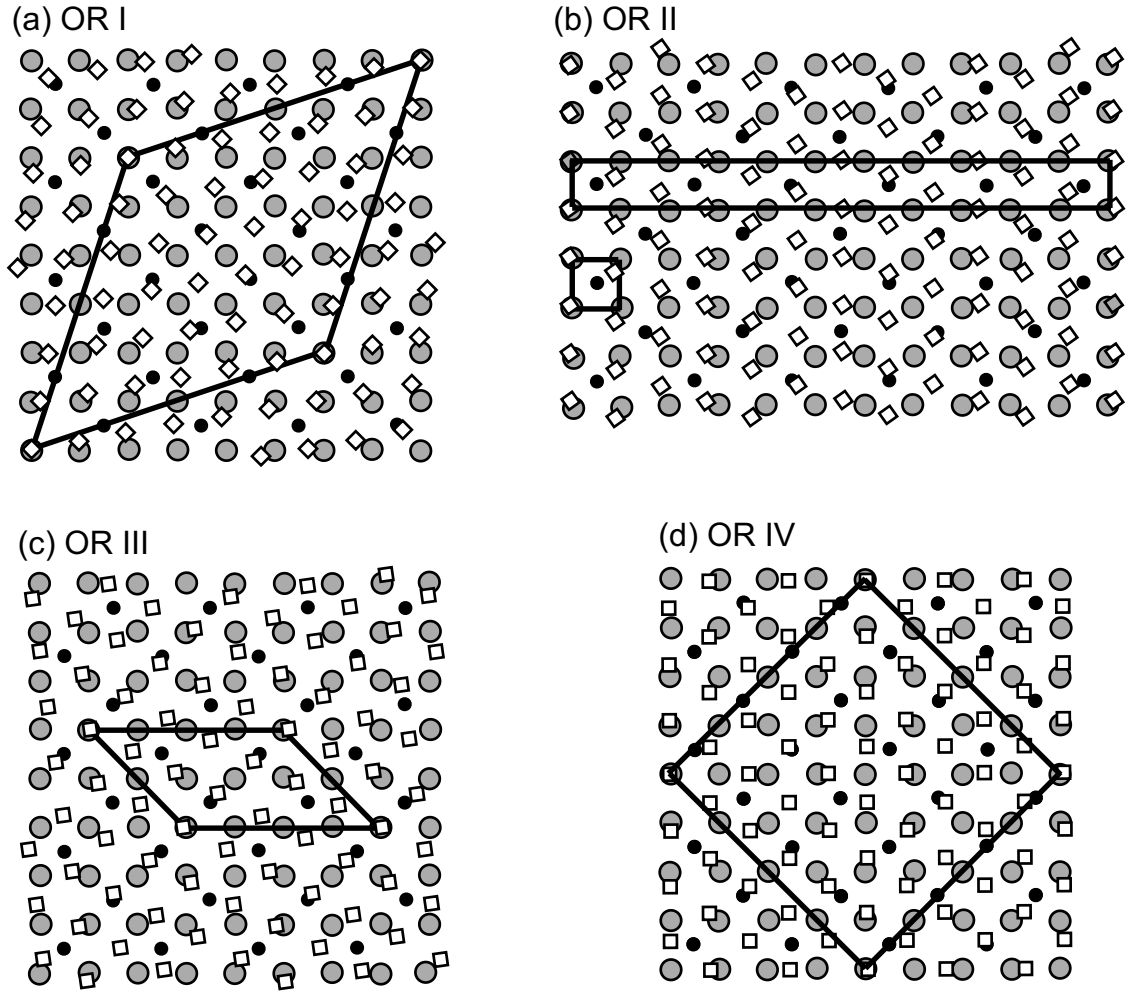

Figure 6.12: Drawing of the best NCSLs for (a) OR I type domains, (b) OR II type domains, (c) OR III type domains an (d) OR IV type domains.

(*italic rows* in Table 6.2). For example, for OR II with $\varphi = 35.3°$ and $\sigma = 1$ a deviation of φ in the range between 33.2° and 37.4° was found. The coincidence misfit is varying between 1.2% and 3.8%, and still satisfy the condition $\delta < 4\%$. These possible deviations of the in-plane texture correspond to those that were observed in the XRD pole figure and in the TEM SAD investigations of plan-view specimens.

6.3 Discussion

6.3.1 NCSL Model

The validity of the NCSL model is questionable, since simple geometrical considerations can not ensure a low energy configuration [Sutton1987]. In general, the interfacial energy depends upon both the atomic structure and the bonding at the interface [Sutton1987]. Nevertheless, Hwang *et al.*, studying YBCO superconducting films on MgO substrates [Hwang1990] and Mykura *et al.*, investigating MgO/CdO interfaces [Mykura1980], have found that all observed ORs match well with the prediction of the NCSL theory. On the other hand, Dickey *et al.* [Dickey2002] observed that for the Ni/ZrO_2 system only one of the detected orientation relationships could be successfully explained within this model.

In the case of the Mo/$SrTiO_3$ system, investigated in this work, the NCSL model predicts that OR II and III for both O and Ti sub-lattices should be favorable since these ORs have a higher density of near coincidence sites (see Table 6.2). However, in the experiment we observed OR II and OR I. OR II matches very well with the prediction of NCSL, as well as its deviants (0.5°-5°). It has a close packed $\langle 111 \rangle_{Mo}$ direction running parallel to the $\langle 110 \rangle_{STO}$ direction, where the mismatch between Mo and $SrTiO_3$ is only 1.1%.

6.3.2 Texture formation

Mo films grown at a substrate temperature of T=600°C were found to establish two different epitaxial orientation relationships with the substrate. The $(110)_{Mo}$ plane is found to be always parallel to the interface. The preferred (110) growth direction is typical for bcc metals since this close packed plane has the lowest surface energy. One of the orientations (OR I) was previously observed by Wagner *et al.* [Wagner2001] by *in situ* RHEED investigations, while the other orientation, OR II, is reported by Fu *et al.* [Fu2003].

The observed in-plane texture indicates strong local minimization of the interfacial energy of the system, which is the main reason for in-plane texture formation. The substrate influences the texture formation by suppressing the growth of one orientation and favoring the other configuration due to its lower interfacial energy [Knorr1994].

The growth mechanisms of the Mo can be understood by considering the Mo unit cell

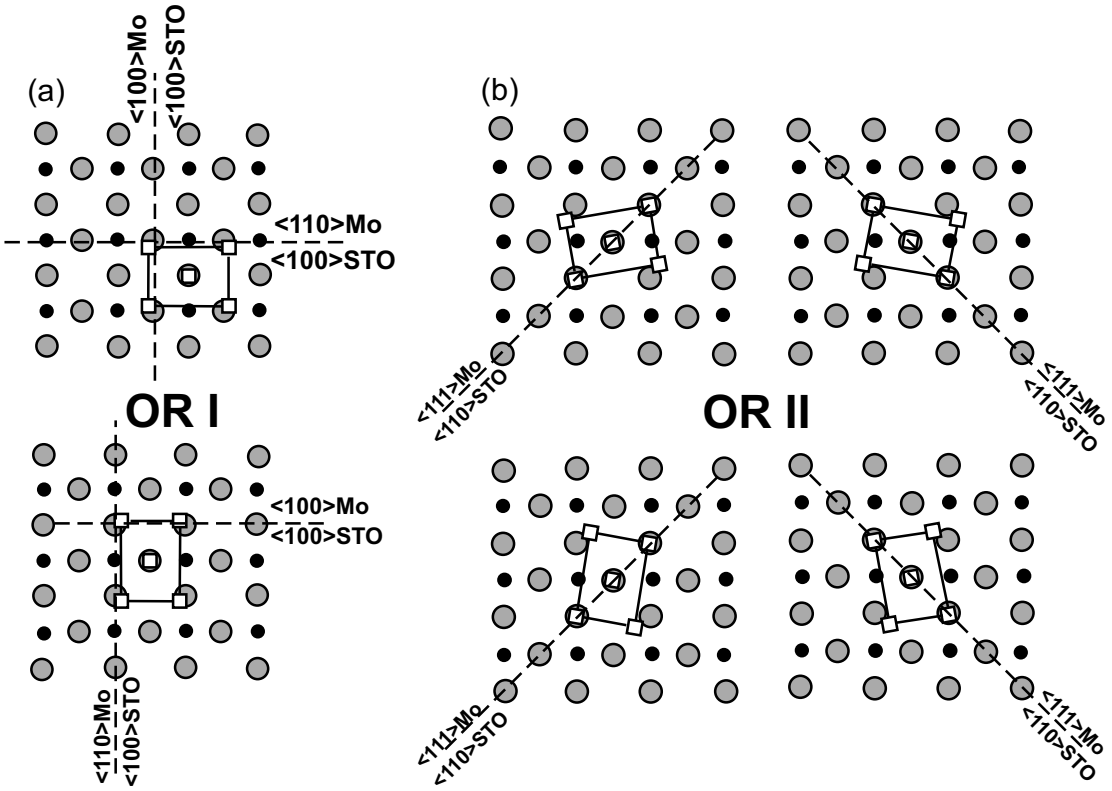

Figure 6.13: Configurations of the Mo (100) unit cell on the (100) $SrTiO_3$ substrate, terminated by TiO_2: (a) OR I with high lattice mismatch (12% and 24 %), (b) OR II with low lattice mismatch (1.1%) for the $\langle 111 \rangle_{Mo}$ to $\langle 110 \rangle_{STO}$ direction.

positioned on top of the $SrTiO_3$ surface. In Figure 6.13 all possible rotations of the OR I (Fig. 6.13a) and OR II (Fig. 6.13b) are drawn schematically. Since the molybdenum normally grows in a 3D Volmer-Weber growth mode, [Wagner2001, Blondeau2002] it can be assumed that in the first stage of the growth, at nominal thickness of about 1-2 MLs, a completely coherent interface is formed. I.e. Mo atoms are placed directly on top of the oxygen atoms of the $SrTiO_3$. In such a case the Mo would have an abnormal fcc-like structure with the lattice parameter of the $SrTiO_3$ (a = 0.3905 nm) as experimentally observed by Fu *et al.* [Fu2003]. A similar structure was predicted by ab-initio calculations [Classen2001]. The formation of such a structure is due to the minimization of the elastic energy, since for a thickness of 1 to 3 monolayers it is energetically favorable for the molybdenum to form an fcc-like metastable structure rather than forming misfit dislocations [Classen2001]. As growth continues, the bulk energy of Mo dominates and the influence of the interface on the bulk metal is reduced,

so it cannot remain in the fcc configuration.

The formation of the fcc-like phase in very thin Mo films was also observed in the early work of Denbigh and Marcus [Denbigh1966], who deposited Mo on MgO substrates. The formation of fcc Mo on the initial growth stages was reported, which tended to transform into the bcc phase as the film thickness increased. The bcc structure was first observed at a thickness of about ~ 4 nm. The measured lattice parameter of fcc Mo was ranging between $0.419 - 0.427$ nm, while in the presented study a value of 0.405nm was found. Kacim and co-workers [Kacim1994] also reported formation of fcc as well as bcc phases of Mo, depending on the film deposition method and sputtering rates. The lattice parameters of fcc Mo were found to vary between 0.415 and 0.422 nm. The authors claim that the presence of non-metallic elements such as O, N and C is responsible for the stabilization of the fcc Mo structure [Kacim1994]. However, in the case of $Mo/SrTiO_3$, N and C atoms were not detected by AES technique up to the detection limit of 0.1 at%, and the amount of O atoms was found to be 7.5 at% for the 50 nm thick films.

Nuclei-islands start to align themselves along those directions of the substrate that lead to reduction of the interface energy. Differently oriented islands attempt to form an interface with the substrate that has a minimum misfit and strain energy, maximally high lattice coincidence and thus minimum interface energy [Chan1994]. At this point the preferred orientations driven by relaxation of the structure begin to develop. The further coalescence of the grains is accompanied by a rotation of the grains into twin orientations, which minimize the grain boundary energy and thus the total energy of the system.

The angular deviations from the ideal ORs have most likely occured at the coalescence stage. When grains with different ORs are brought together, the formation of low-energy special grain boundaries is favored for those grains that are already positioned not far away from such a configuration. As a consequence, these grains might deviate from the perfect alignment at the interface, trying to achieve the balance between the interface energy and grain boundary energy and thus the lowest total energy configuration.

Low-angle grain boundaries that were observed in the film were most likely formed by merging of slightly misoriented islands during film growth.

Grovernor *et al.* [Grovernor1984] suggested that epitaxy for a given system is not com-

pletely established until the formation of misfit dislocations during the film thickening. Kato *et al.* [Kato1989] assumed that epitaxy is determined in the beginning of the deposition, where the dislocations might have not yet appeared. As it is known from the literature, the formation of misfit dislocations can occur in various ways. According to Swiech *et al.*, [Swiech1999] the stress in the Mo, produced during the film growth by thermal expansion-contraction mechanisms, can be relieved by slip along the closest packed $\langle 111 \rangle$ direction. As the slip propagates through the film, atomic steps appear at the interface and form interfacial dislocations. It is speculated that in case of the Mo/$SrTiO_3$ system the nucleation of the dislocations occurs immediatly after the coalescence. While the directions with the highest coincidence of atoms match, the rest of the non-coherent atomic sites minimize the interface energy through the formation of misfit dislocations and form a semi-coherent interface [Sutton1994].

6.3.3 Conclusions

The present study has demonstrated that only a combined approach of RHEED, XRD and TEM techniques is able to solve the complicated structure of the Mo film and the Mo/$SrTiO_3$ interface. Mo films with nominal thicknesses of 50 nm were found to exist in the regular bcc configuration. An fcc-like structure was observed by *in situ* RHEED only for ultra-thin Mo films (0.6 nm) [Fu2003], which had the estimated lattice parameter of $a_{fcc-like\ Mo} = 4.05 \pm 0.10$ Å. However, it was found that the formation of such metastable configuration occurs not due to presence of impurities, but due to the minimization of the total energy. For thicknesses above 2 nm the regular bcc Mo structure was observed. The films with a nominal thickness of 50 nm had the regular bcc structure. A (110) texture of the Mo film with 2 geometrically inequivalent types of domains, each consisting of 2 and 4 geometrically equivalent variants, was observed. Most of the grain boundaries between the various domains are special tilt GBs with a low energy configuration, which is directly linked to the minimization of the total energy in the system. The presence of misfit dislocations at the Mo/$SrTiO_3$ interface indicates strong bonding characteristics. EELS experiments [Gao2003] and *ab initio* calculations [Classen2001] revealed that the Mo forms strong bonds with the O atoms and some weaker metallic bonding with Ti. The thermal stability of the different

types of domains and the preferential grain growth has to be investigated in the future. Furthermore, for a quantitative study of the atomic interfacial structure at the interface better specimen preparation techniques are required.

Chapter 7

$Pd/SrTiO_3$

Detailed studies of the growth behavior and morphology of Pd films deposited on $SrTiO_3$ (100) substrates as well as of the bonding charachteristics at the $Pd/SrTiO_3$ interface can be found in the literature [Richter2000, Wagner2001, Benthem2002]. Therefore, the experimental results concerning the morphology of the Pd films used in the present work as well as the orientation relationship between the Pd and $SrTiO_3$ are only shortly described in Section 7.1. Experimental HRTEM and STEM-HAADF images are also presented in this section. Section 7.2 describes the results of the quantitative HRTEM analysis of the experimental images. The results concerning the determination of the projected bonding distance at the $Pd/SrTiO_2$ interface and the atomic structure at the interface are described in Section 7.3.

7.1 Experimental

In the following subsections the experimental results obtained by CTEM and HRTEM are presented. The growth procedure and orientation relationship between the Pd and the $SrTiO_3$ are described in Section 7.1.1. The HRTEM and STEM-HAADF investigations of the $Pd/SrTiO_3$ interface are given in Section 7.1.2.

7.1.1 Film Structure and Orientation Relationship with $SrTiO_3$

The growth behavior of Pd films with nominal thicknesses of 30 nm deposited on (100) $SrTiO_3$ was studied in detail by RHEED, XRD and CTEM by Richter [Richter2000] and Wagner *et*

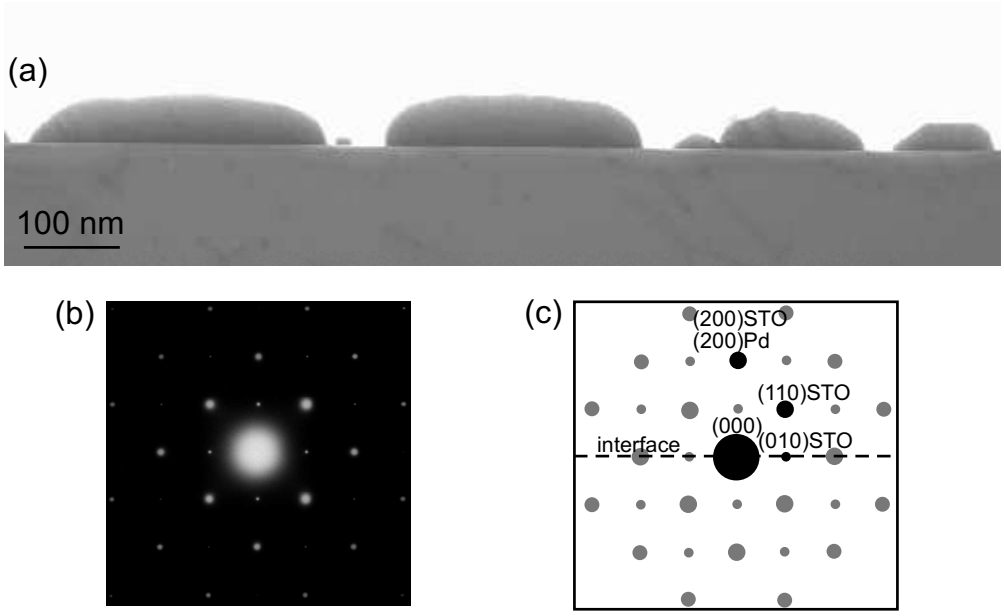

Figure 7.1: CTEM of the Pd/$SrTiO_3$ cross-sectional specimen in $\langle 100 \rangle_{STO}$ zone axis: (a) bright-field image of Pd islands on top of the $SrTiO_3$ substrate, (b) SAD pattern used to determine the OR between Pd and $SrTiO_3$, and (c) schematic drawing of the SAD pattern, revealing the presence of a cube-on-cube OR.

al. [Wagner2001]. The results indicated a 3-dimensional growth of Pd islands on $SrTiO_3$. An epitaxial cube-on-cube OR between Pd and $SrTiO_3$ was determined, where the cubic planes and direction of both materials were parallel and perpendicular to each other [Richter2000].

The Pd films studied in the present work were grown by MBE at UHV conditions at a substrate temperature $T_{substrate} = 650°C$ with a nominal thickness of 50 nm. 3-dimensional growth of Pd islands were also observed for these films, which is in agreement with previous results [Richter2000, Wagner2001]. Figure 7.1a shows a CTEM micrograph of the cross-sectional Pd/$SrTiO_3$ specimen taken in $\langle 100 \rangle_{SrTiO_3}$ zone axis revealing the formation of Pd islands on the $SrTiO_3$ substrate.

The OR between Pd and $SrTiO_3$ was determined by SAD experiments (Fig. 7.1b). The diffraction pattern in Figure 7.1b represents a superposition of the reflections originating from fcc Pd and perovskite $SrTiO_3$. The reflection could not be resolved separately since the lattice mismatch between both materials is only $f = -0.4\%$. The superposition, sketched schematically in Figure 7.1c, reveals a cube-on-cube orientation relationship:

$\{100\}_{Pd} \parallel \{100\}_{STO}$;

$\langle 100 \rangle_{Pd} \parallel \langle 100 \rangle_{STO}$.

Other orientation relationships were not observed for the investigated specimens. This is in accordance to the results reported by Richter and Wagner *et al.* [Richter2000, Wagner2001].

7.1.2 Atomic Structure of the $Pd/SrTiO_3$ Interface

HRTEM investigations

Detailed HRTEM investigations were performed in order to determine the atomic structure of the $Pd/SrTiO_3$ interface using the JEM-ARM 1250 and JEM-2010F transmission electron microscopes. The micrographs were recorded on negatives at a magnification of 600K. For the determination of the atomic structure and the translation state at the interface between the two lattices, at least two different projections of the interface have to be considered. Therefore, HRTEM images of the $Pd/SrTiO_3$ interfaces were taken in $\langle 100 \rangle_{STO}$ and $\langle 110 \rangle_{STO}$ projections.

Figure 7.2a shows a HRTEM micrograph of the $Pd/SrTiO_3$ interface taken in $\langle 100 \rangle_{STO}$ zone axis. No reaction phase occurs and the interface is abrupt. The inspection of larger areas of the specimen revealed the presence of steps in the substrate with heights of one $SrTiO_3$ unit cell. Such steps, caused by the surface preparation procedure, were also detected by Polli *et al.* [Polli1999] and Richter [Richter2000] by STM investigations of as-prepared $SrTiO_3$ surfaces. Detailed inspection of the micrograph in Figure 7.2a revealed a slight inclination of the Pd (100) planes that are perpendicular to the interface plane. This is shown in more detail in Figure 7.3. Here, the (100) planes of $SrTiO_3$ are indicated by solid lines and Pd planes by dashed lines. In addition, a reference line is drawn parallel to the $\langle 100 \rangle_{STO}$ direction and perpendicular to the interface plane. The inclinations of Pd (100) planes might be related to a bending of the specimen due to mechanical instabilities. This occurs at thin areas of the specimen edge.

A different TEM specimen was prepared for the $\langle 110 \rangle_{STO}$ zone axis. The corresponding HRTEM micrograph shows also an abrupt interface (Fig. 7.2b). No misfit dislocations were detected. However, the substrate termination and the atomic structure at the interface can not be determined directly from the experimental images (see Section 4.2.2). The interpretation of the HRTEM images performed by image simulation will be described in Section 7.2.

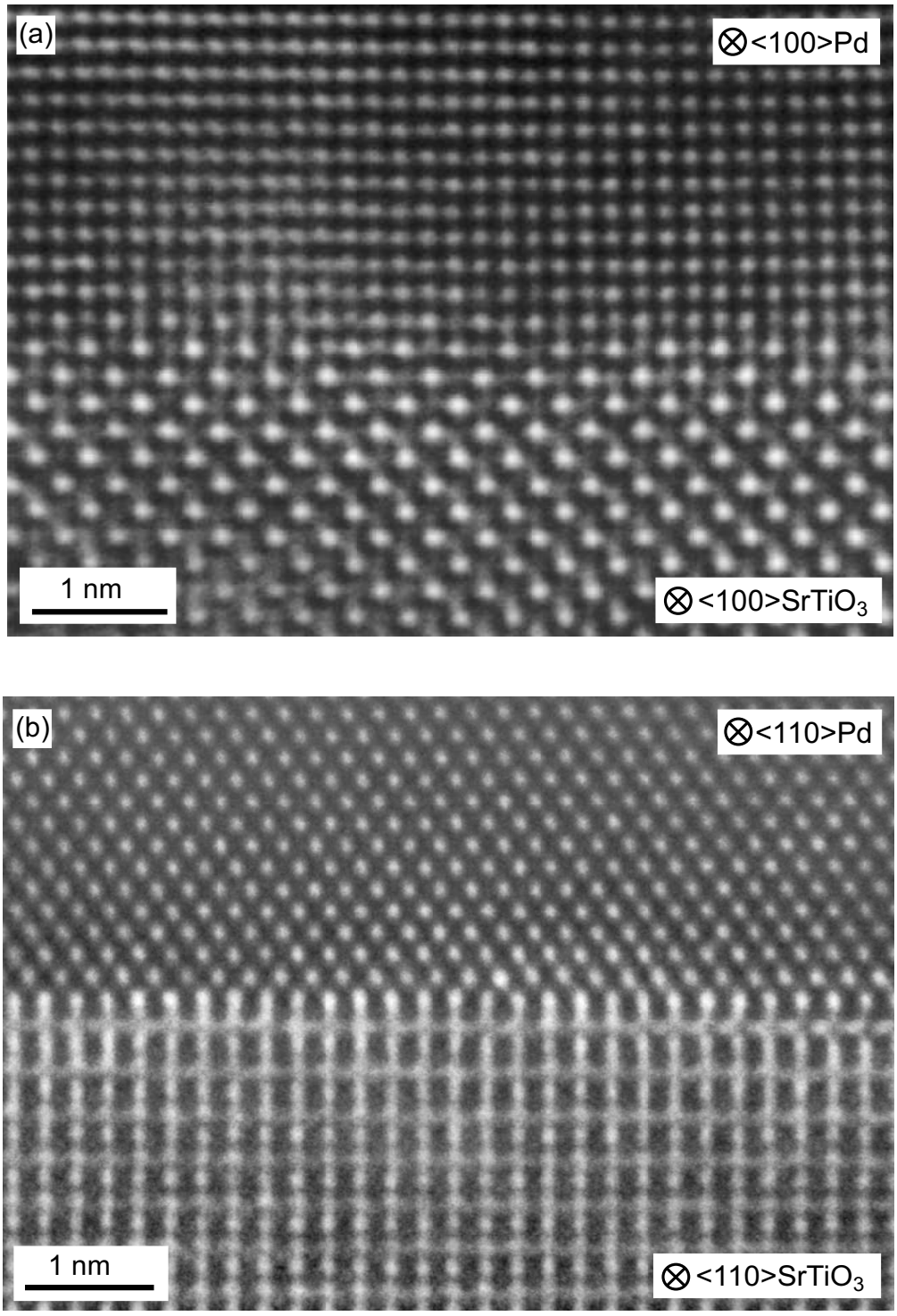

Figure 7.2: HRTEM micrographs of the Pd/$SrTiO_3$ cross-sectional specimen in (a) $\langle 100 \rangle_{STO}$ zone axis, and (b) in $\langle 110 \rangle_{STO}$ zone axis. Both images reveal an atomically abrupt interface. Misfit dislocations could not be observed. The micrographs are taken from different TEM specimens, prepared separately for $\langle 100 \rangle_{STO}$ and $\langle 110 \rangle_{STO}$ directions.

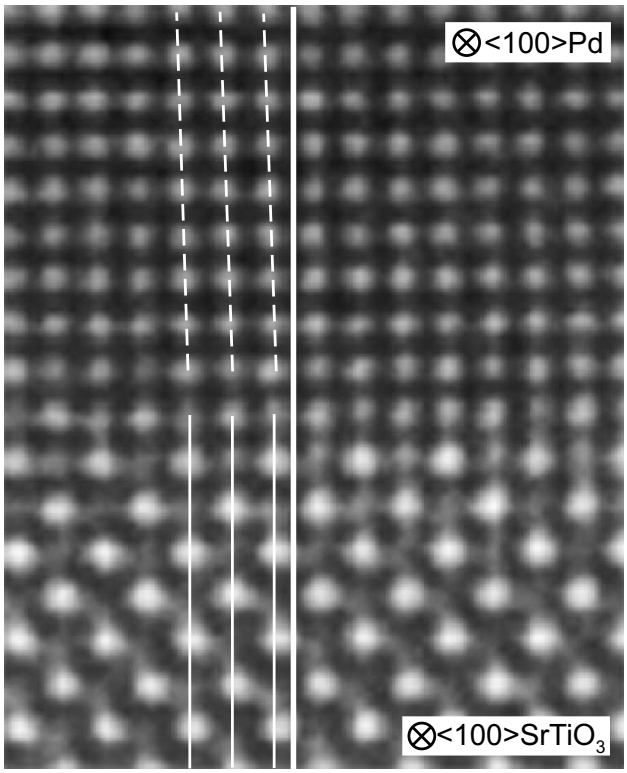

Figure 7.3: HRTEM image of the $Pd/SrTiO_3$ interface in $\langle 100 \rangle_{STO}$ zone axis showing the inclination of the Pd planes.

STEM-HAADF investigations

STEM-HAADF investigations[1] were performed on the $Pd/SrTiO_3$ interface viewed in $\langle 110 \rangle_{STO}$ zone axis in order to determine the terminating plane of the STO at the interface. This technique allows a more direct interpretation of the obtained images compared to HRTEM (see Section 4.2.4), if the electron probe diameter is smaller than the lattice spacings. Figure 7.4a shows an experimental HAADF micrograph. A large jump of the intensity between the Pd and $SrTiO_3$ sides can be seen. This intensity jump is due to the higher scattering amplitude of the Pd atoms, which have a larger Z-value compared to that of $SrTiO_3$ atoms (see Fig. 7.4c). To reduce the contrast jump and to make the periodicity in the image more pronounced, a Bragg filtering procedure was performed (Fig. 7.4b). The filtered image in Figure 7.4b also reveals distortions of the lattices. These distortions are due to instabilities of the scanning unit.

[1]The experiments were performed at the JEM-2010F FEG microscope in collaboration with M. Čeh and S. Šturm at the Jošef Štefan Institute Institute, Ljubljana, Slovenia.

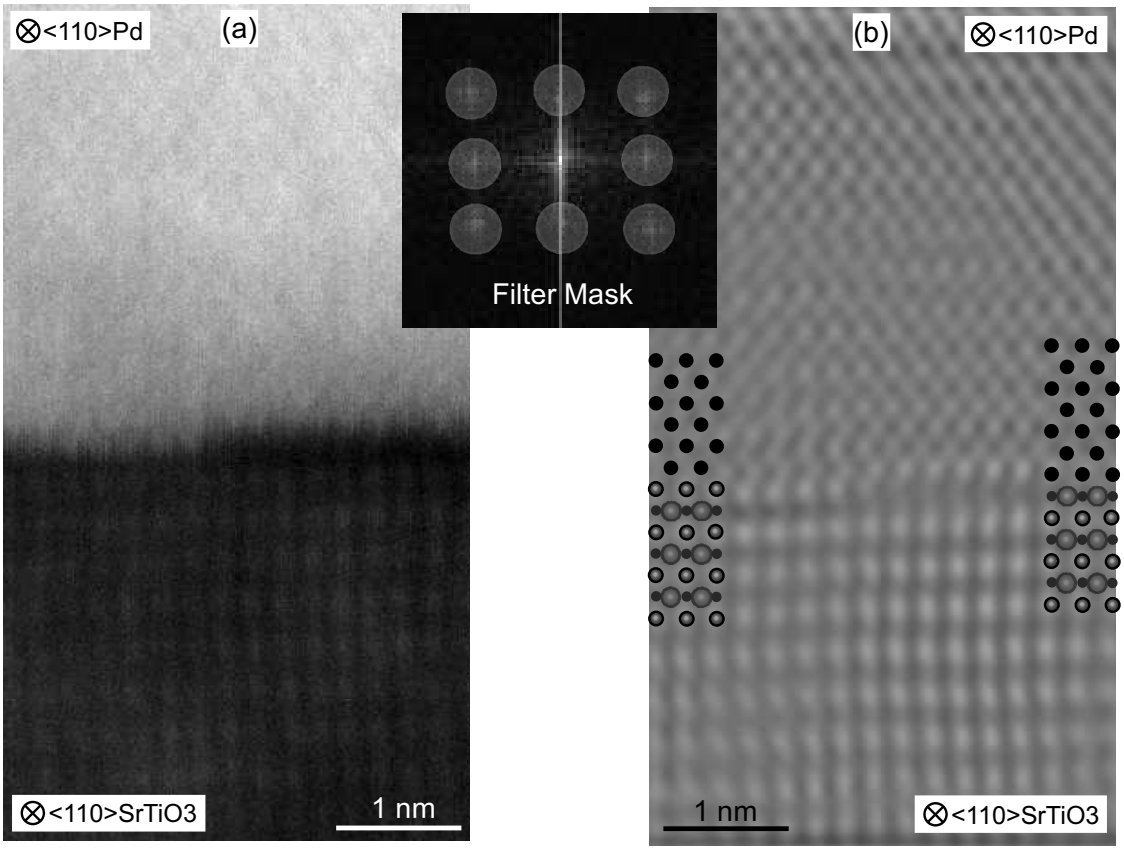

(c)

Atom	Pd	Sr	Ti	O
Z	46	38	22	8

Figure 7.4: HAADF micrographs of the Pd/$SrTiO_3$ cross-sectional specimen (a) raw experimental image taken in $\langle 110 \rangle_{STO}$ zone axis, (b) FFT-filtered image, demonstrating the lattice periodicity in the specimen, and (c) Z-values for the different atoms belonging to the investigated structure.

On the $SrTiO_3$ side, the spots with the higher intensity are caused by Sr atoms, since these have the largest scattering cross-section ($Z_{Sr} = 38$) among all atoms present in the $SrTiO_3$ structure ($Z_{Ti} = 22$, $Z_O = 8$). On the Pd side, the number of atoms with a large scattering cross-section is much higher, but the intensity spots are smaller than those corresponding to the Sr atoms in $SrTiO_3$. Therefore, a qualitative interpretation of the chemical composition at the interface can be performed.

The detailed analysis of the filtered image showed, that two different interface structures might be simultaneously present (Fig. 7.4b, interface structure models as insets). The left

part of the filtered image can be interpreted by a SrO termination of $SrTiO_3$ with Pd atoms sitting in between the Sr atoms, while the right part of the image indicates a TiO_2 termination with the Pd atoms sitting on top of Ti atoms and above the hollow sites. However, for a more precise quantitative analysis, better quality HAADF images of the interface are required.

7.2 HRTEM Image Simulations

In the following section the quantitative analysis of the HRTEM images by means of image simulation techniques is presented. From the comparison of the experimental micrographs with the simulated images information on the atomic structure of the interface can be retrieved. Subsection 7.2.1 introduces the possible models of the $Pd/SrTiO_3$ interface, which are used for the image simulations. The determination of the translation state at the interface between Pd and $SrTiO_3$, e.g. of the projected bonding distance, is performed using the modified method of Schweinfest *et al.* [Schweinfest1998] (see Section 4.2.3). The results are described in Subsection 7.2.2. The investigations of the atomic structure determination of the $Pd/SrTiO_3$ interface are presented in Subsection 7.2.3.

7.2.1 Models of the $Pd/SrTiO_3$ Interface

In order to simulate HRTEM images, a known initial structure model is required (see Section 4.2.2). For the $Pd/SrTiO_3$ interface, four possible variants of the atomic structure at the interface were considered. Figure 7.5 represents top view drawings of possible positions of Pd atoms of the $(100)_{Pd}$ plane on top of TiO_2 and SrO terminated $(100)_{STO}$ surfaces, respectively. The positions where the $(100)_{Pd}$ plane is fitted on top of $(100)_{STO}$ are marked by arrow heads. For the case sketched in Figure 7.5a, all Pd atoms sit directly above the O atoms of the TiO_2 termination. For the case sketched in Figure 7.5b, half of the Pd atoms sit directly above the Ti and the other half is positioned above the hollow sites of the TiO_2 termination. For the SrO termination of $SrTiO_3$, the Pd atoms are placed either directly above the Sr and O atoms (Fig. 7.5c), or above the hollow sites in between the Sr and O atom positions (Fig. 7.5d).

Figure 7.6 represents possible structure models of the $Pd/SrTiO_3$ interface viewed in

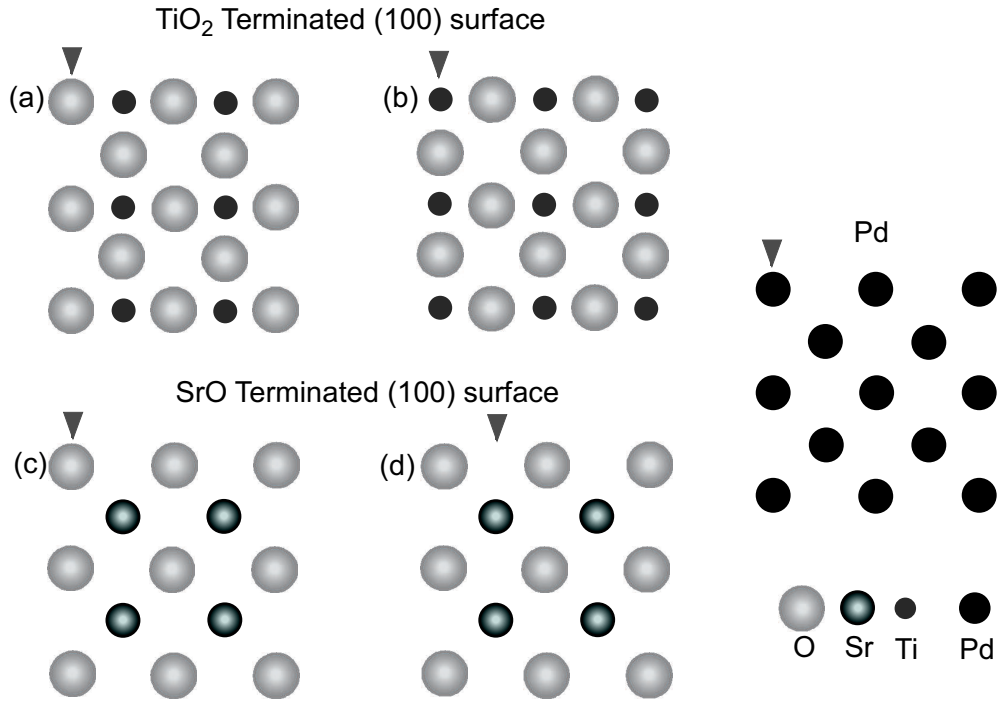

Figure 7.5: Top view of possible positions of Pd atoms on top of SrO and TiO_2 terminated $(100)_{STO}$ surfaces: (a) TiO_2 termination with Pd on top of the O (TiO_2/Pd-O), (b) TiO_2 termination with Pd on top of Ti and hollow sites (TiO_2/Pd-Ti,gap), (c) SrO termination with Pd on top of Sr and O (SrO/Pd-Sr,O), and (d) SrO termination with Pd positioned on the hollow sites (SrO/Pd-gap). The corresponding positioning is indicated by the arrow heads.

$\langle 100\rangle_{STO}$ and $\langle 110\rangle_{STO}$ directions, respectively. The translation state at the interface, determined as the distance between the terminating layer of $SrTiO_3$ and the first layer of Pd (see section 4.2.3), and the position of the terminating plane are marked in Figure 7.6a.

Due to the projection, the positions of the Pd atoms in variants (a) and (b) with TiO_2 termination and (c) and (d) with SrO termination are indistinguishable in $\langle 100\rangle_{STO}$. Therefore, this projection can be used only to determine the translation state. For the exact evaluation of the atomic structure at the interface, the $\langle 110\rangle_{STO}$ projection has to be used additionally. In this projection, different interface structures can be distinguished (Fig. 7.6).

It is worth to mention here that *ab initio* calculations performed by Ochs *et al.* [Ochs2000] had shown a relaxation of the $SrTiO_3$ surface atoms, which decreases with increasing film coverage. Pd film thicknesses up to 3 ML had been considered [Ochs2000]. Since the thicknesses of the Pd films investigated in this work were much larger (nominal thickness 50 nm),

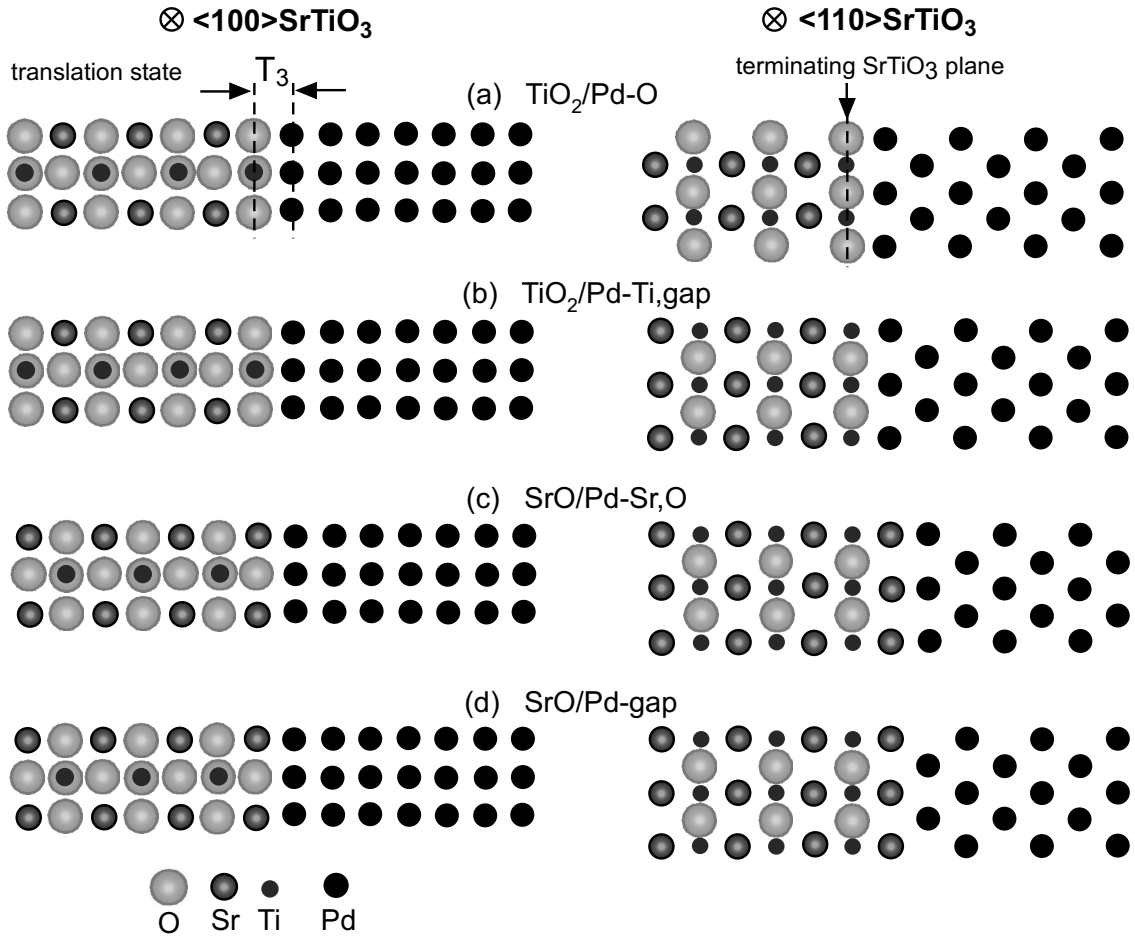

Figure 7.6: Structure models of the $Pd/SrTiO_3$ interface, viewed in $\langle 100 \rangle_{STO}$ and $\langle 110 \rangle_{STO}$ directions: (a) TiO_2 termination with Pd on top of the O (TiO_2/Pd-O), (b) TiO_2 termination with Pd on top of Ti and hollow sites (TiO_2/Pd-Ti,gap), (c) SrO termination with Pd on top of Sr and O (SrO/Pd-Sr,O), and (d) SrO termination with Pd positioned on the hollow sites (SrO/Pd-gap).

models with rigid $SrTiO_3$ lattice were taken for the image simulations.

7.2.2 Determination of the Translation State at the Interface

For the determination of the translation vector component $\mathbf{T}_3$, which is perpendicular to the interface plane, the method described in Section 4.2.3 was employed. The HRTEM micrograph taken in $\langle 100 \rangle_{STO}$ direction was used, since it had the largest areas of uniform contrast on both sides of the interface in comparison to the images taken in $\langle 110 \rangle_{STO}$ direction.

Firstly, simulations using the $Pd/SrTiO_3$ structure models with an a priori $\mathbf{T}_3 = a_{STO}/2 =$

1.9525Å value were performed in order to determine the position of the interface in the experimental image. In the next step, $\mathbf{T}_3$ was calculated using 80 different sets of Pd and $SrTiO_3$ unit cell templates by applying the equations (4.9) and (4.10), described in Section 4.2.3. Finally, the error bars for the $\mathbf{T}_3$ were estimated.

Determination of the interface position in the HRTEM image taken in $\langle 100 \rangle_{STO}$ projection

Prior to HRTEM image simulations of Pd/$SrTiO_3$ in $\langle 100 \rangle_{STO}$ projection, initial values of the specimen thickness and objective lens defocus were determined from the experimental HRTEM image using techniques described in Section 4.2.3.

The initial values of the defocus were calculated using the diffractogramm of an amorphous region (see Section 4.2.3). This is important since the intensity patterns of both $SrTiO_3$ and Pd thickness/defocus maps show a periodic repetition of certain contrast patterns. In the thickness/defocus map for $SrTiO_3$ the same intensity pattern is observed every 30 nm of the defocus change. Figure 7.7 displays a part of the map for defocus values between -56 nm and -101 nm. This part is shown since the initial value for the defocus is around -92 nm, as determined from the diffractogramm. For $\Delta f = -92$ nm, the atomic columns of Ti correspond to the highest intensity spots. However, the atomic column positions might change due to a reverse of the contrast. For example, for images calculated for $\Delta f = -32$ nm, which are not shown in Figure 7.8, the Sr atomic column positions coincide with the highest intensity spots. A similar effect was found for the Pd thickness/defocus map (Fig. 7.8), with the difference that the same intensity pattern is repeated every 15 nm. This can lead to misinterpretation of the structure and to mistakes in the determination of the $\mathbf{T}_3$ value.

As described above, the TiO_2 terminated models (Fig. 7.6a and b) cannot be distinguished in $\langle 100 \rangle_{STO}$ projection. The same is true for the SrO terminated models (Fig. 7.6c and d). Therefore, only one model of each termination was chosen for the simulations of HRTEM images in order to determine the position of the interface.

The TiO_2/Pd-O and SrO/Pd-gap models were used for the simulation. The determined initial parameters were applied. The best fit between the simulated and experimental images

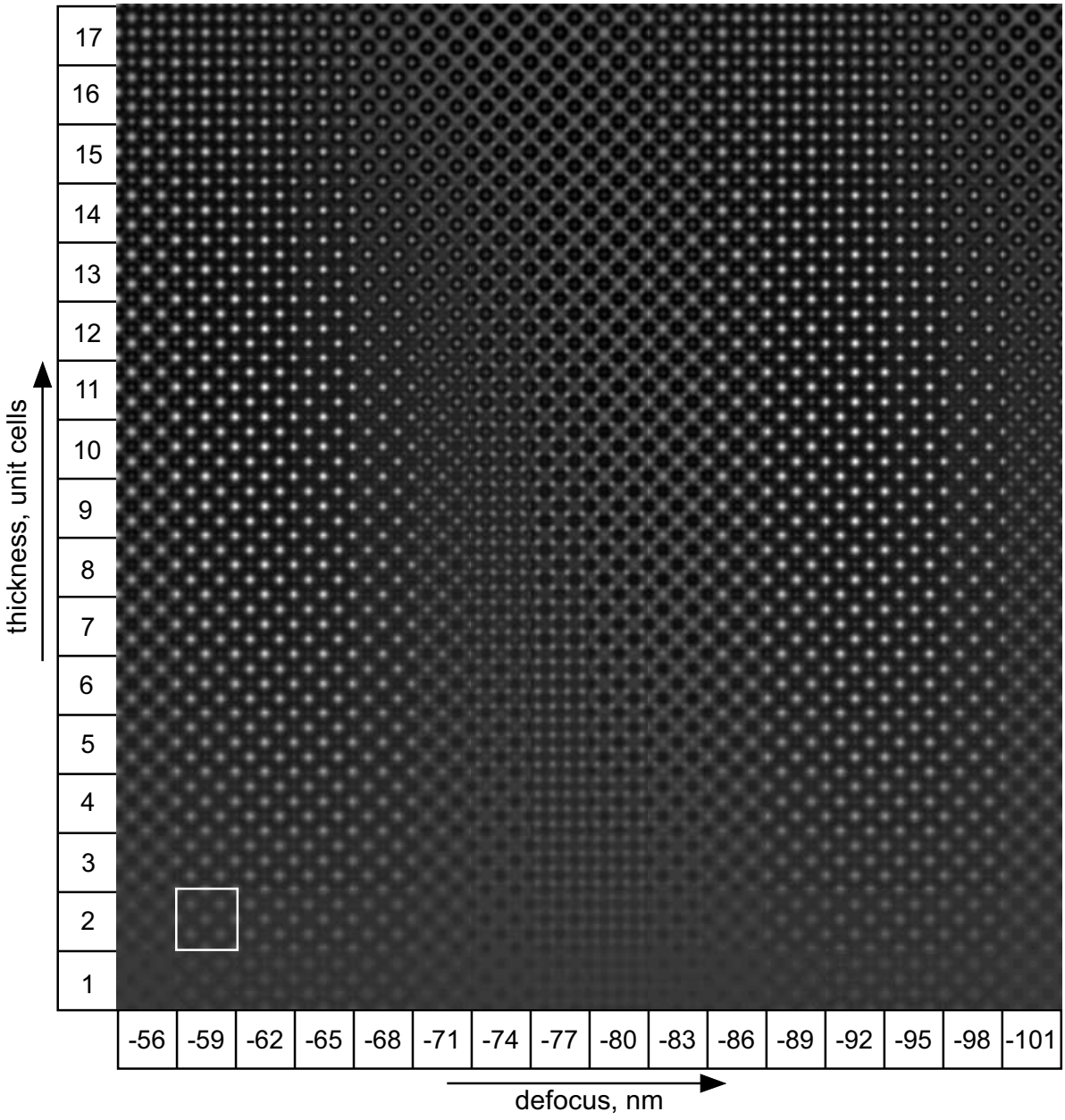

Figure 7.7: Thickness/defocus map calculated for the $SrTiO_3$ bulk cell viewed in $\langle 100 \rangle$ direction, the cell is marked by the white square. Similar intensity patterns occur for defocus values which differ by 30 nm, such as -62 nm and -92 nm.

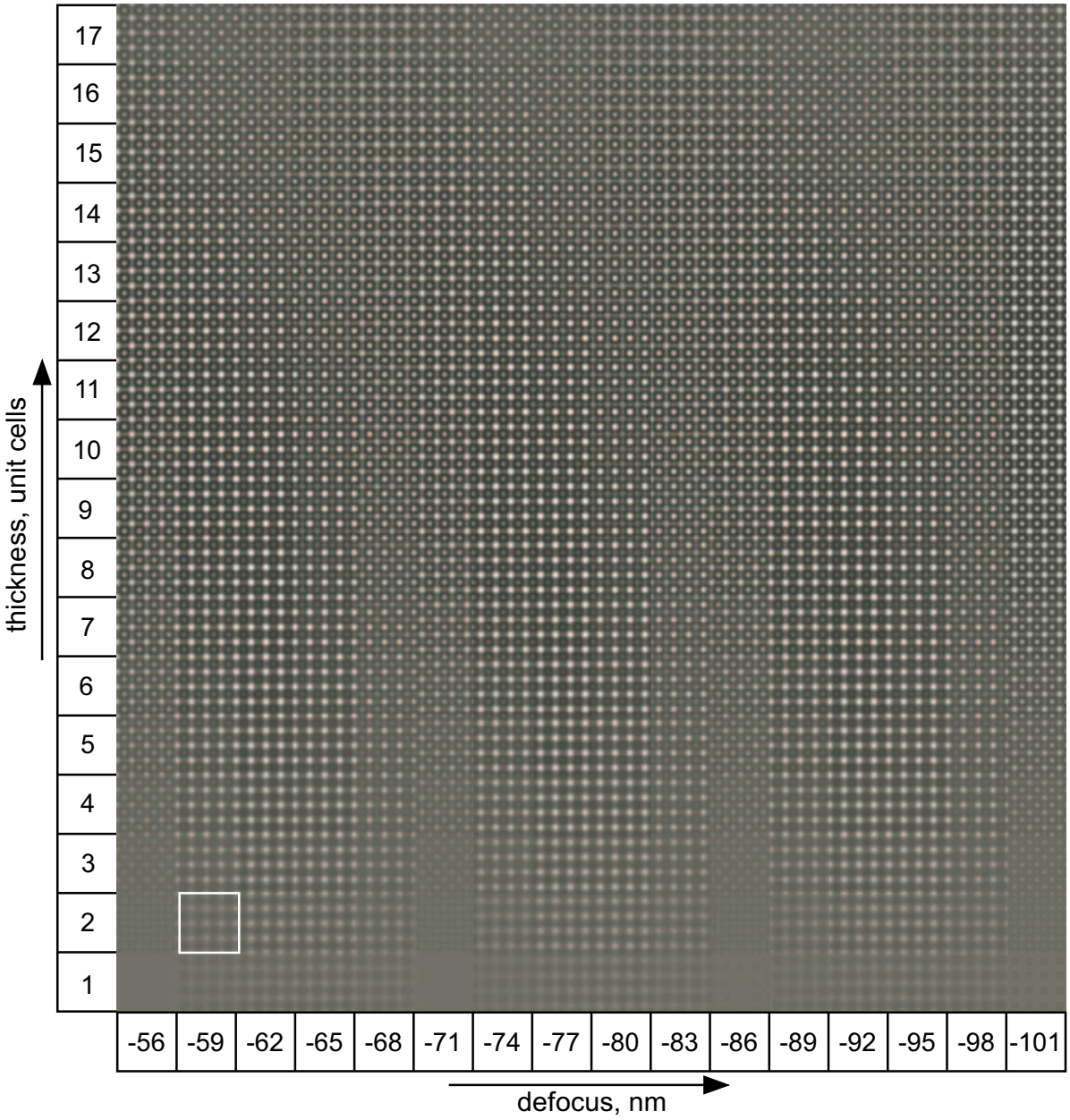

Figure 7.8: Thickness/defocus map calculated for the Pd bulk cell viewed in ⟨100⟩ direction, the cell is marked by the white square. Similar intensity patterns occur here for defocus values with differences of 15 nm, such as −59 nm, −74 nm and −89 nm.

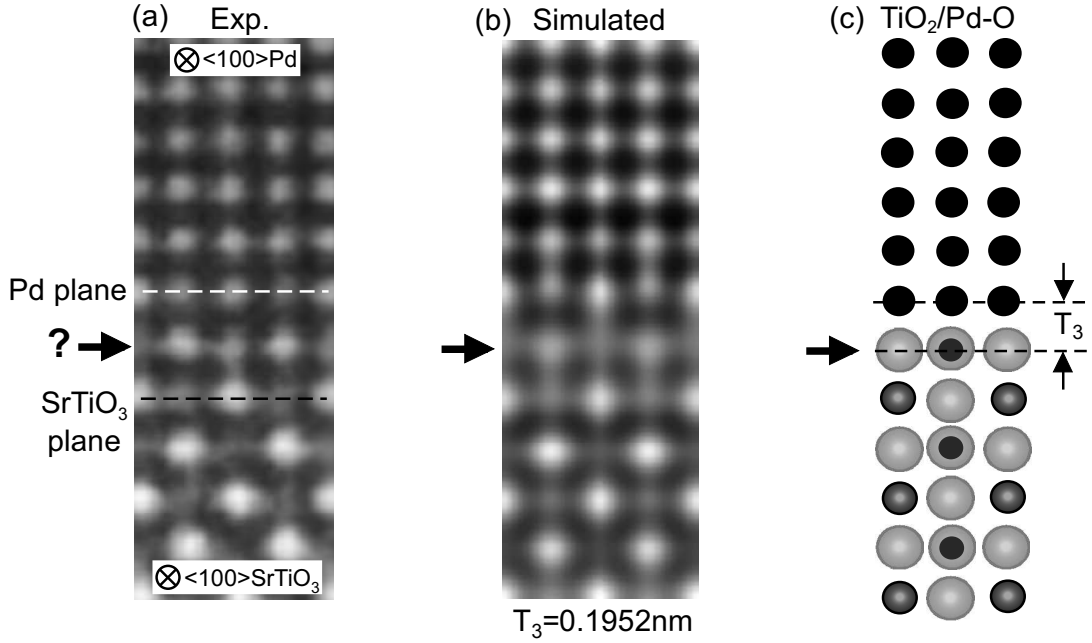

Figure 7.9: Determination of the interface position in the HRTEM image of $Pd/SrTiO_3$ viewed in $\langle 100 \rangle_{STO}$ direction: (a) experimental image of the $Pd/SrTiO_3$ interface region, (b) simulated image with a translation distance of 0.1952 nm at the interface, and (c)TiO_2/Pd-O structure model used for the simulation. The plane of interest is indicated by arrows.

of the bulk Pd and $SrTiO_3$ was obtained at a thickness of 1.2 nm and a defocus of −92 nm. No other parameters were varied during the simulations. Both models, however, gave the same intensity pattern and the same value of the cross-correlation factor XCF = 0.967 (see Subsection 7.2.3). Therefore, only one simulated image obtained by using the TiO_2/Pd-O interface model is shown in Figure 7.9. In addition, the experimental HRTEM micrograph together with the simulated image and the TiO_2/Pd-O model are presented (Fig. 7.9). The plane that has to be identified is marked by arrows. The superposition of the simulated image (Fig. 7.9b) with the structure model (Fig. 7.9c) showed, that the plane of interest belongs to $SrTiO_3$.

Translation state at the Pd/$SrTiO_3$ interface

After the interface position in the experimental HRTEM image was determined, the calculation of the $\mathbf{T}_3$ component of the translation vector was performed following the procedure described in Section 4.2.3 (see also Fig. 4.10 and 4.11). 80 different unit cell templates of Pd and $SrTiO_3$ were used for the calculation of cross-correlation maps and the determination of $\mathbf{T}_3$. The origins of the basis vectors were chosen in the central part of the image in an undistorted area. The distance between the origins and the value of $\mathbf{T}_3$ were calculated using equations 4.9, 4.10, and 4.11.

Due to slight inclination of the Pd lattice (see Fig. 7.3), the origins of the Pd and $SrTiO_3$ do not longer have the same value of the x coordinate. This means that the distance D, which connects the origins, is no longer perpendicular to the interface plane. The interface plane, in its turn, might also be not parallel to the x axis of the image cartesian coordinates. Due to these reasons, the calculation of D and $\mathbf{T}_3$ were performed within the cartesian coordinates of the determined basis vectors $\mathbf{a}$ and $\mathbf{b}$. This allows to achieve higher precision of the calculated values of $\mathbf{T}_3$ and to overcome possible misalignments of the HRTEM image during the digitalization process of the negatives.

The $\mathbf{T}_3$ values resulting from 80 calculation iterations are presented in Figure 7.10. The average value of $\mathbf{T}_3$ is 0.254 nm with the standard deviation of 0.005 nm:

$$\mathbf{T}_3 = 0.254 \pm 0.005 \text{ nm}. \tag{7.1}$$

Errors that occur during the determination of the translation vector component T_3 arise from (i) the choice of the Pd and $SrTiO_3$ templates, (ii) determination of basis vectors for Pd and $SrTiO_3$ fitted 2-dimensional lattices and (iii) determination of the origins of basis vectors (one per calculation).

The errors that occur due to the choice of Pd and $SrTiO_3$ templates are accommodated by a large number of calculations performed with different templates. Deviations in the determination of the origins of the fitted lattices for Pd and $SrTiO_3$ depend strongly on the quality of the HRTEM image. Imperfections in the image contrast pattern reflect the positions of the local intensity maxima in the calculated cross-correlation maps. For 80 performed calculations of $\mathbf{T}_3$ with different Pd and $SrTiO_3$ templates, the standard deviation

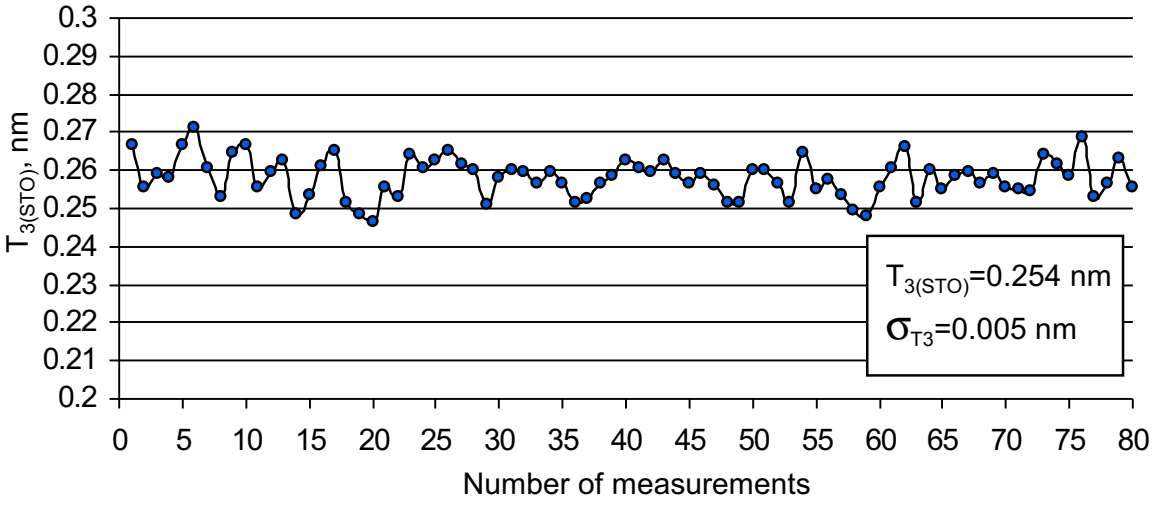

Figure 7.10: Plot of the calculated values for the $\mathbf{T}_3$ translation vector component versus the number of calculations.

of the fitted position of the origins lies in the range of $\sigma_{STO-origin} = \pm 3.9$ pm for the $SrTiO_3$ origin and $\sigma_{Pd-origin} = \pm 4.1$ pm for the Pd origin. The errors obtained for the determination of the basis vectors are $\sigma_{basis} < \pm 0.6$ pm. These two types of errors are incorporated into the final error of the translation vector components through averaging over 80 calculation iterations. Therefore, the final value of the $\mathbf{T}_3$ translation vector component including the calculation errors can be described by Equation 7.1.

The procedure used for the determination of $\mathbf{T}_3$ assumes that there are no lattice distortions or relaxations at the interface, since the basis vectors lengths used for the calculation have values equal to the rigid bulk lattice constant.

7.2.3 Determination of the Atomic Structure of the Interface

A goal of performing the QHRTEM was to determine the terminating plane of the $SrTiO_3$ substrate and to define the positions of the Pd atoms on top of the atoms forming this plane.

Although the Pd atoms positioned on top of the TiO_2 or SrO terminated $(100)_{STO}$ surfaces are undistinguishable for the $\langle 100 \rangle_{STO}$ projection (see Section 7.2.1), it is possible to distinguish between the TiO_2 and SrO terminated interface models in this projection. TiO_2 and SrO structure models with the determined translation state at the interface of $\mathbf{T}_3 = 0.254$ nm (see Section 7.2.2) were used for image simulation and digital image comparison by means

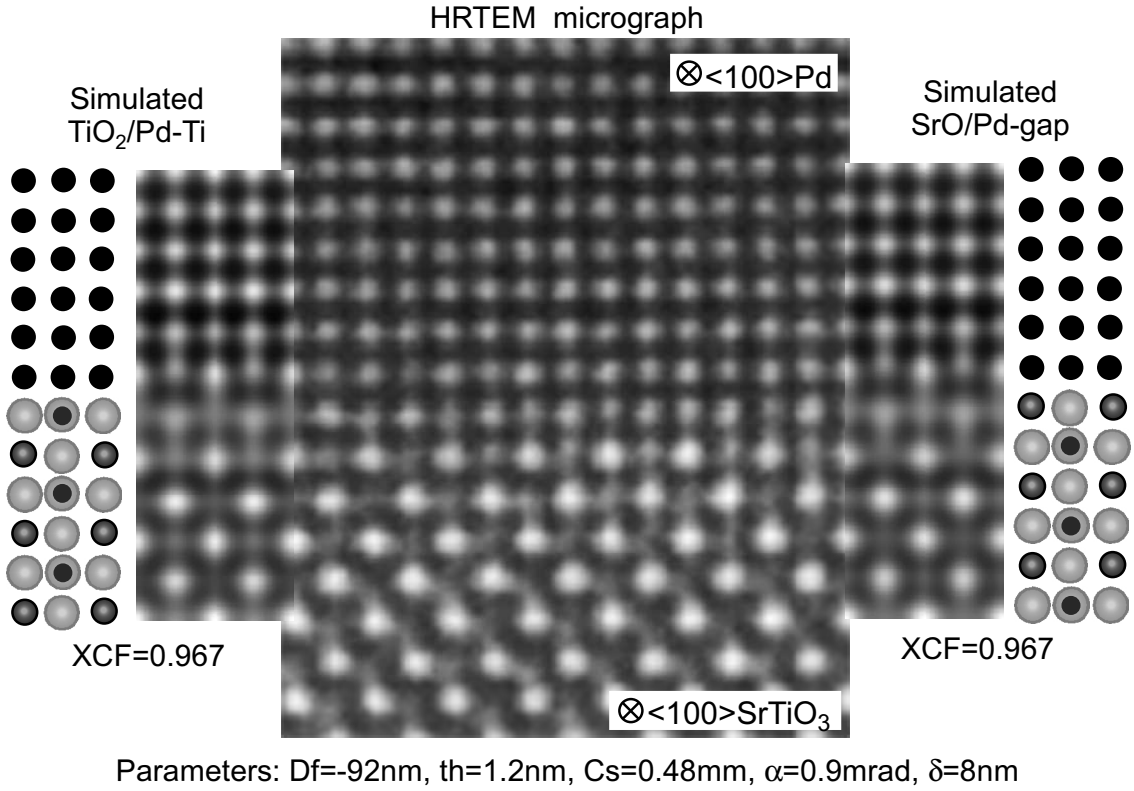

Figure 7.11: Comparison between the experimental HRTEM micrograph of the Pd/$SrTiO_3$ interface viewed in $\langle 100 \rangle_{STO}$ direction and the simulated images, which were obtained by using two different structure models with TiO_2 and SrO terminations, respectively.

of the cross-correlation function (see Section 4.2.3). As can be seen in Figure 7.11, the intensity patterns of both simulated images do not differ significantly. The XCF for both models is identical (XCF = 0.967). Therefore, the $\langle 100 \rangle_{STO}$ projection cannot be used to distinguish the terminating planes of $SrTiO_3$.

For that reason, the $\langle 110 \rangle_{STO}$ projection of the interface was analyzed and four structure models were build with regard to the obtained value of the T_3 interfacial translation state. Figure 7.12 represents all four models of the Pd/$SrTiO_3$ interface in $\langle 110 \rangle_{STO}$ projection together with the corresponding simulated images.

Prior to the simulations, the initial parameters of defocus and specimen thickness were obtained by the methods described in Section 4.2.3. The defocus value was estimated to be +35 nm and the nominal thickness was calculated to be 4 unit cells ($\sim$ 2.2 nm). Only one region of thickness/defocus values in the calculated maps for Pd and $SrTiO_3$ are close to

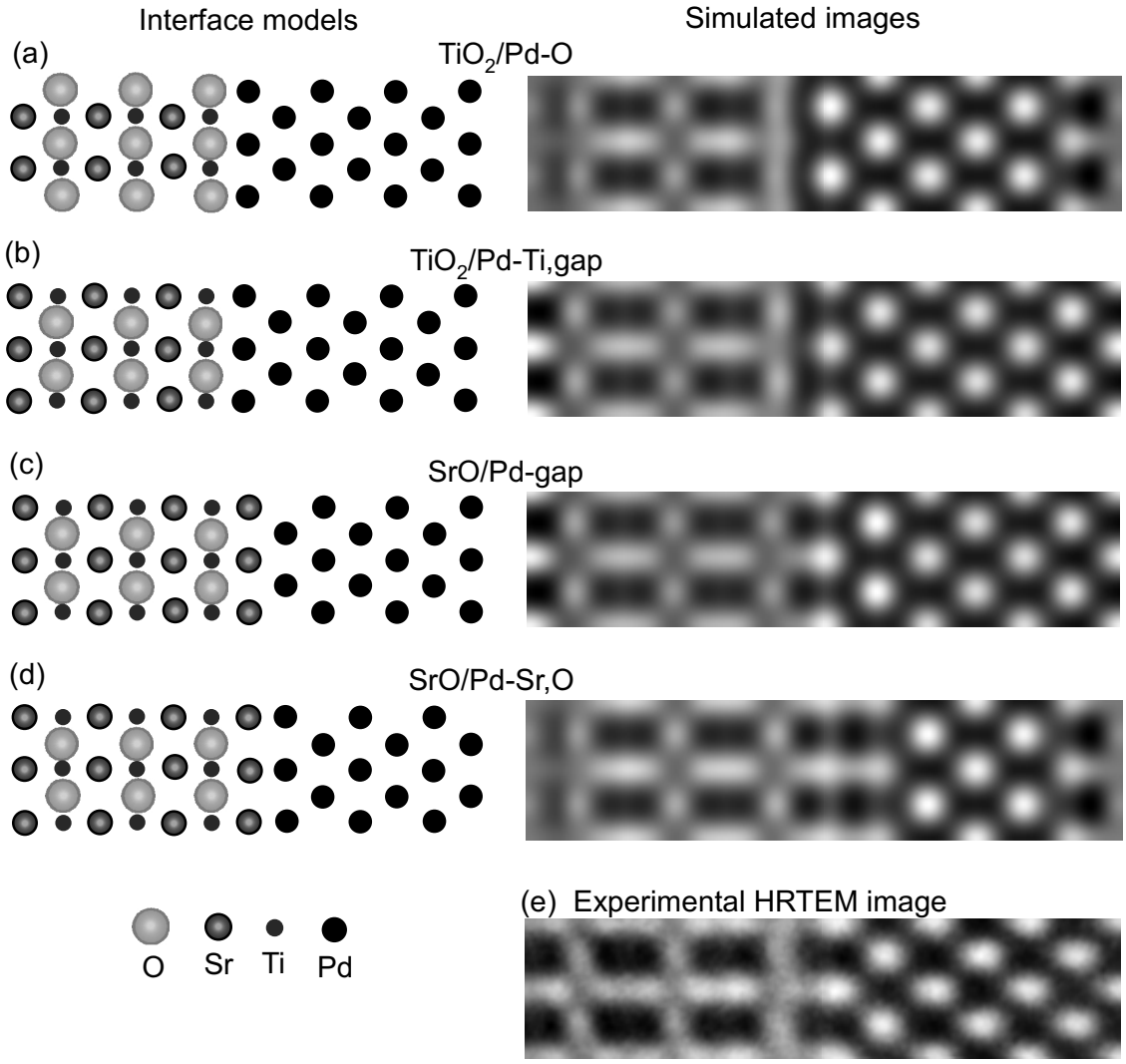

Figure 7.12: Sketch of the four possible structure models of $Pd/SrTiO_3$ interface in $\langle 110 \rangle$ projection together with the corresponding simulated images: (a) TiO_2 termination with Pd positioned on top of O atoms, (b) TiO_2 termination with Pd positioned in top of the Ti atoms and above the hollow sites, (c) SrO termination with Pd positioned above the hollow sites, (d) SrO termination with Pd positioned on top of the Sr and O atoms, and (e) experimental HRTEM image.

these values.

Figures 7.13 and 7.14 show the calculated thickness/defocus maps. The regions of similar contrast pattern for bulk $SrTiO_3$, which match the experimental pattern, lie in the range of +32 to +48 nm for the defocus value and 2 to 10 unit cells thickness. The Pd map shows a similar tendency. However, since the Pd structure is less complex compared to $SrTiO_3$, the

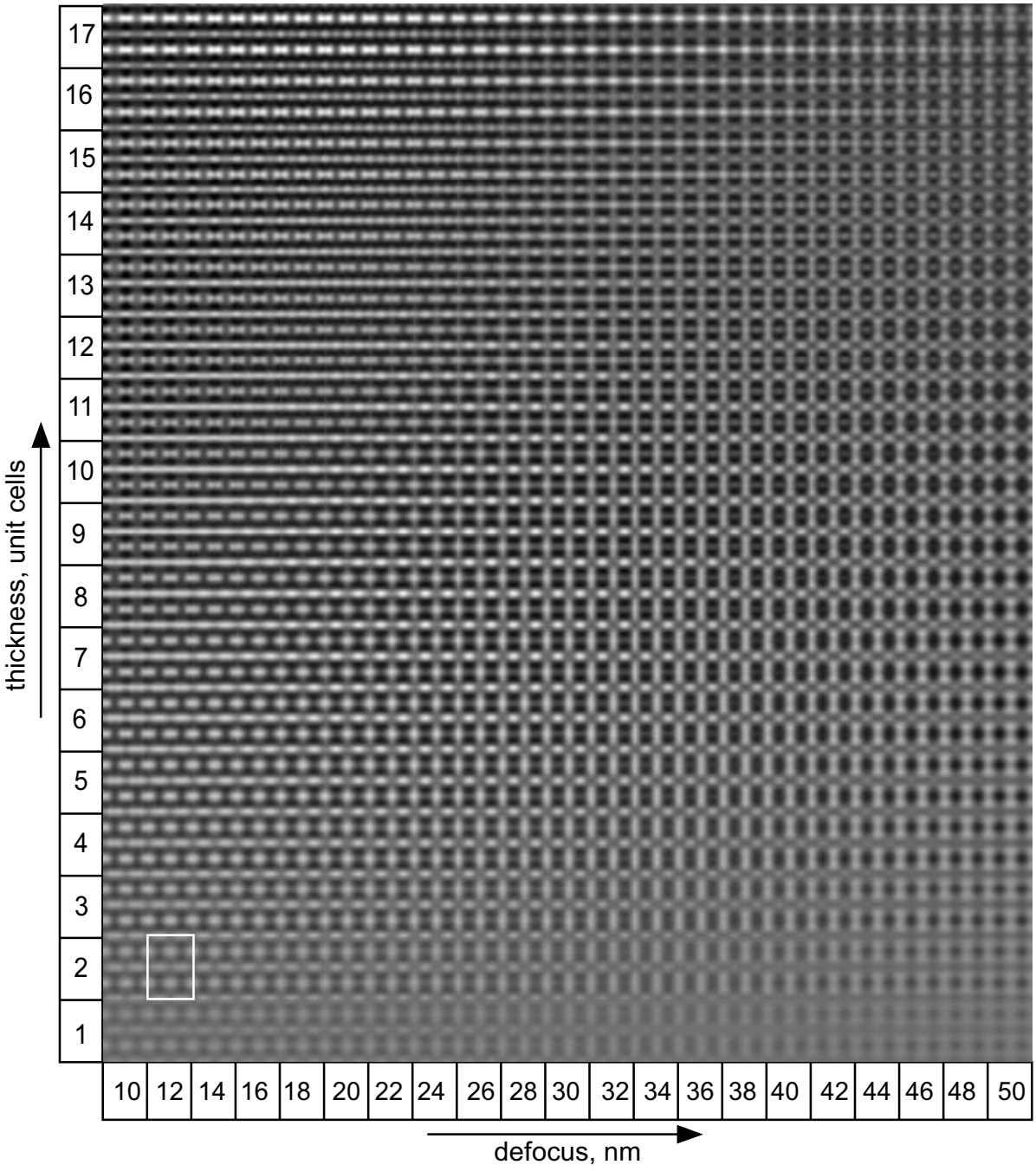

Figure 7.13: Thickness/defocus map calculated for the $SrTiO_3$ bulk cell viewed in $\langle 110 \rangle$ direction, the cell is marked by the white square.

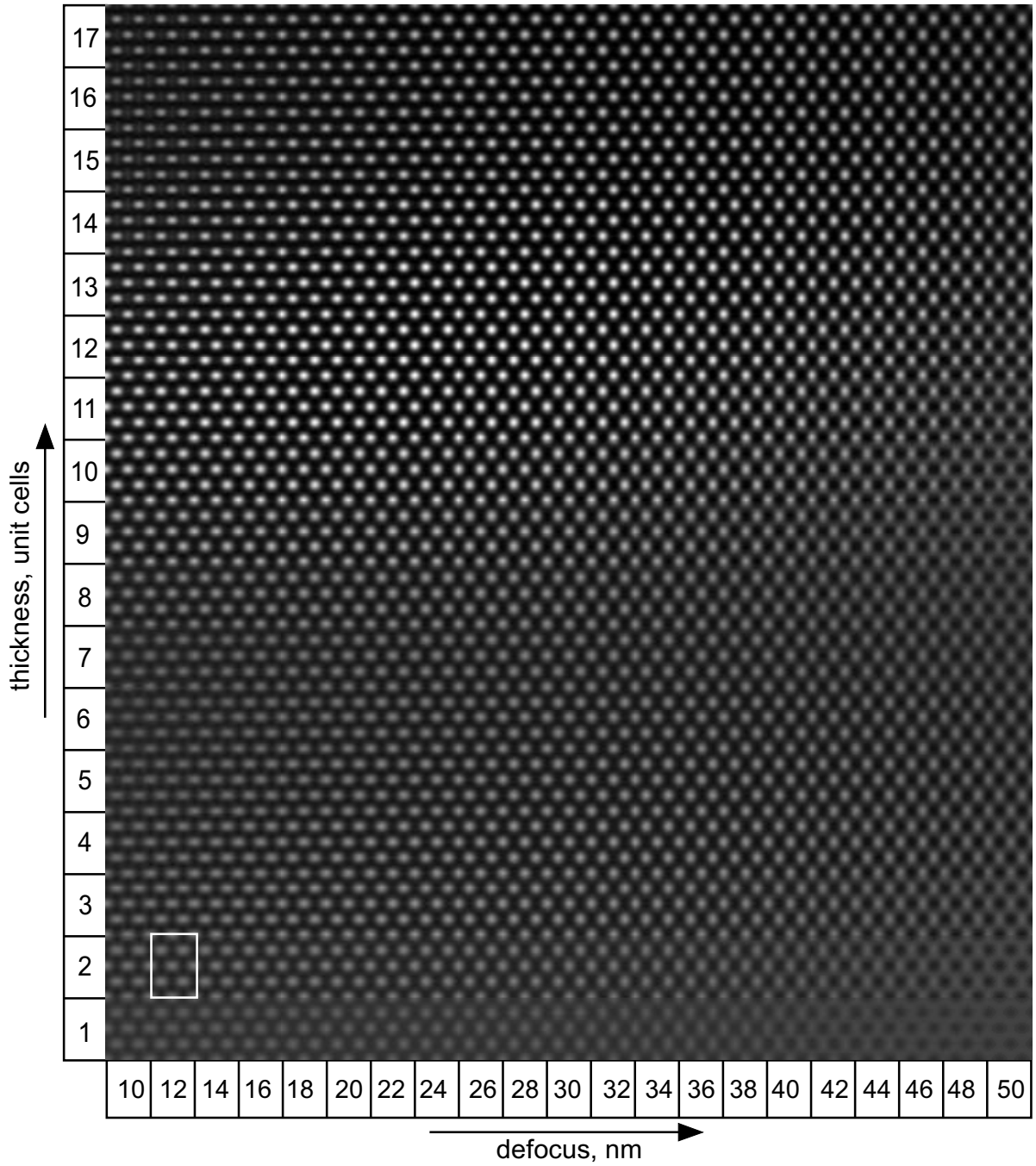

Figure 7.14: Thickness/defocus map calculated for the Pd bulk cell viewed in ⟨110⟩ direction, the cell is marked by the white square.

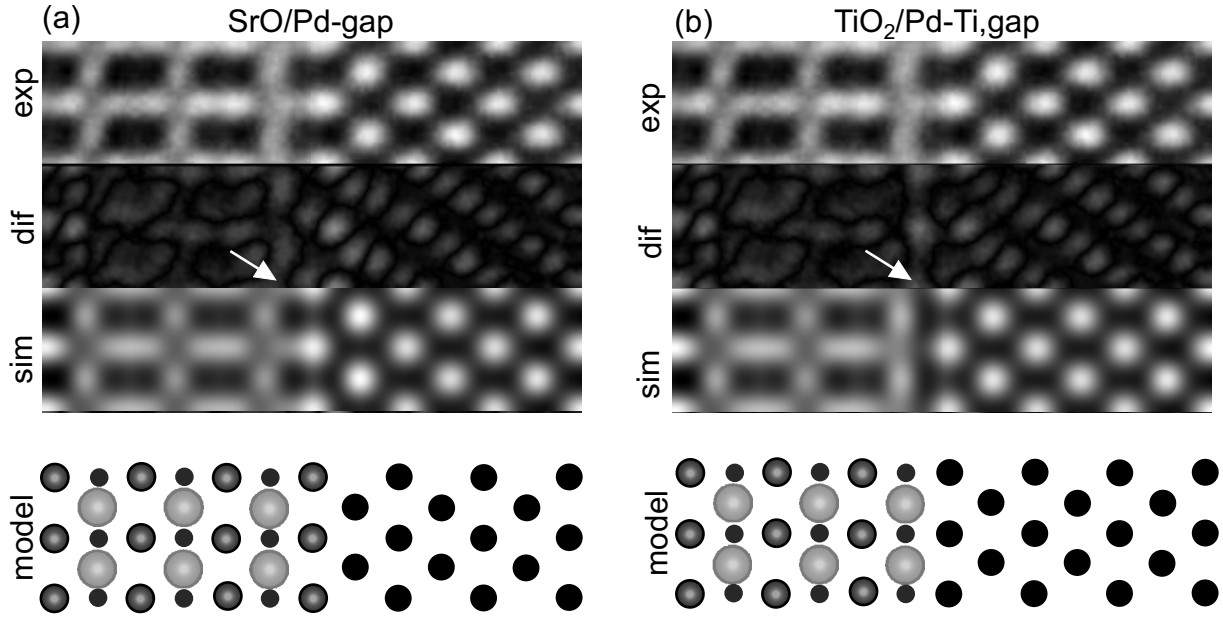

Figure 7.15: Calculated difference image between the experimental micrograph and simulated images of different structure models: (a) SrO/Pd-gap, and (b) TiO_2/Pd-Ti,gap.

simulation parameters of the best fit for the bulk $SrTiO_3$ lattice are considered for further simulations in order to resolve the fine details observed in the experimental image.

The images shown in Figure 7.12 were calculated for the same set of parameters, received through the iterative simulation procedure for bulk $SrTiO_3$. The final cross-correlation obtained for the bulk was XCF=0.96. The contrast observed in the simulated image obtained by using TiO_2/Pd-O (Fig. 7.12a) and SrO/Pd-Sr,O (Fig. 7.12d) structure models does not correspond to the contrast observed in the experimental image (Fig. 7.12e). Specifically, there are no bright connections, or "bridges", in the simulated image obtained by using the TiO_2/Pd-O interface model in comparison to the experimental image (Fig. 7.12a,e). For the SrO/Pd-Sr,O model (Fig. 7.12d), this contrast features are doubled. Variation of the simulation parameters within the determined ranges did not change significantly the contrast pattern at the interface for these models. Therefore, they could be excluded.

The contrast patterns calculated by using the TiO_2/Pd-Ti,gap (Fig. 7.12b) and SrO/Pd-gap (Fig. 7.12c) models show the presence of the bridges, having much higher intensities for the SrO/Pd-gap model compared to the TiO_2/Pd-Ti,gap model. These two latter structure models were considered for further iterative simulations performed by means of the IDIM

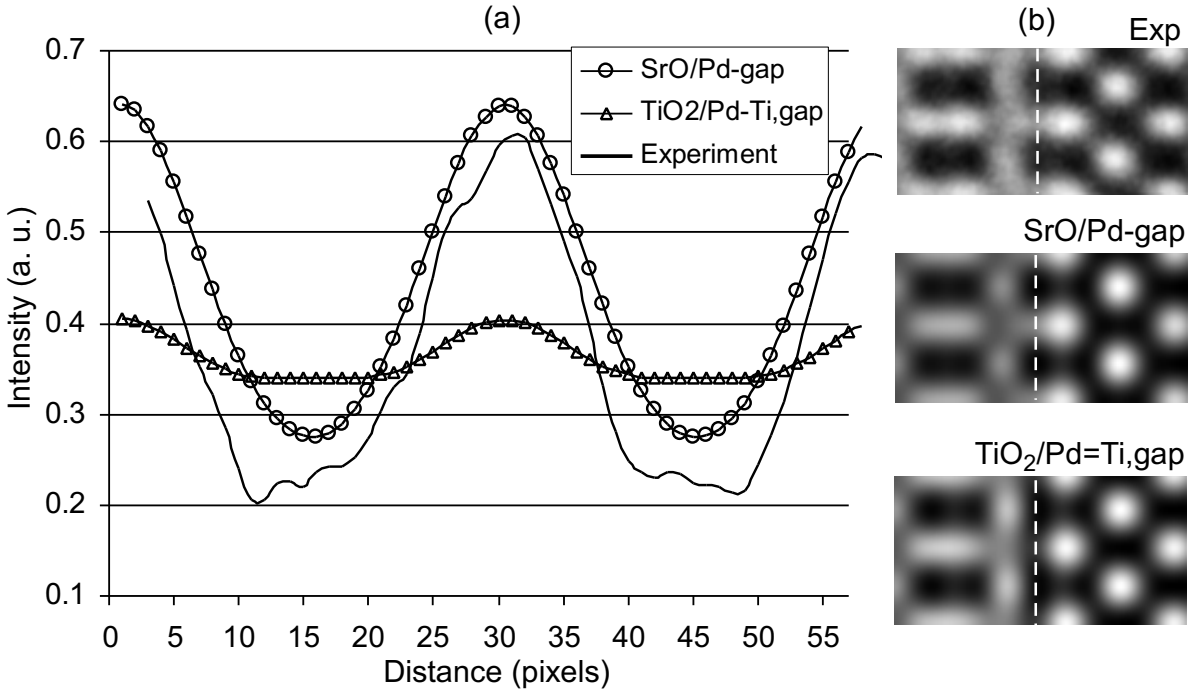

Figure 7.16: Line scan of the intensity profile along the interface for two simulated images obtained by using the SrO/Pd-gap and TiO_2/Pd-Ti,gap structure models used to simulate the image and the experimental HRTEM micrograph. The line scans were obtained from the region marked by the dashed lines.

programm package [Moebus1994]. Figure 7.15 shows the results for the digital comparison of the experimental HRTEM image with the simulated images of both considered structure models. The difference map in both cases has a similar intensity pattern. However, at the interfacial region with the bridge structure, which is marked by the arrows, the difference intensity is higher for the TiO_2/Pd-Ti,gap model (Fig. 7.15b). As can be seen in Figure 7.15, this bridge structure is well pronounced in the images simulated using the SrO/Pd-gap model and almost invisible in the images simulated using the TiO_2/Pd-Ti,gap model. Furthermore, the interfacial spots shapes and intensities between the experimental image and simulated images are compared. In case of the image calculated using the SrO/Pd-gap model (Fig. 7.15a) the shape of the spots fits well to the features at the interface in the experimental image, which has a slightly elongated shape. For the TiO_2/Pd-Ti,gap model (Fig. 7.15b), the shape of the spots is circular.

In order to quantify these results, line scans were performed along a line parallel to the

interface (see Fig. 7.16b). As can be seen in the plot of the measured intensity versus pixel position along the interface (Fig. 7.16a), the curve belonging to the SrO/Pd-gap model is almost parallel to the curve belonging to the experimental image and has a similar shape. The profile representing the TiO_2/Pd-Ti,gap model has much less intensity fluctuations. This result suggests that the structure of the Pd/$SrTiO_3$ interface can be described with the SrO/Pd-gap structure model.

7.3 Discussion

7.3.1 Translation State at the Pd/$SrTiO_3$ Interface

The determination of the translation state at the interface between Pd and $SrTiO_3$ was performed using the method described in Section 4.2.3. For this method, it is essential that no lattice distortions and no thickness variations across the investigated area are present in the experimental HRTEM micrograph. Only HRTEM images taken in the $\langle 100 \rangle_{STO}$ zone axis possessed the desired quality, i.e. areas of homogeneous contrast were large enough. In the images taken in $\langle 110 \rangle_{STO}$ zone axis the bright contrast spots corresponding to the Pd atoms become elongated within the first layers of Pd owing to a small thickness of the TEM specimen and possible bending of this very thin region of the film. Due to the elongations of the spots, the fitted 2D lattice of Pd becomes distorted (see Section 4.2.3), which leads to an increase of the error bars. Therefore, images taken in $\langle 110 \rangle_{STO}$ zone axis could not be used for the determination of the translation state.

However, even for the HRTEM image taken in $\langle 100 \rangle_{STO}$ zone axis some small lattice distortions exist, for example a slight buckling and inclination of the Pd lattice (Fig. 7.2a, Fig. 7.3). The presence of such features is observed in very thin areas of the TEM specimens, i.e. where most part of the Pd islands was already milled away, or at the thin edges of the whole Pd islands. They are most likely generated during the Ar^+-ion milling procedure at the final stage of the TEM specimen preparation. This source of possible analysis errors was overcome by choosing positions of the Pd and $SrTiO_3$ basis vectors origins in the central part of the HRTEM image, which had no distortions.

Theoretical values of the translation vector component $\mathbf{T}_3$ at the Pd/$SrTiO_3$ interface

were previously determined in the work of Ochs *et al.* [Ochs2000] by performing *ab initio* calculations. Four energetically metastable structure models were considered by Ochs *et al.* [Ochs2000]. All the theoretical values of $\mathbf{T}_3$ were calculated using a relaxed $SrTiO_3$ structure. In this structure, the first 3 planes of $SrTiO_3$ next to the interface plane are shifted inwards. The displacement of the atoms from their rigid positions decreases as the distance from the interface increases. The method used in the present work for the retrieve of the translation vector component $\mathbf{T}_3$ did not account such relaxations. However, it was shown in the theoretical calculations that for Pd films with 3 ML thickness, the relaxation of the $SrTiO_3$ surface decreases compared to the relaxation calculated for 1 ML of Pd [Ochs2000]. In the present thesis, Pd films had significantly higher thicknesses (the nominal thickness was 50 nm). Therefore, in the first approximation, $\mathbf{T}_3$ values obtained by assuming a rigid structure of the $SrTiO_3$ (see Section 4.2.3 for the method and Section 7.2.2 for the results) can be compared to the theoretical values.

Table 7.1: Values of the translation vector component $\mathbf{T}_3$ calculated *ab initio* for 3 ML of Pd on top of TiO_2 and SrO terminated (100)$SrTiO_3$ [Ochs2000] and the value obtained by the HRTEM image processing.

Structure	Theoretical value, Å relaxed $SrTiO_3$ surface	Experimental value, Å
TiO_2/Pd-O	2.13	
TiO_2/Pd-Ti,gap	2.48	2.54 ± 0.05
SrO/Pd-gap	2.51	
SrO/Pd-Sr,O	2.76	

The theoretical values of $\mathbf{T}_3$ represent the distances between the projected positions of metal atoms of the given TiO_2 or SrO terminations and Pd atoms. Table 7.1 summarizes the $\mathbf{T}_3$ values for the different models, obtained theoretically and through the analysis of the experimental data.

As can be seen from the numbers in Table 7.1, the best agreement between the experimental results and the calculated values of $\mathbf{T}_3$ are given for the SrO/Pd-gap and the TiO_2/Pd-Ti,gap structure models. The differences between $\mathbf{T}_{3\,(theory)}$ and $\mathbf{T}_{3\,(exp)}$ are $\Delta\mathbf{T}_3 = 2$ pm and

$\Delta\mathbf{T}_3 = 6$ pm for the SrO/Pd-gap and the TiO_2/Pd-Ti,gap structure models, respectively. These lie in the range of the standard deviation $\sigma_{T\,3\,(exp)}$ of the experimentally obtained value. For both other models, TiO_2/Pd-O and SrO/Pd-Sr,O, the difference between theoretical and calculated values is exceeding the standard deviation.

7.3.2 Atomic Structure at the Pd/$SrTiO_3$ Interface

The investigations of the atomic structure at the Pd/$SrTiO_3$ interface, including the determination of the terminating layer of $SrTiO_3$ and the positioning of the Pd atoms on top of the atoms of this layer, could only be performed for the $\langle 110 \rangle$ projection of the interface. For the $\langle 100 \rangle_{STO}$ zone axis, a similar contrast pattern is obtained for all four considered structure models.

For the quantitative image simulations of the Pd/$SrTiO_3$ interface, a compromise in choosing the initial parameters for simulation had to be made. Due to the more complex structure of $SrTiO_3$, the fine structure details in the experimental image are resolved only for limited variations of the imaging parameters such as thickness, defocus and electron beam convergence. Introduction of more parameters such as beam tilt, specimen tilt or astigmatism was leading to significant deviations from the experimentally determined thickness and defocus values. Therefore, only thickness, defocus and beam convergence were subjected to iterative increment. The estimated thickness is 2 nm, which is rather small. However, the underestimation of specimen thicknesses by HRTEM image analysis was described before in a study of O'Keefe *et al.* [O'Keefe1994].

In order to obtain the best fit between simulated bulk $SrTiO_3$ images with the experimental ones, the cross-correlation function (see Section 4.2.3) was successfully used. Nevertheless, it could not be applied for comparison between the simulated and experimental images of the Pd/$SrTiO_3$ interface. The reason for that is the presence of contrast imperfections in the HRTEM micrograph, i.e. the elongation of the intensity spots on the Pd side. During the cross-correlation procedure, the contribution of these spots to the XCF is much higher than the contribution of the small interfacial features. This led to the reduction of the overall XCF value, although the contrast difference map showed a good match with low residual intensity at the interface region (see Fig. 7.16). Therefore, a comparison of the experimental

and simulated images was accomplished by the detailed evaluation of the intensity features as well as of the difference map at the region near the interface.

Detailed theoretical investigations of the projected bonding distance, bonding behavior and energetics of the $Pd/SrTiO_3$ interface were performed by Ochs *et al.* [Ochs2000] using *ab initio* calculations. Table 7.2 summarizes the results of the calculated cohesion energy, work of separation and translation state at the interface for four relaxed structure models.

Table 7.2: Cohesion energies and work of separation calculated using *ab initio* methods for 3 ML of Pd on top of relaxed TiO_2 and SrO terminated (100)$SrTiO_3$ [Ochs2000].

Structure	TiO_2/Pd-O	TiO_2/Pd-Ti,gap	SrO/Pd-gap	SrO/Pd-Sr,O
Cohesion energy, eV	-3.86	-3.70	-3.69	-3.76
Work of separation, J/m^2	1.87	0.84	0.77	1.22

Comparison of the work of separation and cohesion energy values for different adsorption sites of the two terminations of $SrTiO_3$ led to the conclusions that (i) the Pd atoms should be placed on top of O atoms, and (ii) the TiO_2 termination is energetically favorable due to the possibility of arranging all Pd atoms of the unit cell at the energetically favorable O adsorption sites [Ochs2000]. For the SrO termination, strong interactions between Pd and O were observed, while the Sr interacts only weakly with O ions. This lead to a shift of the Sr atoms into the substrate interior when the Pd was placed on the hollow sites between two O and two Sr atoms [Ochs2000]. No pronounced bonds between the Pd and the substrate were detected in this case. For TiO_2/Pd-Ti,gap and SrO/Pd-Sr,O models, the positioning of Pd on two different adsorption sites was found to result in strong Pd buckling [Ochs2000].

Van Benthem [Benthem2002] analyzed the bonding across the $Pd/SrTiO_3$ interface by EELS and ELNES techniques. The best agreement between the experimental ELNES data and the calculated projected density of states was found for the case, where the $SrTiO_3$ is TiO_2 terminated. Strong Pd-O bonds and some weak Pd-Ti bonds were detected by Van Benthem [Benthem2002]. This is in agreement with the results of Ochs *et al.* [Ochs2000].

In the present work, image simulations were performed for all four structure models. The simulated images were compared to the HRTEM micrographs. Surprisingly, the simulated

image of TiO_2/Pd-O structure model revealed a contrast pattern at the interface that was significantly different from the pattern of the experimental image (see Fig. 7.12). Images simulated using the TiO_2/Pd-Ti,gap and SrO/Pd-gap models showed the best agreement with the details of the experimental contrast pattern.

The results obtained by the Z-contrast (HAADF) imaging technique were also not able to clarify the question of the $SrTiO_3$ termination. Instead, features that fit into two differently terminating models, namely SrO/Pd-gap and TiO_2/Pd-Ti,gap, were observed in the same experimental image. Even though the quality of the Z-contrast images has to be improved in order to perform quantitative image simulation analysis, the obtained image clearly shows a step in the center of the image, after which differently terminated structure models can be fitted into the contrast pattern (Fig. 7.4).

Since the $SrTiO_3$ substrates were prepared by the preparation method of Kawasaki et al. [Kawasaki1994], the substrate termination is expected to consist of 100% TiO_2 [Kawasaki1994]. However, there was no possibility to perform an ion-scattering analysis on the $SrTiO_3$ substrates prior to the Pd deposition in order to prove the gained surface termination. Therefore, the areas where the HRTEM images were taken might possibly have the SrO termination.

7.3.3 Conclusions

The present study has demonstrated that the atomic structure of the Pd/$SrTiO_3$ interface cannot be easily determined even by the combination of different investigation techniques. The TEM specimen preparation plays an important, most likely a controlling role for a high-quality quantitative HRTEM evaluation.

The Pd/$SrTiO_3$ interface was found to be atomically abrupt. As expected, misfit dislocations were not detected in the regions investigated by HRTEM. Steps of one $SrTiO_3$ unit cell height were observed in some regions of the HRTEM images, which means that the termination of the substrate is the same along the interface. The translation state $\mathbf{T}_3$ at the interface corresponds to the theoretical value of the TiO_2/Pd-Ti,gap and SrO/Pd-gap structure models, which should be according to the *ab initio* calculations [Ochs2000] not energetically favorable. Nevertheless, the best match of the contrast patterns between simulated and experimental HRTEM images at the interfacial region, taken in $\langle 110 \rangle_{STO}$ projection,

was found for the SrO/Pd-gap structure model. HAADF imaging, performed at the same interface in the same projection, revealed the possibility that two differently terminated interfacial configurations are present. These correspond to the SrO/Pd-gap and TiO_2/Pd-Ti,gap structure models.

In order to solve the atomic structure of the Pd/$SrTiO_3$ interface, a better quality of the HRTEM images is required. Performing further image simulations using structure models with relaxed atomic positions at the interface might improve the reliability of the determined atomic interfacial configuration. Finally, better quality of HAADF images and, therefore, the possibility of their quantitative analysis through the performance of HAADF image simulations can give an additional information about the chemical structure of the interface.

Appendix A

NCSL Model Calculations

In order to calculate the possible configurations of the NCSL formed by positioning the $(110)_{Mo}$ plane on top of the $(100)_{STO}$ plane, the initial setup schematically drawn in Figure A.1 was used. Here, the components of the translation vector $\mathbf{T}_s$ are vectors $\mathbf{b}_1$ and $\mathbf{b}_2$, lying on the $\langle 110 \rangle_{STO}$ directions, while the components of translation vector $\mathbf{T}_f$ are vectors $\mathbf{a}_1$ and $\mathbf{a}_2$, lying on the $\langle 111 \rangle_{Mo}$ directions (Fig.A.1). The coordinates of the basis vectors were used as an input for the calculation, and the $\mathbf{T}_s$ and $\mathbf{T}_f$ were calculated as

$$\mathbf{T}_f = k\mathbf{a}_1 + l\mathbf{a}_2, \tag{A.1}$$

$$\mathbf{T}_s = m\mathbf{b}_1 + n\mathbf{b}_2, \tag{A.2}$$

were the range of integers k, l, m and n could be arbitrary chosen. The degree of coincidence σ was then calculated as

$$\sigma_{Mo} = \mathrm{k}^2 + \mathrm{l}^2 \tag{A.3}$$

$$\sigma_{STO} = \mathrm{m}^2 + \mathrm{n}^2. \tag{A.4}$$

The coincidence was set to be achieved when

$$|\ \mathbf{T}_s| = |\ \mathbf{T}_f|, \tag{A.5}$$

with the error of coincidence due to the different lattice constants of Mo and $SrTiO_3$

$$\delta = \frac{2(\mathbf{T}_{Mo} - \mathbf{T}_{STO})}{\mathbf{T}_{Mo} + \mathbf{T}_{STO}}. \tag{A.6}$$

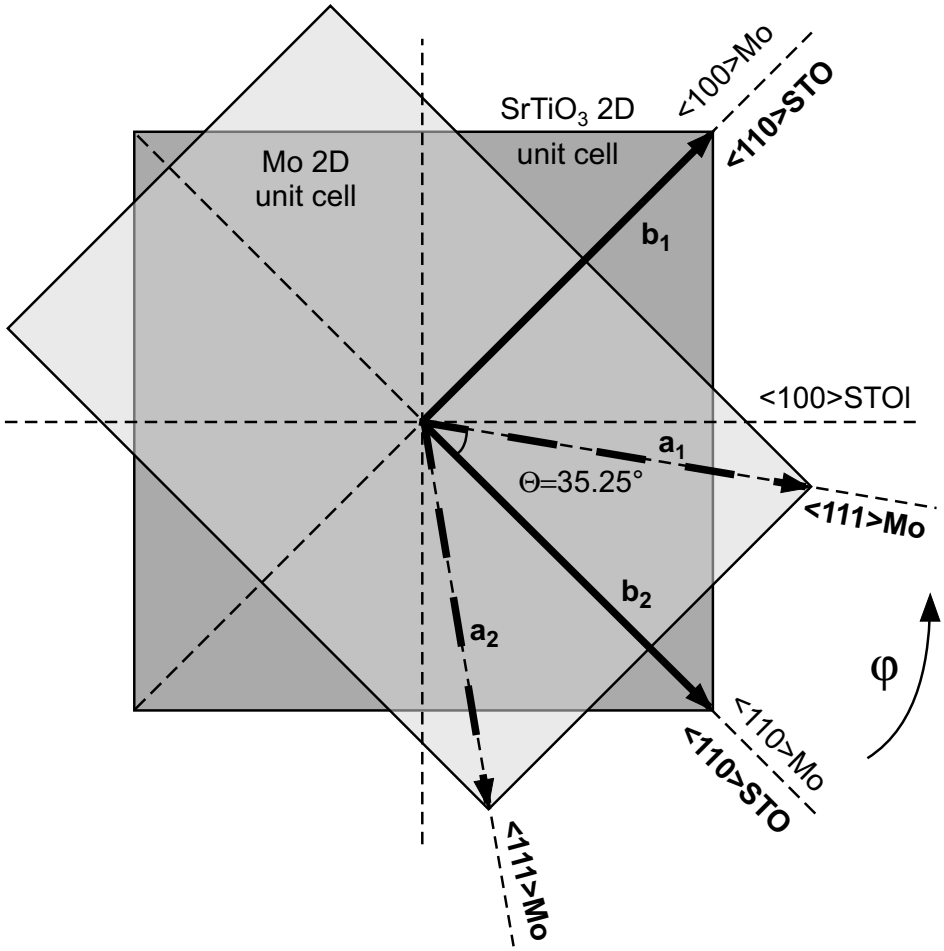

Figure A.1: Sketch of the calculations setup, used in this work to determine the possible NCSL configurations for Mo on O-sublattice. The angle φ describes the rotation of the Mo lattice. As a zero rotation $\varphi = 0°$, the position $\langle 110\rangle_{Mo} \| \langle 110\rangle_{STO}$ (OR III) is taken.

An initial angle $\Theta = 35.25°$ between $\langle 111\rangle_{Mo}$ and $\langle 110\rangle_{STO}$ directions was taken so that $\langle 110\rangle_{Mo} \parallel \langle 110\rangle_{STO}$. This position was taken as the $\varphi = 0°$ rotation (Fig. A.1). The rotation was then performed in the range of φ from 0° to 90° and the values of σ and δ were calculated using the equations above.

The following limitations were applied to the calculation: k, l, m, n ≤ 10, $\delta \leq 4.5\%$ and $\sigma \leq 50$. It is always possible to choose a smaller unit cell with a larger degree of coincidence misfit, so both parameters should be kept as small as possible in order to interpret the obtained structure as a low energy structure from the geometrical point of view.

All values were calculated for both possible configurations of Mo on top of TiO_2 ter-

Table A.1: Possible NSCLs for Mo on O sub-lattice. As a zero rotation the position $\langle 110\rangle_{Mo}\|\langle 110\rangle_{STO}$ (OR III) is taken.

Misorientation $\varphi(^\circ)$	σ_{Mo}	σ_{SrTiO_3}	Coincidence misfit $\delta(\%)$	Orientation Relationship
0	25	25	3.01	$\langle 110\rangle_{Mo}\|\langle 110\rangle_{STO}$
0-3.7	*25*	*25, 18*	*3.01-3.9*	OR III
9.7	16	13	3.36	$\langle 111\rangle_{Mo}\|\langle 100\rangle_{STO}$
7.8-10.1	*16*	*13*	*1.8-3.9*	OR IV
35.3	1	1	1.2	$\langle 111\rangle_{Mo}\|\langle 110\rangle_{STO}$
33.2-37.4	*1, 11*	*1, 11*	*1.2-3.8*	OR II
45	29	25	3.6	$\langle 110\rangle_{Mo}\|\langle 100\rangle_{STO}$
44.8-46.8	*26, 29*	*25, 26*	*0.6-3.2*	$\langle 100\rangle_{Mo}\|\langle 100\rangle_{STO}$
				OR I a,b

Table A.2: Possible NSCLs for Mo on Ti sub-lattice. As a zero rotation the position $\langle 110\rangle_{Mo}\|\langle 100\rangle_{STO}$ (OR I) is taken.

Misorientation $\varphi(^\circ)$	σ_{Mo}	σ_{SrTiO_3}	Coincidence misfit $\delta(\%)$	Orientation Relationship
0	13	25	4.2	$\langle 110\rangle_{Mo}\|\langle 100\rangle_{STO}$
0-4	*20, 25*	*37, 41*	*2.1-4.2*	$\langle 100\rangle_{Mo}\|\langle 100\rangle_{STO}$
				OR I a,b
9.7	2	4	1.2	$\langle 111\rangle_{Mo}\|\langle 110\rangle_{STO}$
7.6-11.8	*2*	*4*	*1.2-3.8*	OR II
35.3	8	13	3.3	$\langle 111\rangle_{Mo}\|\langle 100\rangle_{STO}$
33.2-37.4	*8*	*13*	*1.7-3.9*	OR IV
45	13	20	4.3	$\langle 110\rangle_{Mo}\|\langle 110\rangle_{STO}$
39.6-50.4	*10, 13*	*17, 20*	*0.6-3.2*	OR III

minated $SrTiO_3$, which are Mo on O-sublattice and Mo on Ti-sublattice. It is important to note, that different zero rotation positions ($\varphi = 0^\circ$) for both cases were chosen to simplify the calculation: the position $\langle 110\rangle_{Mo}\|\langle 110\rangle_{STO}$ (OR III) for Mo on O-sublattice and $\langle 110\rangle_{Mo}\|\langle 100\rangle_{STO}$ (OR I) for Mo on Ti-sublattice. This affected only the values of φ, which shifted for 45°.

The results are summarized in Tables A.1 (the same as Table 6.2) and A.2. Although the values of σ exhibit small differences for O and Ti sublattices, the general tendency, i.e. which OR has the smallest σ values, and which the largest, is kept unchanged.

List of Tables

List of Figures

Bibliography

[Adachi1999] Adachi Y., Kohiki S., Wagatsuma K., Oku M. Changes in the chemical state of monocrystalline $SrTiO_3$ surfaces by argon ion bombardment. *Applied Surface Science* **143** (1999) 272.

[Andersen1990] Andersen J.E.T., Mller P.J. Ultra-thin deposition of copper on room temperature. *Thin solid films* **186** (1990) 137.

[Balluffi1982] Balluffi R.W., Brokman A., King A.H. CSL/DSC lattice model for general crystal-crystal boundaries anf their line deffects. *Acta Metallurgica et Materialia* **30** (1982) 1453.

[Bauer1958] Bauer E. *Zeitschrift für Kristallographie* **110** (1958) 372.

[Benthem2002] van Benthem K. *Electron microscopy investigations of the bonding behavior of metals on $SrTiO_3$ substrates*. Ph.D. thesis, Universität Stuttgart (2002).

[Benthem2002a] van Benthem K., Scheu C., Sigle W., Rühle M. Electronic structure investigations of Ni and Cr films on (100)$SrTiO_3$ substrates using electron energy-loss spectroscopy. *Zeitschrift für Metallkunde* **93** (2002) 362.

[Blondeau2002] Blondeau-Patissier V., Lian G.D., Domenichini B., Steinbrunn A., Bourgeois S., Dickey E.C. Molybdenum thin film growth on rutile titanium dioxide (110). *Surface Science* **506** (2002) 119.

[Bollmann1970] Bollmann W. *Crystal Defects and Crystalline Interfaces*. Springer Verlag, 1970.

[Born1999] Born M., Wolf E. *Principles of optics*. Cambridge University Press, 1999, 7 edition.

[Bredow1999] Bredow T., Pacchioni G. A quantum-chemical study of Pd atoms and dimers supported on TiO_2(110) and their interaction with CO. *Surface Science* **426** (1999) 106.

[Browning1993] Browning N.D., Chrisholm M.F., Pennycook S.J. Atomic - resolution chemical analysis using a scaning transmission electron microscope. *Nature* **366** (1993) 143.

[Bruley1993] Bruley J. Spatially-resolved electron-energy-loss near-edge structue-analysis of a near Σ11 tilt boundary in sapphire. *Microscopy Microanalysis Microstructure* **1** (1995) 23.

[Brydson1995] Brydson R., Müllejans H., Bruley J., Trusty P.A., Sun X., Yeomans J.A., Rühle M. Spatially-resolved electron-energy-loss studies of metal/ceramic interfaces in transition-metal alumina cermets. *Journal of Microscopy* **177** (1995) 369.

[Cardona1965] Cardona M. Optical properties of $SrTiO_3$ and $BaTiO_3$. *Physical Review A* **2A** (1965) 651.

[Chan1994] Chan S.W. Degenerate epitaxy, coincidence epitaxy and origin of special boundaries in thin films. *Journal of Physical Chemistry of Solids* **55** (1994) 1137.

[Chapon1985] Chapon C., Henry A.R., Chemam A. Formation and characterization of small Pd particles deposited on MgO as a model catalyst. *Surface Science* **162** (1985) 747.

[Chen1995] Chen F.R., Chang L., Chiou S.K., Hong C.S. High-resolution electron microscopy of Cu/MgO and Pd/MgO interfaces. *Materials Science Forum* **189-190** (1995) 373.

[Chung1979] Chung Y.W., Weissbard W.B. Surface spectroscopy studies of the $SrTiO_3$ (100) surface and the platinum-$SrTiO_3$ (100) interface. *Physical Review B* **20** (1979) 3456.

[Classen2001] Classen T. *Mikroskopische Struktur und Energetik von kohärenten Übergangsmetall-$SrTiO_3$-Grenzflächen*. Diploma Thesis, University of Stuttgart, 2001.

[Conard1996] Conard T., Rousseau A.C., Yu L.M., Ghijsen J., Sporken R., Caudano R., Johnson R.L. Electron spectroscopy study of the Cu/$SrTiO_3$ interface. *Surface Science* **359** (1996) 82.

[Cowley1957] Cowley J.M., Moodie A.F. The scattering of electrons by atoms and ctystals. 1. A new theoretical approac. *Acta Cryst.* **10** (1957) 609.

[Cowley1959] Cowley J.M., Moodie A.F. Electron diffraction and imaging effects for superimposed thin crystals. *Acta Cryst.* **12** (1959) 423.

[Dehm2002] Dehm G., Inkson B.J., Wagner T. Growth and microstructural stability of epitaxial Al films on (0001) α-Al_2O_3 substrates. *Acta Materialia* **50** (2002) 5021.

[Dehm1997] Dehm G., Scheu C., Möbus G., Brydson R., Rühle M. Synthesis of analytical and high-resolution transmission electron microscopy to determine the interface structure of Cu/Al_2O_3. *Ultramicroscopy* **67** (1997) 207.

[Dehm1998] Dehm G., Scheu C., Rühle M., Raj R. Growth and structure of internal Cu/Al_2O_3 and Cu/Ti/Al_2O_3 interfaces. *Acta Materialia* **46** (1998) 759.

[Denbigh1966] Denbigh P.N., Marcus R.B. Structure of very thin tantalum and molybdenum films. *Journal of Applied Physics* **37** (1966) 4325.

[Dickey2002] Dickey E.C., Ma Y., Bagiyono, Lian G.D., Sinnott S.B., Wagner T. Preferred crystallographic orientation relationships of nickel films deposited on (100) cubic-zirconia substrates. *Thin Solid Films* **372** (2002) 37.

[Doben1988] Doben P., Onellion M., Kime Y. The influence of metal substrates on the electronic states of metal overlayers. *Scanning Tunneling Microscopy* **2** (1988) 177.

[Domenichini2000] Domenichini B., Pétigny S., Blondeau-Patissier V., Steinbrunn A., Bourgeois S. Effect of surface stoichiometries on the interaction of Mo with TiO_2(110). *Surface Science* **468** (2000) 192.

[Elssner1990] Elssner G., Petzow G. *Metal/Ceramic Joining*, volume 30. ISIJ International, 1990.

[Evans1996] Evans J., Hayden B.E., Lu G. The adsorption of carbon monoxide on TiO_2(110) supported palladium. *Surface Science* **360** (1996) 61.

[Fischmeister1993] Fischmeister H.F., Elssner G., Gibbesch, Kadow K.H., Kawa F., Korn D., Turwitt M. Solid-state bonding of accurately oriented metals ceramic bicrystals in ultra-high vacuum. *Review of Scientific Instruments* **64** (1993) 234.

[Fu2003] Fu Q., Tchernychova E., Wagner T. Texture of molybdenum thin films on $SrTiO_3$: a RHEED study. *Surface Science Letters* **538** (2003) L511.

[Fu2001] Fu Q., Wagner T. Nucleation and growth of Cr clusters and films on (100)$SrTiO_3$. *Thin Solid Films* **420-421** (2001) 455.

[Fu2002] Fu Q., Wagner T. Thermal stability of Cr clusters and films on (100)$SrTiO_3$ surfaces. *Surface Science* **505** (2002) 39.

[Fujimoto1978] FUJIMOTO F. Periodicity of crystal structure images in electron microscopy with crystal thickness. *Physica Status Solidi A* **45** (1978) 99.

[Fujishita1979] FUJISHITA H., SHIOZAKI Y., SAWAGUCHI E. Lattice distortions of pbzro$_3$. *Journal of the Physical Society of Japan* **4** (1979) 1391.

[Gao2003] GAO M., SCHEU C., TCHERNYCHOVA E., RÜHLE M. Electron-energy-loss spectroscopy studies of Mo/$SrTiO_3$ interfaces grown by molecular beam epitaxy. *Journal of Microscopy* **210** (2003) 94.

[Gomes2003] GOMES J.R.B., LODZIANA Z., ILLAS F. Adsorption of small palladium clusters on the relaxed α-Al_2O_3(0001) surface. *Journal of Physical Chemistry* **107** (2003) 6411.

[Goniakowski1998] GONIAKOWSKI J. Electronic structure of MgO-supported palladium films: influence of the adsorption site. *Physical Review B* **57** (1998) 1935.

[Goniakowski1999a] GONIAKOWSKI J. Transition metals on MgO(100) surface: evolution of adsorption characteristics along the 4*d* series. *Physical Review B* **59** (1999) 11047.

[Goniakowski1999b] GONIAKOWSKI J., NOGUERA C. Characteristics of Pd deposition on the MgO(111) surface. *Physical Review B* **60** (1999) 16120.

[Gossman1991] GOSSMANN H., FISANICK G. Temperature dependence of the Stranski-Krastanov layer thickness. *Surface Science Letters* **244** (1991) L117.

[Goyhenex1996] GOYHENEX C., MEUNIER M., HENRY C.R. Limitation of Auger electron spectroscopy in the determination of the metal-on-oxide growth mode: Pd on MgO(100). *Surface Science* **350** (1996) 103.

[Grovernor1984] GROVERNOR S.R., SUTTON A.P., SMITH D.A. Epitaxy of bcc metals on fcc (001) substrates. *Scripta Metallurgica* **18** (1984) 939.

[Guilloux1996] Guilloux-Viry M., Perrin A., Padiou J., Sergent M., Rossel C. Epitaxially grown molybdenum thin films deposited by laser ablation on (100)MgO substrates. *Thin Solid Films* **280** (1996) 76.

[Gutekunst1997] Gutekunst G., Mayer J., Rühle M. Atomic structure of epitxial Nb/Al_2O_3 interfaces: I. Coherent regions. *Philosophical Magazine A* **75** (1997) 1329.

[Hansen1999] Hansen K.H., Worren T., Stempel S., Lægsgaard E., Bäumer M., Freund H.J., Besenbacher, Stensgaard I. Palladium nanocrystals on Al_2O_3: structure and adhesion energy. *Physical Review Letters* **83** (1999) 4120.

[Heidemann1973] Heidemann Y., Wettenge H. Change of lattice parameters of $SrTiO_3$. *Zeitschrift für Physik* **5** (1973) 429.

[Henrich1978] Henrich V.E., Dresselhaus G., Zeiger H.J. Surface defects and electronic structure of $SrTiO_3$ surfaces. *Physical Review B* **17** (1978) 4908.

[Henry1992] Henry C.R., Chapon C., C.Goyhenex. Size of the CO chemisorption on palladium clusters supported on magnesium oxide. *Surface Science* **272** (1992) 283.

[Hill1989] Hill D.M., Meyer H.M., Weaver J.H. Y, Ba, Cu and Ti interfaces with $SrTiO_3$ surfaces. *Journal of Applied Physics* **65** (1989) 4943.

[Howe1997] Howe J.M. *Interfaces in materials*. John Wiley & Sohns, Inc., New-York, 1997.

[Hull1984] Hull D., Bacon D.J. *Introduction to Dislocations*. Pegamon Press, London/Oxford, 1984, 3rd edition.

[Hwang1990] Hwang D.M., Ravi T.S., Ramesh R., Chan S.W., Chen C.Y., Nazar L. Application of near coincidence site lattice theory to the

otientations of $YBa_2Cu_3O_{7-x}$ grains on (001) MgO subdtrates. *Applied Physics Letters* **57** (1990) 1690.

[Imhoff1999] Imhoff D., Lauren S., Colliex C., Backhaus-Ricoult M. Determination of the characteristic interfacial electronic states of {111} Cu-MgO interfaces by ELNES. *European Physical Journal - Applied Physics* **5** (1999) 9.

[Jackson1994] Jackson T.J., Glowacki B.A., Evetts J.E. Oxidation thermodynamics of metal substrates during the deposition of buffer layer oxides. *Physica C* **296** (1994) 215.

[Jiang1996] Jiang Q.D., Zegenhagen J. $SrTiO_3$ (001) surface and growth of ultra-thin $CdBa_2Cu_3O_{7-x}$ films studied by LEED/AES and UHV-STM. *Surface Science* **338** (1996) L882.

[Kacim1994] Kasim S., Delcambe P., Binst L., Jardinier-Offergeld M., Bouillon F. Structural behavior of direct-current sputtered and thermally evaporated molybdenum thin films. *Thin Solid Films* **249** (1994) 150.

[Kato1989] Kato M., Wada M., Sato A., Mory T. Epitaxy of cubic crystals on (001) cubic substrates. *Acta Metallurgica et Materialia* **37** (1989) 749.

[Kawada1999] Kawada T., Iizawa N., Tomida M., Kaimai A., Kawamura K., Nigara Y., Mizusaki J. High-temperature transport properties at metal/$SrTiO_3$ interfaces. *Journal o fthe European Ceramic Society* **19** (1999) 687.

[Kawasaki1994] Kawasaki M., Takahashi K., Maeda T., Tsuchiya R., Shinohara M., Ishiyama O., Yonezawa T., Yoshimoto M., Koinuma H. Atomic control of the $SrTiO_3$ crystal surface. *Science* **266** (1994) 1540.

[Kido2000] Kido Y., Nishimura T., Hoshino Y., Namba H. Surface structures of $SrTiO_3$(001) and Ni/$SrTiO_3$(001) studied by medium-energy ion scattering and SR-photoelectron spectroscopy. *Nuclear Instruments and Methods in Physics Research B* **161-163** (2000) 371.

[Kienzle1999] Kienzle O. *Atomistische Struktur und chemische Zusammensetzung innerer Grenzflächen von Strontiumtitanat*. Ph.D. thesis, Universität Stuttgart, Stuttgart, Germany (1999).

[Kitchin2003] Kitchin J.R., Barteau M.A., Chen J.G. A comparison of gold and molybdenum nanoparticles on TiO_2(110) 1×2 reconstructed single crystal surfaces. *Surface Science* **526** (2003) 323.

[Knorr1994] Knorr D.B. Texture in thin films. *Materials Science Forum* **157-162** (1994) 1327.

[Landoldt1981] Landoldt-Börnstein. *Zahlenwerte und Funktionen aus Naturwissenschaft und Technik*, volume 16. Springer, Berlin, 1981.

[Lodziana2002] Łodziana Z., Nørskov J.K. Interaction of Pd with steps on Al_2O_3(0001). *Surface Science* **518** (2002) L577.

[Lu1992] Lu P., Cosandey F. Dislocation structure at Cu/MgO and Pd/MgO interfaces. *Acta Metall. Mater.* **40** (1992) S259.

[Lytle1964] Lytle F.W. X-Ray diffractometry of low-temperature phase transformations in strontium titanate. *Journal of Applied Physics* **7** (1964) 2212.

[Markov1976] Markov I., Kaishew R. Influence of supersaturation on the mode of crystallixation on crystalline substrates. *Thin Solid Films* **32** (1976) 163.

[Matsumoto1992] Matsumoto T., Tanaka H., Kawai T., Kawai S. STM imaging of a $SrTiO_3$ (100) surface with atomic scale resolution. *Surface Science* **278** (1992) L153.

[Matveev1999] Matveev A.V., Neyman K.M., Yudanov I.V., Rösch N. Adsorption of transition metal atoms on oxygen vacancies and regular sites of the MgO(100) surface. *Surface Science* **426** (1999) 123.

[May2001] May U., Calarco R., Hauch J.O., Kittur H., Fonine M., Rüdiger U., Güntherodt G. Charaterization of epitaxial growth of Fe(110) on $(11\bar{2}0)$ sapphire substrates driven by Mo(110) seed layers. *Surface Science* **489** (2001) 144.

[Meijering1971] Meijering J.L. *Advances in Materials Research*. John Willey and Sons, New York, 1971.

[Meixner1995] Meixner H., Gerblinger J., Lampe U., Fleischer M. Thin-film gas sensors based on semiconducting metal-oxides. *Sensors and Actuators B* **23** (1995) 119.

[Merwe1993] van der Merwe J. Theoretical considerations in growing uniform epilayers. *Interface Science* **1** (1993) 77.

[Moebus1994] Möbus G., Rühle M. Structure determination of metal/ceramic interfaces by numerical contrast evaluation of HRTEM micrographs. *Ultramicroscopy* **56** (1994) 54.

[Moebus1998] Möbus G., Schweinfest R., Gemming T., Wagner T., Rühle M. Iterative structure retrieval techniques in HRTEM: a comparative study and a modular program package. *Journal of Microscopy* **190** (1998) 109.

[Moodie1977] Moodie A.F., Warble C.E. Direct observation of Pd/MgO and Pd/SiO_2 reactions in transmission electron microscope. *Philosophical Magazine* **35** (1977) 201.

[Mullejans1995] Müllejans H., Bruley J. Electron-energy-loss near-edge structue of internal interfaces by spatial difference spectroscopy. *Journal of Microscopy* **180** (1995) 12.

[Muller1998] Muller D.A., Shashkov D.A., Benedek R., Yang L.H., Silcox J., Seidman D.N. Atomic scale observations of metal-induced gap states at {222}MgO/Cu interfaces. *Physical Review Letters* **80** (1998) 4741.

[Mykura1980] Mykura H., Bansal P.S., Lewis M.H. Coincidence site lattice relations for Mgo-CdO interfaces. *Philosophical Magazine A* **42** (1980) 225.

[Nassau1988] Nassau K., Miller A.E. Strontium-titanat - an index to the literature of properties and the growth of single crystals. *Journal of Crystallography* **3** (1988) 373.

[Ochs2000] Ochs T. *Theoretische Untersuchungen der atomaren and electronischen Structur an Korngrenzen in kubischraumzentrierten Übergangsmetallen und an Metall/Keramik-Grenzflächen*. Ph.D. thesis, Universität Stuttgart, Stuttgart, Germany (2000).

[O'Keefe1994] O'Keefe M.A., Radmilovic V. Specimen thickness is wrong in simulted HRTEM images. In *ICEM*, 361. Paris, 1994.

[Pennycook1991] Pennycook S.J., Jesson D.E. High-resolution Z-contrast imaging of crystals. *Ultramicroscopy* **37** (1991) 14.

[Petigny1999] Pétigny S., Domenichini B., Mostéfa-Sba H., Lesniewska E., Steinbrunn A., Bourgeois S. Molybdenum deposition on TiO_2 surfaces with different stoichiometries. *Applied Surface Science* **142** (1999) 114.

[Phillipp1994] Phillipp F., Höschen R., Osaki M., Möbus G., Rühle M. New high-voltage atomic resolution microscope approaching 1-Angstrom point resolution installed in Stuttgart. *Ultramicroscopy* **56** (1994) 1.

[Polli1999] Polli A., Wagner T., M.Rühle. Effect of Ca impurities and wet chemical etching on the surface morphology of $SrTiO_3$ substrates. *Surface Science* **429** (1999) 237.

[Polli2000] Polli A.D., Wagner T., Gemming T., Rühle M. Growth of platinum on TiO_2- and SrO-terminated $SrTiO_3$(100). *Surface Science* **448** (2000) 279.

[Reimer1984] Reimer L. *Transmission Electron Microscopy*. Springer-Verlag, Berlin, 1984.

[Renaud1999] Renaud G., Barbier A., Robach O. Growth, structure and morphology of the Pd/MgO(100) interface: epitaxial site and interfacial distance. *Physical Review B* **60** (1999) 5872.

[Richter2000] Richter G. *Charakterisierung der Keimbildung und des Wachstums dünner Pd-Schichten auf der $SrTiO_3$(001)-Oberfläche*. Ph.D. thesis, Universität Stuttgart, Stuttgart, Germany (2000).

[Romanov1998] Romanov A.E., Wagner T., Rühle M. Coherent to incoherent transition in mismatched interfaces. *Scripta Materialia* **38** (1998) 869.

[Ruehle1989] Rühle M., Evans A.G. Structure and chemistry of metal ceramic interfaces. *Materials Science and Engineering A* **107** (1989) 187.

[Ruehle1990] Rühle M., Evans A.G., Ashby M.F., Hirth J.P. (eds.). *Metal-Ceramic Interfaces*, 4. Acta-Scripta Metallurgica Proceedings, Pergamon Press, Oxford, 1990.

[Ryan1999] Ryan P.A., Tsui F. Smoothening transition during initial epitaxial growth of Mo on sapphire. *Applied Physics Letters* **75** (1999) 3796.

[Scheu1996b] Scheu C. *Electron energy-loss spectroscopy at Cu/Al_2O_3 and Ti/Al_2O_3 interfaces*. Ph.D. thesis, Universität Stuttgart, Germany (1996b).

[Scheu1995] Scheu C., Dehm G., Müllejans H., Brydson R., Rühle M. Electron-energy-loss near-edge structue of metal-alumina interfaces. *Microscopy Microanalysis Microstructure* **6** (1995) 19.

[Scheu1996a] Scheu C., Dehm G., Müllejans H., Rühle M. Growth, structure and interfaces of Cu and Cu/Ti thin films on (0001)alpha-Al_2O_3. *Materials Science Forum* **207-209** (1996) 181.

[Scheu1998] Scheu C., Dehm G., Rühle M. Electron-energy-loss spectroscopy studies of Cu-alpha-Al_2O_3 interfaces grown by molecular beam epitaxy. *Philosophical Magazine A* **78** (1998) 439.

[Schweinfest1998] Schweifest R., Ernst F., Wagner T., Rühle M. High-precision assessment of interface lattice offset by quantitative HRTEM. *Journal of Microscopy* **194** (1998) 142.

[Sinnott2003] Sinnott S.B., Dickey E.C. Ceramic/metal interface structures and their relationship to atomic- and meso-scale properties. *Materials Science and Engineering R* **42** (2003) 1.

[Smith1976] Smith D.A., Pond R.C. Bollmann's O-Lattice theory: a geometrical approach to interface structure. *International Materials Review* **205** (1976) 61.

[Spence1981] Spence J.C.H. *Experimental High-Resolution Electron Microscopy*. Clarendon Press, Oxford, 1981.

[Stadelmann1987] Stadelmann P.A. EMS - a software package for electron-diffraction analysis and HRTEM image simulation in materials science. *Ultramicroscopy* **21** (1987) 131.

[Strecker1993] Strecker A., Salzberger U., Mayer J. Specimen preparation for transmission electron microscopy: reliable method for cross-sections and brittle materials. *Prakische Metallograhpie* **30** (1993) 482.

[Sutton1987] Sutton A.P., Balluffi R.W. On geometric criteria for low interfacial energy. *Acta Met. et Mat.* **35** (1987) 2177.

[Sutton1994] Sutton A.P., Balluffi R.W. *Interfaces in crystalline materials*. Clarendon Press, Oxford, 1995, 1 edition.

[Svedberg1999] Svedberg E.B., Jemander T.S., Lin N., Erlandsson R., Hansson G., Birch J. Epitaxial growth of UHV magnetron sputtered Mo thin films on MgO (001) substrates, oxygen segregation and surface reconstructions. *Surface Science* **433** (1999) 31.

[Swiech1999] Święch W., Mundschau M., Flynn C.P. Characterisation of single crystal films of milybdenum (011) grown by molecular beam epitaxy on sapphire ($11\bar{2}0$) and studied by low-energy electron microscopy. *Surface Science* **437** (1999) 61.

[Takayanagi1978] Takayanagi K., Yagi K., Honjo G. Roles of lattice fitting in epitaxy. *Thin Solid Films* **48** (1977) 137.

[Tanaka1994] Tanaka H., Matsumoto T., Kawai T., Kawai S. Interaction of oxygen vacancies with O_2 on a reduced $SrTiO_3$ (100) surface observed by STM. *Surface Science* **318** (1994) 29.

[Tsao1993] Tsao J.Y. *Materials Fundamentals of Molecular Beam Epitaxy*. Academic Press, San Diego, 1993.

[Tsurekawa1993] Tsurekawa S., Tanaka T., Yoshinaga H. Grain boundary structure, energy and strength in molybdenum. *Materials Science and Engineering* **A176** (1993) 341.

[Uchino1994] Uchino K. *Ferroelectric Ceramics*. VCH, Weinheim, 1994.

[Wagner2001] Wagner T., Polli A.D., Richter G., Stanzik H. Epitaxial growth of metals on (100) $SrTiO_3$: the influence of lattice mismatch and reactivity. *Zeitschrift für Metallkunde* **92** (2001) 701.

[Waser1990a] Waser R., Baiatu T., Hardtl K.H. DC electrical degradation of perovskite-type titanates .1. Ceramics. *Journal of the American Ceramic Society* **73** (1990) 1645.

[Waser1990b] Waser R., Baiatu T., Hardtl K.H. DC electrical degradation of perovskite-type titanates .2. Single crystals. *Journal of the American Ceramic Society* **73** (1990) 1654.

[Williams1996] Williams D.B., Carter C.B. *Transmission Electron Microscopy*. Plenum Press, New York, 1996.

[Winterbottom1967] Winterbottom W.L. Equilibrium shape of a small particle in contact with a foreign substrate. *Acta Metallurgia* **15** (1967) 303.

[Wulff1901] Wulff G. *Zeitschrift für Kristallographie* **34** (1901) 449.

[Xu1997] Xu C., Oh W.S., Liu G., Kim D.Y., Goodman D.W. Scanning tunneling microscopy studies of the TiO_2(110) surface: structure and the nucleation growth of Pd. *Physical Review B* **56** (1997) 13464.

[Yoshimoto1994] Yoshimoto M., Maeda T., Shimozono K., Koinuma H., Shinohara M., Ishiyama O., Ohtani F. Topmost analysis of $SrTiO_3$ (001) by coaxial impact collision ion-scattering spectroscopy. *Applied Physics Letters* **65** (1994) 3197.

Acknowledgements

I would like to thank:

- Prof. Manfred Rühle for giving me the opportunity to work in his department and his constant interest in forthcoming of this thesis.
- Prof. Fritz Aldinger for taking over the *Mitbericht*.
- exceptionally Dr. Christina Scheu for her continuous guidance and support throughout the project and for the proofreading of the thesis.
- Dr. Thomas Wagner for the fruitful discussions in the field of thin films and for the MBE growth of the $Pd/SrTiO_3$ and $Mo/SrTiO_3$ specimens.
- Dr. Gunter Richter for the extensive introduction into and constant help with the quantitative HRTEM analysis, and many scientific discussions.
- Dr. Sašo Šturm for many rewarding scientific discussions, support regarding the HRTEM image simulations and for help with the HAADF experiments.
- Dr. Miran Čeh at the Jošef Štefan Institute (Ljubljana, Slovenia) for help with the HAADF experiments.
- Dr. Qiang Fu for the MBE growth of $Mo/SrTiO_3$ and many fruitful discussions.
- Dr. Min Gao for the fruitful cooperation concerning analytical TEM.
- Ute Salzberger and Adolf Strecker for their patience while introducing me to the specimen preparation techniques, and preparation of excellent TEM specimens.

- Peter Kopold and Reiner Höschen for the introduction to the microscopes and technical support during the CTEM and HRTEM experiments.
- Gerd Maier for the help with XRD experiments.
- all members of the group of Prof. Rühle for warm working atmosphere, many beneficial work and private discussions, and support with solving all kind of problems.
- my friends for their strong support; especially André Christ for standing by me throughout these times and continuous encouragement.

This thesis was performed at the Max-Planck-Institut für Metallforschung, Stuttgart at the department of Prof. Manfred Rühle under financial support of German Science Foundation through the Graduirtenkolleg "Innere Grenzflächen in kristallinen Materialien".